



DIPLOMARBEIT

Particlelike States in D-Shaped Fibers

ausgeführt am

Institut für Theoretische Physik
der Technischen Universität Wien

Institute for Theoretical Physics
Vienna University of Technology

unter der Anleitung von
Dipl.-Ing. Philipp Ambichl
und

Univ.-Prof. Dipl.-Ing. Dr. techn. Stefan Rotter
durch

Matthias Kühmayer
Klein-Mariazell 78
A-2571 Altenmarkt
e0825988@student.tuwien.ac.at

Datum

Unterschrift

Contents

1	Introduction	1
2	Theoretical Framework	5
2.1	Classical Dynamics	5
2.1.1	Classical Phase Space of D-Shaped Billiards	7
2.1.2	Characteristic Quantities of Chaotic Systems	11
2.1.3	Monte-Carlo Generation of Trajectory Bundles	14
2.2	Wave Dynamics	16
2.2.1	Solving Helmholtz’s Equation	16
2.2.2	Heisenberg Time	18
2.2.3	“Quantum” Poincaré Sections	19
2.2.4	Scattering Formalism	22
2.2.5	Wigner-Smith Time-Delay Operator	24
3	Results	27
3.1	Wave Dynamics in a 2D Fiber Toy Model	28
3.1.1	Non-Operator-Based Approaches	29
3.1.2	Projection of the Time-Delay Operator	32
3.1.3	Introducing the Dependence Shift (DEFT) Operator	36
3.1.4	Impact of Imperfections	42
3.2	Wave Dynamics in a 3D D-Shaped Fiber	45
3.2.1	Generalizing the Projection Procedure	45
3.2.2	Finding Island States via the DEFT-Operator	49
3.3	Classical Dynamics in a 3D D-Shaped Fiber	57
3.4	Classical Dynamics in a 3D D-Shaped Rod	61
4	Summary and Outlook	67
5	Acknowledgments	71
A	Hamiltonian Optics	73
B	Exponential Growth of Distances in Chaotic Systems	75
C	Derivation of the Scalar Helmholtz Equation	77

D Spatial Participation Ratio	79
Bibliography	81

Chapter 1

Introduction

Complex wave dynamics is one of the cornerstones of modern physics. Ranging from the description of classical waves like sound waves, water waves and electromagnetic waves to subatomic particles whose dynamics are governed by the Schrödinger equation, the treatment of wave scattering is among the most important challenges in these fields of research. In scattering theory, a general tool for the calculation of the propagation of wavefronts is the scattering matrix which fully describes the asymptotics of a scattering process and consists of the transmission and reflection matrices of each system port. Experimentally, the transmission matrix can be measured by applying wavefront shaping techniques using spatial light modulators, antennas or loudspeaker arrays to control the incident field. In optics, these transmission matrix measurements can, for example, be used for focusing light through or inside a complex scattering medium, or for coupling to the so-called *open transmission* channels [1, 2]. Recently, these wavefront shaping concepts have also been successfully applied to multi-mode optical fibers, which could thereby be turned into microscopes [3], or into optical tweezers for optically trapping and manipulating of micro-particles [4]. Moreover, it has recently been shown that these fibers are highly predictable systems with respect to refractive index deviations or fiber curvatures [5], which may open up new possibilities in the field of optical imaging.

In conventional fibers, the cross section is of circular shape which features regular dynamics, whereas adding a straight cut, yielding a D-shaped fiber cross section, results in either completely chaotic, regular or mixed dynamics of classical light trajectories inside the fiber [6]. Chaotic systems are governed by an exponential growth in the phase space separation of two initially nearby trajectories, whereas systems with a mixed phase space feature islands with regular dynamics on which the phase space separation grows linearly. Moreover, the classical phase space structure also plays a key role in understanding the dynamics of wave states in a given system. In this context, it was also discovered that among highly excited fiber modes which feature a small transverse wavelength, so-called *scars* exist which show an intensity enhancement along classically unstable periodic orbits. These topics have been studied theoretically for D-shaped fibers and billiard systems [6]. Specifically, the phenomenon of light scarring in a fully chaotic D-shaped fiber has

been investigated [7], and the properties and statistics of regular modes in mixed D-shaped fibers have been studied [8]. Apart from addressing certain modes, a big goal in fiber optics is to find states with little dispersion and a high degree of collimation, where we will consider the concepts introduced by Wigner and Smith in order to reach this goal.

In the framework of quantum mechanical scattering theory, Wigner showed the possibility to extract information about the mean interaction time of a particle passing a potential from the corresponding scattering phase [9]. Following Wigner and using the concept of scattering matrices, Smith derived a “lifetime matrix” [10], which is nowadays well-known under the term of Wigner-Smith time-delay operator. Applying this concept to waveguide systems, the eigenvalues of this operator are the so-called *proper delay times*, while some of its eigenstates might be given by collimated wavefronts that follow classical trajectory-like paths, provided that the associated proper delay time is lower than the Ehrenfest time of the system [11]. Due to their classical behavior, these states are called *particlelike states* and correspondingly they feature a transmission close to zero or one, which allows for a very efficient transmission through a complex system. The concept of time-delay is a general concept of wave dynamics that can be applied to almost any type of waves and the existence of particlelike states has just recently been verified experimentally in an elastic cavity using laser-excited ultrasound waves [12].

In this thesis, we search for particlelike states in multi-mode fibers with a D-shaped cross section without cladding in the mixed and completely chaotic case. We will also draw a comparison between classical-trajectory-bundles and wave dynamics. Regarding the classical dynamics, we will use Monte-Carlo methods to generate trajectory bundles that mimic initial wavefronts in order to achieve the best coincidence with our wave simulations. In the framework of the Helmholtz equation, our search for particlelike wave states will be focused on finding a new operator constructed from the transmission matrix, which contains states with the desired particlelike behavior among its eigenstates, where we will exploit the concept of time-delay. The behavior of those wave states will be investigated in the spatial domain, as well as in classical phase space by means of Husimi distributions. We will see, that the phase space structure, which depends on the truncation of the fiber cross section, plays an important role for finding particlelike states since islands in a classically mixed phase space can help a wave state to stay collimated for longer propagation times compared to systems with regular or chaotic phase spaces. Ultimately, our aim is to study in which way these special states of light are suitable for efficient data transmission and for optical imaging techniques based on multi-mode optical fibers.

Considering an experimental realization of this work, we also have to deal with restrictions regarding the possible experimental methods and the geometric dimensions at hand. Currently, the collaborating group of Hui Cao at the Yale University is limited to millimeter-sized cross section diameters, i.e., we are dealing with glass

rods rather than fibers. Since the full wave simulation of such a large rod-system is numerically not feasible for optical wavelengths in the visible spectrum, we will thus restrict the investigation of the actual experimental setup to classical trajectory bundle simulations, in order to make predictions about the behavior of wave states in this system.

Chapter 2

Theoretical Framework

In this chapter, we first give an overview over the classical trajectory dynamics of light rays in different D-shaped geometries. Besides the dynamics in position space, the behavior of states in phase space is also of great importance as it features the simultaneous visualization in position *and* momentum space. Moreover, we will introduce characteristic quantities which give a measure for the chaoticity of a system and we will discuss the description of wave states through trajectory “bundles”. The latter will also feature spreading in order to draw a fair comparison to wave states. Regarding the wave dynamics, we will explain how to solve the wave equation and introduce a characteristic time called Heisenberg time up to which a wave consisting of quantized fiber modes can mimic the classical behavior which is based on a continuous spectrum. Furthermore, we will give an overview of phase space distribution functions that allow a representation of wave states in classical phase space and describe the scattering formalism which is used to derive an expression for the transmission matrix. This transmission matrix is then used to construct the time-delay operator, where besides the meaning of its eigenvalues and eigenstates an algorithm for treating non-square transmission matrices is presented.

2.1 Classical Dynamics

In this section we consider the dynamics of classical trajectories in a straight fiber, i.e. without bends or imperfections, with a D-shaped cross section without a cladding, see sketch in Fig. 2.1. In order to describe a light ray by way of a particle-trajectory, we have to find expressions which describe the trajectory’s dynamics in such a system. These will serve as building blocks for approximating wave states as bundles of trajectories.

Due to the translational invariance of our system, the dynamics reduce to those of a two-dimensional D-shaped billiard. Even though we are not dealing with a real billiard system with hard walls, we can make use of this assumption since the refractive index difference between the fiber’s silica-core ($n_{\text{co}} \approx 1.5$) and the surrounding “air-cladding” ($n_{\text{cl}} \approx 1$) is quite high resulting in a pretty steep critical angle of total internal reflection. According to Snell’s law, this angle calculates to

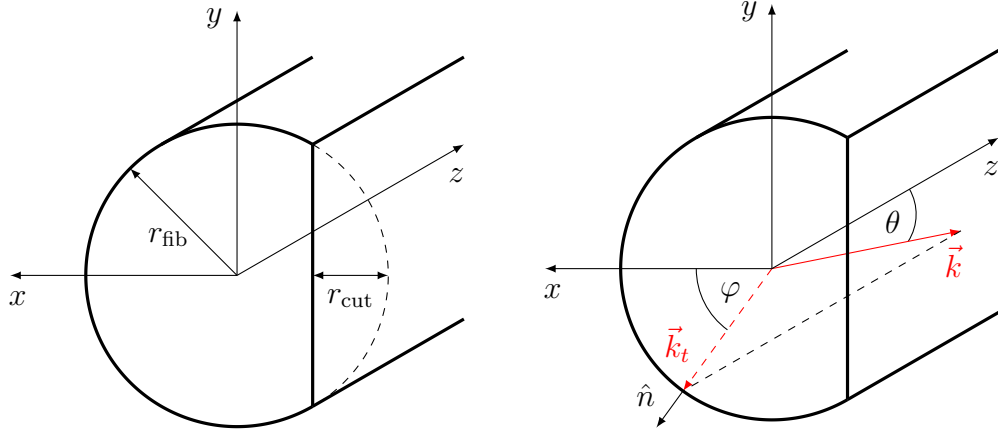


Figure 2.1: Left: Schematic of the fiber geometry. Right: Trajectory's “wavevector” \vec{k} (red line) and its projection onto the cross section (red dashed line) with the injection angle φ w.r.t. the x -axis and θ w.r.t. to the z -axis indicated.

$$\eta_c = \arcsin \left(\frac{n_{\text{cl}}}{n_{\text{co}}} \right) \approx 41.8^\circ , \quad (2.1.1)$$

measured normal to the cross section surface. Due to a limited number of open modes available in our wave simulations (see section 2.2), this angle will never be reached and hence there will always be total internal reflection.

Starting from Fermat's principle which states that light takes the path whose optical path length is an extremum, one can derive an equation of motion for the light trajectory (see Appendix A)

$$\frac{d}{ds} \left(n \frac{d\vec{x}}{d\zeta} \right) = \vec{\nabla} n , \quad (2.1.2)$$

which is similar to the respective equation of a point particle $d\vec{p}/dt = \vec{F}$ with $\vec{p} = m d\vec{x}/dt$, where the time t is replaced by the arc length ζ along the particle's trajectory, and the mass m is replaced by the refractive index n of the material. Moreover, we see that the refractive index plays the role of a potential whose gradient can be seen as a force acting on the trajectory. Since our system is homogeneous inside the cross section we have $\vec{\nabla} n = 0$ resulting in a free propagation of a light ray until it hits the boundary. There it gets reflected according to Snell's law, which states that for total internal reflection, the angle of reflection is equal to the angle of incidence. Thus, the “wavevector” in the transverse xy -plane after a reflection can be determined by

$$\vec{k}_t' = \vec{k}_t - 2(\vec{k}_t \cdot \hat{n})\hat{n} , \quad (2.1.3)$$

where \hat{n} is the outward normal unit vector to the boundary of the two-dimensional D-shaped cross section at the reflection point, $|\vec{k}_t| = n_{\text{co}}(2\pi/\lambda) \sin(\theta) = |\vec{k}_t'|$ (see Fig. 2.1), and λ is the light's vacuum wavelength.

2.1.1 Classical Phase Space of D-Shaped Billiards

The phase space of a given dynamical system represents all possible states of the system, where each point corresponds to one of those possible states. Since every degree of freedom is represented as an axis, the classical phase space for a system with N_f degrees of freedom, i.e. N_f spatial dimensions, is generally $2N_f$ -dimensional, consisting of N_f generalized positions and N_f generalized momenta. For high-dimensional systems, it is thus impossible to visualize the full phase space and, therefore, it is convenient to introduce so-called *Poincaré surface of sections* (PSSs) which are lower-dimensional cuts through the high-dimensional phase space. In our case of a three-dimensional fiber, $N_f = 3$, but since our particlelike states should stay collimated during the propagation through the system, we are particularly interested in the PSS at the output facet ($z = l_{\text{fb}}$) in which a localization should be visible. This reduces the number of dimensions to $2N_f - 1 = 5$. Given that in a straight fiber, the dynamics of a single trajectory projected to the two-dimensional cross section do not principally change when changing the angle to the optical axis, θ , gives us the opportunity to fix this angle, i.e. to fix k_z , and to reduce the number of dimensions to $2N_f - 2 = 4$. Lastly, we can consider just a single transverse wavevector component, i.e., k_x or k_y , since the other one is fixed by energy conservation, which reduces the number of dimensions to $2N_f - 3 = 3$.

Apart from the above considerations, it is more convenient to use so-called *Birkhoff coordinates* which are introduced in the following, where the full description of a billiard system can be mapped entirely to the dynamics on the boundary. This reduces the number of dimensions to 2, resulting in two-dimensional graphs which are much easier to read.

Birkhoff Coordinates

An important concept in the description of classical billiard systems are the Birkhoff coordinates which contain all dynamical information of a two-dimensional billiard. They are defined for every bounce of the trajectory at the walls and for a D-shaped billiard they are given by the following two parameters: the normalized arc length $s = \varphi/\varphi_{\text{max}}$ at the point of impact, and the sine of the angle of a trajectory after a reflection (see Fig. 2.2), $t = \sin \chi$, which can also be seen as the normalized tangential momentum. The sign of χ thus corresponds to the sign of the angular momentum. Together they form a mapping from the n -th bounce to the $(n+1)$ -th,

$$s_n, t_n \rightarrow s_{n+1}, t_{n+1} , \quad (2.1.4)$$

which is area preserving if the boundary is convex and continuously differentiable [13]. Given that our fiber cross section is D-shaped, our boundary is not continuously differentiable and thus we just take the curved part of the boundary into account. Due to time-reversal symmetry of our trajectories, our phase space

is symmetric under the mapping $\chi \rightarrow -\chi$, where our y -symmetric fiber geometry additionally causes our phase space to be symmetric under the transformation $\varphi \rightarrow -\varphi$.

Poincaré Surface of Section

In what follows, we explicitly investigate the classical PSS at the fiber boundary using Birkhoff coordinates, where the phase space structure and thus the classical dynamics depend on the ratio $\gamma = r_{\text{cut}}/r_{\text{fib}}$ (see Fig. 2.2). In a full or half circle ($\gamma = 0$ or 1), we get completely regular dynamics since we can separate the equations of motion [6], then. This separation yields two constants of motion which are given by the radial momentum k_r and the angular momentum L in a full circle billiard. In the half circle billiard the angular momentum can change its sign and hence the second constant of motion is given by L^2 instead of L . For these two systems, we thus have the same number of degrees of freedom as constants of motion, which is the reason for their regular dynamics. For all other values of γ neither L nor L^2 is conserved, which results in completely chaotic ($0 < \gamma < 1$), or mixed ($1 < \gamma < 2$) dynamics.

In Fig. 2.3 PSSs for different values of γ are shown. The first diagram shows the full circle billiard with its regular dynamics, and introducing a cut $0 < \gamma < 1$, we see that the phase space consists entirely of the chaotic sea. Notice that some empty horizontal lines can be seen in these plots which numerically originate from classical periodic orbits as explained below. Looking at the circle billiard we can define two types of periodic orbits: the polygon and the star orbits (see Fig. 2.2).

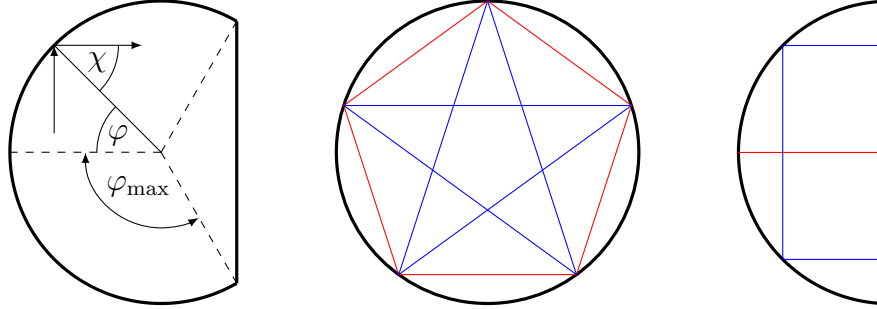


Figure 2.2: Left: Fiber cross section with the Birkhoff coordinates φ and χ indicated. Middle: Example of a polygon orbit with $n = 5$ bounces (red) and a star-shaped orbit with $n = 5$ and $q = 2$ trips around the circle (blue). Right: Two periodic orbits in a fiber with $\gamma = 1.05$ which correspond to the centers of the two largest types of islands in the PSS.

For a polygon orbit with n edges, we know that the sum of the interior angles is given by $2\chi n = (n - 2)\pi$, and hence the angle of reflection is

$$\chi = \frac{(n - 2)\pi}{2n} . \quad (2.1.5)$$

For the star-shaped orbits with n edges, we also have to take the number q of trips around the circle into account. In such an orbit the reflection angle is given by

$$\chi = \frac{(n - 2q)\pi}{2n} . \quad (2.1.6)$$

Depending on the fiber cut, some of these orbits do not bounce off the cut region and survive like in a full circle billiard. Since both of these two types of orbits have measure zero in phase space, it is practically impossible to launch a trajectory there. Furthermore, we can only treat finite propagation times in our numerical simulation, which means that we cannot propagate a trajectory long enough, such that it would fill out these empty lines visible in the PSSs for $0.1 \leq \gamma \leq 0.9$ in Fig. 2.3 due to the underlying chaoticity. In a mixed PSS, this effect is even more pronounced since there, some trajectories are trapped on stable islands, where different sets of parameters correspond to different island-contours. This results in partly empty islands due to the finite grid spacing of our initial parameters which can be seen in the PSSs for $1 < \gamma < 2$ in Fig. 2.3.

At $\gamma = 1$, we again get regular dynamics as mentioned above, and cutting more than one radius ($\gamma > 1$) causes the regular bands to split up into some stable islands, where the space between them is filled out by the chaotic sea. Cutting further results in the disappearance of some smaller islands into the chaotic sea, where the bigger islands grow in size, and after the special case of $\gamma = 1.5$ almost the entire PSS is filled out with the central island.

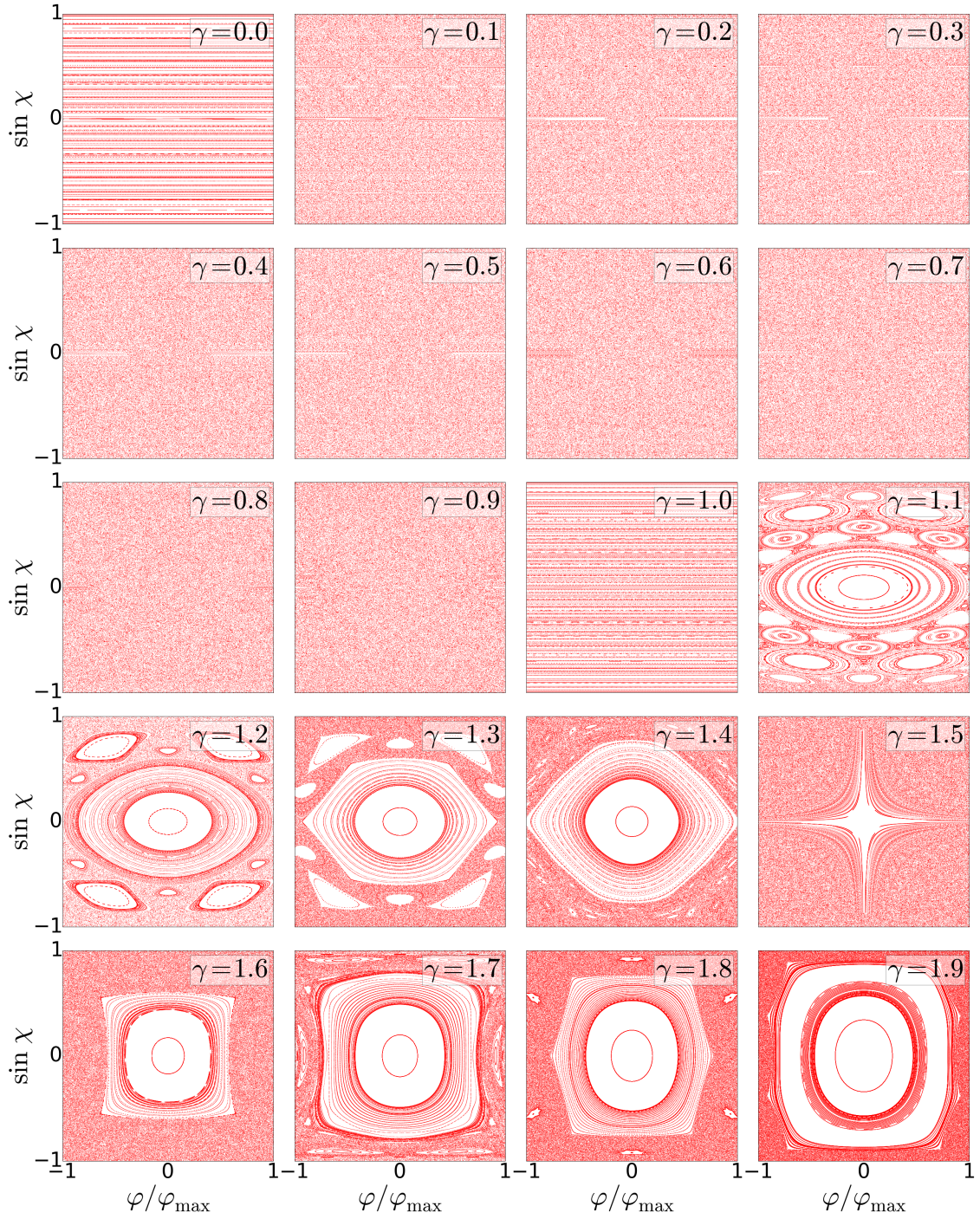


Figure 2.3: Poincaré surfaces of section for different values of $\gamma = r_{\text{cut}}/r_{\text{fib}}$. For $\gamma = 0, 1$ we get regular dynamics, for $0 < \gamma < 1$ the phase space is completely filled with the chaotic sea, and for $1 < \gamma < 2$ we have mixed dynamics, i.e., there exist some stable islands in between the chaotic sea. Please note that the value of φ_{max} changes for every value of γ .

2.1.2 Characteristic Quantities of Chaotic Systems

Lyapunov Exponent

In chaotic systems, the distance $d(t)$ between two initially nearby trajectories in phase space grows exponentially with the propagation time t , where the measure for this growth is given by the Lyapunov exponent Λ_{phys} (see. Appendix B) [14]:

$$d(\vec{x}_0, t) = d(\vec{x}_0, 0)e^{\Lambda_{\text{phys}}t} . \quad (2.1.7)$$

Here, the subscript denotes the physical exponent which is given in units of $1/s$. Since the Lyapunov exponent depends on the initial position and injection angles at the input facet, we use a certain parameter set and track the phase space separation of each trajectory pair. Then, we build the mean over all individual exponents in order to arrive at an estimate for a single Lyapunov exponent which describes the system. Again we use Birkhoff coordinates, where we measure the phase space separation every time when the trajectories collide with the boundary

$$d(\vec{x}_0, n) = d(\vec{x}_0, 0)e^{\Lambda_{\text{Birk}}n} , \quad n = 1, 2, 3... \quad (2.1.8)$$

In contrast to (2.1.7) we have used another subscript to indicate that this exponent is dimensionless due to its calculation in Birkhoff coordinates. This Birkhoff Lyapunov exponent is then defined as

$$\Lambda_{\text{Birk}}(\vec{x}_0) = \lim_{n \rightarrow \infty} \lim_{d(0) \rightarrow 0} \frac{1}{n} \ln \left(\frac{d(\vec{x}_0, n)}{d(\vec{x}_0, 0)} \right) . \quad (2.1.9)$$

Numerically, the second limit cannot be realized due to finite machine precision. Thus, we use a very small initial separation in phase space greater than the machine's precision, where we chose to let the trajectories start from the same position with an angular difference of $\Delta\varphi = 10^{-14}$. Using a small $d(0)$ is important in order to observe an exponential growth of $d(t)$ over a fairly large number of bounces n , where a greater initial phase space separation would result in a faster reach of the saturated regime caused by the boundedness of the system. Due to this saturation, the first limit in (2.1.9) cannot be realized either, but in order to estimate the Lyapunov exponent it is sufficient to let the trajectories undergo a certain number of bounces until the saturation is reached. This saturation of $d(\vec{x}_0, n)$ can clearly be seen in Fig. 2.4, where the Lyapunov exponent shows a decrease proportional to $1/n$ due to the constant phase space separation. The Lyapunov exponent is then calculated by taking the mean value over a certain range of bounces for which it stays mostly constant, where this range is typically reached before the saturation sets in (see Fig. 2.4). To get a single Lyapunov exponent, we furthermore build the average over all initial conditions as mentioned above, where the conversion factor

from the Birkhoff to the physical exponent is given by the mean propagation time $\langle\tau\rangle$ between two collisions with the fiber boundary [15, 16],

$$\Lambda_{\text{phys}} = \frac{\Lambda_{\text{Birk}}}{\langle\tau\rangle} . \quad (2.1.10)$$

A more rigorous approach is the the so-called *Benettin method* [17], which is based on repeated rescaling of the offset from the reference trajectory every time the mentioned saturation is reached, which yields longer propagation times and thus a more precise value for the Lyapunov exponent. Another way of calculating the Lyapunov exponent is by considering the trajectories' stability matrices for each free propagation and reflection, where the Lyapunov exponents are then given by the eigenvalues of the product of these matrices [6]. These stability matrices describe the particle's short term phase space dynamics for which the exponential can be linearized resulting in a Jacobian matrix. Since the latter is a $N_f \times N_f$ matrix with $N_f = 2$ being the number of degrees of freedom in our billiard system, we get two exponents, where the one greater zero is a measure for the chaoticity of the system.

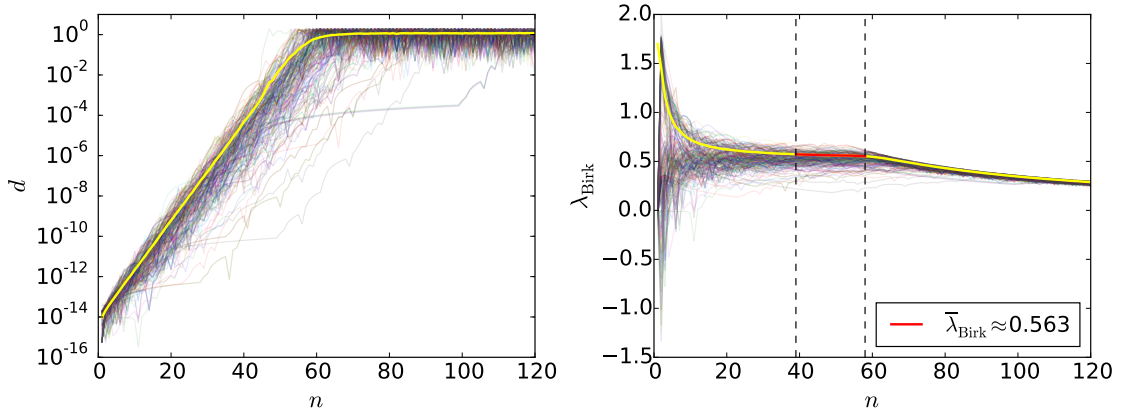


Figure 2.4: Exponential growth of phase space separations in a geometry with $\gamma = 0.44$. Left: Phase space distance between two trajectories dependent on the number of bounces for many initial conditions, where the yellow line shows the mean value and the saturated regime can be clearly seen ($n \approx 60$). Please note the logarithmic scale on the ordinate, where the slope is proportional to the Lyapunov exponent. Right: Lyapunov exponent dependent on the number of bounces for many initial conditions, where the yellow line denotes the mean value and the red line marks the region, where it stays mostly constant.

Ehrenfest Time

The Ehrenfest time is defined as the time, where the separation of two trajectories reaches a characteristic system length which is given by the square root of the fiber cross section:

$$d(\tau_E) = d(0)e^{\Lambda_{\text{phys}}\tau_E} \equiv L_0 = \sqrt{A_{\text{fib}}} . \quad (2.1.11)$$

Hence, the Ehrenfest time is given by

$$\tau_E = \frac{1}{\Lambda_{\text{phys}}} \ln \left(\frac{L_0}{d(0)} \right) . \quad (2.1.12)$$

Physically, at $t = \tau_E$ every pair of initially nearby trajectories will be spread out over the cross section. Since we want our trajectories or trajectory bundles to stay collimated, this time will serve as a useful estimate for an upper limit of propagation lengths in cases of fully chaotic systems. Looking at Eq. (2.1.12), we want to point out that this definition is valid for two trajectories, but since we want to treat trajectory bundles which mimic waves, we have to modify this definition. For this purpose, we set the initial spatial distance $d(0)$ to the mean distance between two trajectories in a Gaussian bundle, i.e., $d(0) = w_0 = 2\sigma_0$. Hence, at $t = \tau_E$ the number of particlelike bundles should be already pretty small which of course depends on the definition of the criterion for a bundle at the output facet to be counted as particlelike.

2.1.3 Monte-Carlo Generation of Trajectory Bundles

In order to mimic the behavior of waves, we now want to create bundles of trajectories that also feature the spreading of the corresponding wavepackets, where we assume Gaussian shaped intensity distributions which consist of $N_t = 10^3$ trajectories whose initial spatial spread is two times the Gaussian's standard deviation, i.e., $w_0 = 2\sigma_0$. Furthermore, they are defined by a preferred angle in the transverse plane $\varphi \in [0, 2\pi)$ and a preferred angle to the fiber axis θ .

The initial positions $\vec{r} = (x, y)$ in the fiber cross section A_{fib} are then generated by drawing random points from a Gaussian probability distribution

$$g(x, y) = \begin{cases} \frac{1}{2\pi\sigma_0^2} \exp\left(-\frac{(x-x_0)^2 + (y-y_0)^2}{2\sigma_0^2}\right) & \vec{r} \in A_{\text{fib}} , \\ 0 & \vec{r} \notin A_{\text{in}} , \end{cases} \quad (2.1.13)$$

which is truncated at the fiber boundary and normalized, i.e. $\int dx dy g(x, y) = 1$. In order to create minimal uncertainty bundles, we then also draw random points from the Fourier transform of the directed Gaussian

$$\tilde{g}(k_x, k_y) = \begin{cases} \mathcal{F}\{g(x, y) \exp[i(xk_{x,0} + yk_{y,0})]\} & k_x^2 + k_y^2 < k_0^2 , \\ 0 & k_x^2 + k_y^2 \geq k_0^2 , \end{cases} \quad (2.1.14)$$

which is also normalized, i.e., $\int dk_x dk_y \tilde{g}(k_x, k_y) = 1$. Using the Fourier transformation

$$\mathcal{F}\{g(x, y)\} = \frac{1}{2\pi} \int dx dy g(x, y) e^{-i(xk_x + yk_y)} \quad (2.1.15)$$

for the distribution of transverse wavevectors accounts for spreading, i.e. spatially more localized bundles will have a broader transverse momentum distribution, and will thus spread more quickly in accordance with the behavior of waves. Furthermore, the exponential factor in (2.1.14) containing $k_{x,0} = k_t \cos \varphi$ and $k_{y,0} = k_t \sin \varphi$ with $k_t = k_0 \sin \theta$ shifts the function to the preferred position $(k_{x,0}, k_{y,0})$ in Fourier space. Note that the light's wavelength enters in the above equations through k_t , where we use $\lambda = 553$ nm of the experimentally used Nd:YAG laser.

Numerically, one would start to draw three random numbers from uniform distributions, i.e. two for x_n and y_n , and one for our probability p_n , where the positions are accepted if the value lies beneath the function we want to draw our random samples from, i.e. $p_n < g(x_n, y_n)$. However, if we have highly localized distributions, the amount of discarded random numbers is huge. One can save computation time though by introducing a supporting Gaussian envelope function $h(x, y)$, from which it is easy to draw random samples from in order to achieve a higher acceptance rate (see Fig. 2.5). This is called acceptance-rejection method, where we have to ensure that $g(x, y) < Ch(x, y)$ with some real-valued constant $C > 1$. It can be shown that the unconditional acceptance probability is $1/C$, which means that a high

value of C results in many discarded random samples, and thus keeping the value of C as low as possible is crucial for a good performance of this algorithm. Since we place our trajectory bundles approximately one to three standard deviations away from the boundary, the effect introduced by the truncation is mostly rather small, and thus our wavevector distribution will look very similar to a Gaussian with a standard deviation of approximately $1/\sigma_0$. Thus, the supporting envelope function for $\tilde{g}(k_x, k_y)$ will be the Fourier transform of our spatial envelope function, i.e. $\tilde{h}(k_x, k_y)$.

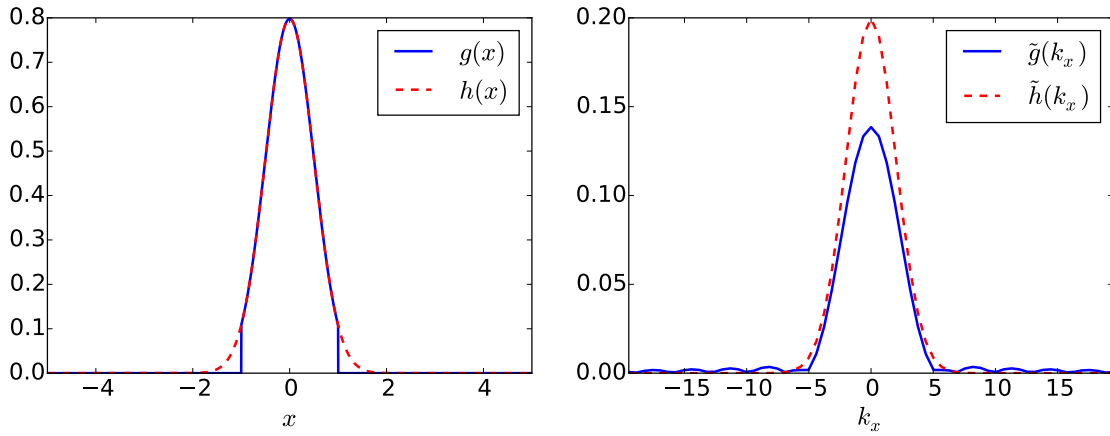


Figure 2.5: Left: Example of a one-dimensional, truncated Gaussian probability distribution $g(x)$ (blue solid line) from which we want to draw random samples. Since the random sampling of uniformly distributed values of x_n and p_n would result in many discarded random samples x_n , one can introduce a Gaussian envelope function $h(x)$ (red dashed line), from which it is easy to draw random samples from, where we have to assure that $Ch(x) > g(x)$ with some $C > 1$. Right: Fourier transformed distributions, where some oscillations in $\tilde{g}(k_x)$ appear due to the spatial truncation. Again, we have to find a $\tilde{C} > 1$ such that $\tilde{C}\tilde{h}(k_x) > \tilde{g}(k_x)$.

Having found the constant C , one then draws random samples x_n and y_n from the supporting Gaussian distribution $h(x, y)$ and p_n from the uniform distribution in the unit interval. The positions x_n and y_n are then accepted if $p_n Ch(x_n, y_n) < g(x_n, y_n)$, whereas they are discarded if this condition is not fulfilled. Together with its equivalent procedure for the Fourier transformed quantities, this is repeated until N_t positions (x, y) and wavevectors (k_x, k_y) are found, where the propagation of the whole bundles is computed by means of the propagation of each single trajectory as described at the beginning of section 2.1.

2.2 Wave Dynamics

2.2.1 Solving Helmholtz's Equation

In this subsection we discuss the algorithm to solve the three-dimensional wave equation for the electric field. This wave equation originates from Maxwell's equations and generally a full vectorial approach would be needed. However, in case of a medium homogeneous along z , i.e. $\epsilon(x, y, z) \equiv \epsilon(x, y)$, and a monochromatic and linearly polarized electric field with a harmonic time-dependence, the wave equation can be simplified to a scalar Helmholtz equation (see Appendix C),

$$[\Delta + n^2(\vec{r})k_0^2] \psi(\vec{r}, z) = 0 , \quad (2.2.1)$$

where $\Delta = \Delta_t + \partial_{zz}$ is the Laplacian, $\Delta_t = \partial_{xx} + \partial_{yy}$ is the transverse Laplacian and

$$n = n(\vec{r}) = \begin{cases} n_{\text{co}} = 1.5 & \vec{r} \in A_{\text{fib}} , \\ n_{\text{cl}} = 1.0 & \vec{r} \notin A_{\text{fib}} , \end{cases} \quad (2.2.2)$$

is the refractive index which depends only on the position $\vec{r} = (x, y)$ in the transverse plane due to the homogeneity of our system along the z -axis. Moreover, $k_0 = 2\pi/\lambda$ with λ being the vacuum wavelength of our monochromatic electric field. Due to the absence of scatterers or fiber bends, the solutions of Eq. (2.2.1) will keep their linear polarization in the transverse plane, which makes the full vectorial treatment unnecessary. Since $n(x, y, z) \equiv n(x, y)$, we can separate an exponential factor from the wavefunction and write down a general ansatz for the solution [7]

$$\psi(\vec{r}, z) = \int d\beta_z \chi(\vec{r}, \beta_z) e^{i\beta_z z} , \quad (2.2.3)$$

where $\beta_z = n_{\text{co}} \sqrt{k_0^2 - k_t^2}$ is the propagation constant. Inserting Eq. (2.2.3) into (2.2.1) yields

$$[\Delta_t + n^2(\vec{r})k_0^2] \psi(\vec{r}, z) = \beta_z^2 \psi(\vec{r}, z) , \quad (2.2.4)$$

which can also be written as a stationary Schrödinger equation with an effective potential

$$\left[-\frac{1}{2} \Delta_t + V(\vec{r}) \right] \chi(\vec{r}) = E \chi(\vec{r}) . \quad (2.2.5)$$

Using $\beta_0 = n_{\text{co}} k_0$, the effective potential is given by

$$V(\vec{r}) = \frac{1}{2} (\beta_0^2 - n^2(\vec{r})k_0^2) = \begin{cases} 0 & \vec{r} \in A_{\text{fib}} , \\ \frac{1}{2} (n_{\text{co}}^2 - n_{\text{cl}}^2) k_0^2 & \vec{r} \notin A_{\text{fib}} , \end{cases} \quad (2.2.6)$$

and the “eigenenergy” is defined as

$$E = \frac{1}{2} (\beta_0^2 - \beta_z^2) = \frac{1}{2} \beta_t^2 = \frac{1}{2} n_{\text{co}}^2 k_t^2 . \quad (2.2.7)$$

Eq. (2.2.5) basically describes a finite potential well whose solutions feature quantized eigenenergies E_n and corresponding eigenstates $\chi_n(\vec{r})$. Numerically, solving this equation is accomplished by using a finite differences approach with hard wall boundary conditions at the borders of our transverse grid. An eigenstate of Eq. (2.2.1) now reads

$$\psi_n(\vec{r}, z) = \mathcal{N}_n \chi_n(\vec{r}) e^{i\beta_{z,n} z} \quad (2.2.8)$$

with \mathcal{N}_n being a normalization constant. Here one can see the similarity between $\psi_n(\vec{r}, z)$ and the time-evolution of an eigenstate of the Schrödinger equation, where the z -coordinate plays the role of the time. The guided, flux-carrying modes fulfill $E_n < V(\vec{r})$, i.e.,

$$n_{\text{co}} k_{t,n} < \sqrt{n_{\text{co}}^2 - n_{\text{cl}}^2} k_0 . \quad (2.2.9)$$

Please note that we use the *open mode approximation*, where we just treat open ($\beta_{z,n} \in \mathbb{R}$) guided modes, and neglect the evanescent ones which feature a purely imaginary propagation constant $\beta_{z,n} \in \mathbb{C}$. We should further mention that the transverse eigenstates are orthogonal and intensity normalized according to

$$\int d^2r \chi_n^*(\vec{r}) \chi_m(\vec{r}) = \delta_{nm} . \quad (2.2.10)$$

In (the unbounded) longitudinal direction, one could use a scattering normalization to a Dirac δ -distribution for which $\mathcal{N}_n = 1/\sqrt{2\pi}$, however, a more convenient choice for describing wave guide states is the normalization to unit flux

$$j_z = \text{Re} \left[\psi_n^*(\vec{r}, z) \left(-i \frac{\partial}{\partial z} \right) \psi_n(\vec{r}, z) \right] = 1 . \quad (2.2.11)$$

Imposing the condition (2.2.11) onto our modes yields $\mathcal{N}_n = 1/\sqrt{\beta_{z,n}}$. Bear in mind that this also changes the transverse intensity normalization at a given z

$$\int d^2r \psi_n^*(\vec{r}, z) \psi_m(\vec{r}, z) = \frac{1}{\beta_{z,n}} \delta_{nm} , \quad (2.2.12)$$

and thus it is convenient to use either the δ - or the flux-normalization depending on the pursued purpose. Since our transverse differential operator in (2.2.5) is Hermitian, its eigenstates form a complete and orthogonal set of basis states, in which we can expand any arbitrary state

$$\Psi(\vec{r}, z) = \sum_n c_n \psi_n(\vec{r}, z) = \sum_n \frac{c_n}{\sqrt{\beta_{z,n}}} \chi_n(\vec{r}) e^{i\beta_{z,n} z} , \quad (2.2.13)$$

where we have already taken into account the flux normalization mentioned above.

2.2.2 Heisenberg Time

For a quantum mechanical system the Heisenberg time is given by the inverse of the mean level spacing, which is nothing else than the mean density of states

$$\tau_H = \frac{h}{\langle \Delta E \rangle} = \frac{2\pi}{\langle \Delta \omega \rangle} , \quad (2.2.14)$$

where h is Planck's constant. Beyond this time, the classical or semi-classical descriptions of waves break down and the discreteness of the energy spectrum of a bounded system becomes important. Thus, at this time-scale, a system cannot mimic the classical behavior which is based on a continuous spectrum. To obtain an expression for τ_H for classical waves, one can compare the time evolution of an arbitrary quantum mechanical state expanded into eigenstates of the respective Hamiltonian in position space,

$$\Psi(\vec{r}, t) = \sum_n c_n \chi_n(\vec{r}) e^{-i\omega_n t} , \quad (2.2.15)$$

to the propagation of an arbitrary state expanded into eigenstates of our Helmholtz equation (see Eq. (2.2.13)),

$$\Psi(\vec{r}, z) = \sum_n c'_n \chi_n(\vec{r}) e^{i\beta_{z,n} z} , \quad (2.2.16)$$

where c'_n contains the longitudinal normalization factor. In the above two equations, the eigenstates of the stationary Schrödinger equation in position space were denoted by the same symbol $\chi_n(\vec{r})$ as the one of the transverse Helmholtz equation (2.2.5) in order to emphasize the similarity of these equations. We can now see that the z -coordinate plays the role of the time and thus the Heisenberg time of our classical system is given by

$$\tau_H = \frac{2\pi}{\langle \Delta \beta_z \rangle} . \quad (2.2.17)$$

Since higher dimensional systems in most cases feature a higher density of states as energy levels are more closely spaced to each other, it usually holds that $\tau_H \gg \tau_E$ [18], however, in case of $\tau_H < \tau_E$ the Heisenberg time would replace the Ehrenfest time in its role as a limiting factor for propagation times of particlelike states.

Besides the analytical expression (2.2.17), one can also estimate the Heisenberg time (length) for our fiber system by using the relation [7]

$$\tau_H = \beta_0 A_{\text{fib}} , \quad (2.2.18)$$

where $\beta_0 = n_{\text{co}} k_0$ and A_{fib} is the area of the fiber cross section.

2.2.3 “Quantum” Poincaré Sections

In this subsection we introduce two prominent representatives of phase space distributions often used in wave mechanics. In classical mechanics, the choice of generalized coordinates defines conjugate generalized momenta which together define (commuting) coordinates in phase space. In quantum (and generally wave) mechanics, these observables are replaced by non-commuting Hermitian operators, where this non-commutativity impedes the association of a wave state with a single point in phase space. However, the *phase space formulation of quantum mechanics* restores the equivalence of quantum mechanics and Hamiltonian mechanics by representing a wave state by a quasi-probability distribution in phase space, instead of a wave function (or a density matrix), where in contrast to the former the latter has to be represented in position *or* momentum space.

Due to the high dimensionality of our system, we again just look at certain Poincaré surfaces of section as discussed in subsection 2.1.1 which are often called *quantum Poincaré sections* due to their heavy usage in quantum mechanics. Even though we are dealing with classical optics, we use this term, since the structure of the Helmholtz equation is similar to that of the time-independent Schrödinger equation as shown in subsection 2.2.1.

Wigner Distribution at a Fiber Facet

Since we search for states that stay collimated during the propagation through the system, a localization of their phase space distribution at the output facet should be visible. For this, we use the quantum-mechanical Wigner phase space distribution of a state $\Psi(\vec{r}, z)$ at the output facet ($z = l_{\text{fib}}$)

$$W(\vec{r}, \vec{k}_t) = \frac{1}{(2\pi)^2} \int_{-\infty}^{\infty} \Psi^*(\vec{r} + \vec{\xi}/2, l_{\text{fib}}) \Psi(\vec{r} - \vec{\xi}/2, l_{\text{fib}}) e^{-i\vec{\xi} \cdot \vec{k}_t} d^2\xi, \quad (2.2.19)$$

where \vec{r} and \vec{k}_t stand for the transverse position and transverse momentum of the wavefunction. Note that these two phase space variables are just vectors consisting of scalar quantities now and not operators, even though we are dealing with wave mechanics. This distribution is a quasi-probability distribution, i.e.

$$\int_{-\infty}^{\infty} d^2k_t W(\vec{r}, \vec{k}_t) = \langle \vec{r} | \rho | \vec{r} \rangle = |\Psi(\vec{r})|^2, \quad (2.2.20)$$

$$\int_{-\infty}^{\infty} d^2r W(\vec{r}, \vec{k}_t) = \langle \vec{k}_t | \rho | \vec{k}_t \rangle = |\Psi(\vec{k}_t)|^2, \quad (2.2.21)$$

$$\int_{-\infty}^{\infty} d^2k_t \int_{-\infty}^{\infty} d^2r W(\vec{r}, \vec{k}_t) = \text{Tr}(\rho) = 1, \quad (2.2.22)$$

which has furthermore the advantage of being uniquely defined (contrary to the Husimi distribution we introduce in the following section). In the above relations,

the second equal signs only hold true, if we have a pure state for which the density matrix reads $\rho = |\Psi\rangle\langle\Psi|$. The term “quasi” refers to the fact that the Wigner distribution can take negative values which usually occur in regions of small scale oscillations and indicate a non-classical, purely wave-type behavior. These small regions are shielded by the uncertainty principle and disappear in the classical limit.

For classical optics, the wavefunction corresponds to the electric field, and its absolute value squared is proportional to the intensity of the wave. Hence, integrating out one of the arguments of the Wigner function gives the intensity or the momentum distribution of the wave.

Husimi Distribution on the Fiber Boundary

For our three-dimensional fiber we use the more convenient Husimi distribution H (not to be confused with a Hamiltonian), which is basically the Wigner distribution smoothed by the convolution with a Gaussian-shaped minimum-uncertainty state $|\alpha\rangle$

$$H(\alpha) = \frac{1}{\pi} \langle \alpha | \rho | \alpha \rangle = \frac{1}{\pi} |\langle \alpha | \Psi \rangle|^2, \quad (2.2.23)$$

where the second equal sign holds true for a pure state whose density matrix reads $\rho = |\Psi\rangle\langle\Psi|$. This smoothing is the reason for its non-negative definiteness, but even if it is bounded and non-negative it is not an actual probability distribution, since different coherent states are not orthogonal, $\langle \alpha_n | \alpha_m \rangle \neq \delta_{nm}$, and thus they do not represent two disjoint possibilities. However, since it is positive definite and numerically easier to calculate than the Wigner distribution, it is a standard tool for representing phase spaces in billiard systems.

The next step is to find an expression which is analogous to the classical PSS in Birkhoff coordinates. In wave simulations we have to deal with the problem, that in billiard systems with hard walls, the boundary is a nodal line, i.e., the wave function vanishes there, and thus $H(\alpha)$ would be zero. As explained earlier, we have a finite but very high potential well, and hence the same argument applies. To resolve this, we can expand the wave function at a position close to the boundary [13], where $r = |\vec{r}| \approx r_{\text{fib}}$,

$$\Psi(\vec{r})|_{r \approx r_{\text{fib}}} = \underbrace{\Psi(\vec{r})|_{r=r_{\text{fib}}}}_{\approx 0} + \frac{\partial \Psi(\vec{r})}{\partial r} \bigg|_{r=r_{\text{fib}}} (r - r_{\text{fib}}) + \mathcal{O}((r - r_{\text{fib}})^2). \quad (2.2.24)$$

To first order, we can thus represent the wave function on the circular part of the boundary by its normal derivative

$$u(s) \equiv \frac{\partial \Psi(\vec{r})}{\partial r} \bigg|_{r=r_{\text{fib}}} = \left(\vec{\nabla} \Psi \cdot \hat{n} \right)_{r=r_{\text{fib}}}, \quad (2.2.25)$$

which only depends on the normalized arc length $s = \varphi/\varphi_{\max}$ (see subsection 2.1.1). This expression is usually called boundary function, and it can be written in a more general way for arbitrary, non-circular geometries [19]

$$u(s) = \vec{\nabla}\Psi(\vec{r}(s)) \cdot \hat{n}(s) , \quad (2.2.26)$$

where $\vec{r}(s)$ stands for a point on the boundary parametrized by the arc length. The Husimi distribution is then given by [6]

$$H(\varphi_0, L_0) = \left| \int_{-1}^1 ds \langle \varphi_0, L_0 | s \rangle u(s) \right|^2 , \quad (2.2.27)$$

where $-\varphi_{\max} < \varphi_0 < \varphi_{\max}$, $-L_{\max} < L_0 < L_{\max}$ and $L_{\max} = r_{\text{fib}} n_{\text{co}} k_t$. The configuration state representation of the minimum-uncertainty state is given by

$$\langle s | \varphi_0, L_0 \rangle = \left(\frac{1}{\pi\sigma} \right)^{1/4} \exp \left[-\frac{(\varphi - \varphi_0)^2}{2\sigma^2} + iL_0(\varphi - \varphi_0) \right] . \quad (2.2.28)$$

with $\sigma = \sqrt{\varphi_{\max}/L_{\max}}$. This Husimi distribution is now calculated at the boundary at a given value of z , but in order to get the full phase space representation, we calculate the mean Husimi distribution over all propagation steps

$$\bar{H}(\varphi_0, L_0) = \frac{1}{N_s} \sum_{N=0}^{N_s} H_N(\varphi_0, L_0) , \quad (2.2.29)$$

where N_s is the number of propagation steps and H_N is the Husimi distribution at step N .

2.2.4 Scattering Formalism

A general tool for calculating the propagation of wavefronts is the scattering matrix which consists of transmission and reflection matrices and fully describes the asymptotics of a scattering process. In our case of a perfect straight fiber without scattering regions, no reflections occur, and the transmission matrix in mode basis is diagonal consisting just of the phase factors in Eq. (2.2.13), which describe the propagation through the system. Since we will also study the case of fiber imperfections (see subsection 3.1.4), we will give a brief overview of the used scattering formalism, and based on that, we will analytically derive the transmission matrix for the case of a perfect straight fiber. For a two-port system the scattering matrix is given by

$$S = \begin{pmatrix} r & t' \\ t & r' \end{pmatrix} \quad (2.2.30)$$

and relates the mode coefficient vectors of incoming and outgoing states $\vec{\phi}$ and $\vec{\psi}$ like

$$\begin{pmatrix} \vec{\psi} \\ \vec{\psi}' \end{pmatrix} = S \begin{pmatrix} \vec{\phi} \\ \vec{\phi}' \end{pmatrix}, \quad (2.2.31)$$

where the absence/presence of a prime denotes quantities for the input/output facet. The transmission and reflection matrix can be calculated via the *Fisher-Lee relations* [20]:

$$t_{nm}(k_0) = 2i\sqrt{\beta_{z,n}\beta_{z,m}} \int_{A_{\text{out}}} d^2r_{\text{out}} \int_{A_{\text{in}}} d^2r_{\text{in}} \chi_n^*(\vec{r}_{\text{out}}) G^+(\vec{r}_{\text{out}}, \vec{r}_{\text{in}}; k_0) \chi_m(\vec{r}_{\text{in}}), \quad (2.2.32)$$

$$r_{nm}(k_0) = -\delta_{nm} + 2i\sqrt{\beta_{z,n}\beta_{z,m}} \int_{A_{\text{in}}} d^2r'_{\text{in}} \int_{A_{\text{in}}} d^2r_{\text{in}} \chi_n^*(\vec{r}'_{\text{in}}) G^+(\vec{r}'_{\text{in}}, \vec{r}_{\text{in}}; k_0) \chi_m(\vec{r}_{\text{in}}). \quad (2.2.33)$$

Here t_{nm} and r_{nm} stand for the transmission and reflection from mode m to mode n , where $\chi_n(\vec{r})$ are the intensity-normalized transverse profiles of the modes, i.e., solutions of Eq. (2.2.5), and $G^+(\vec{r}_{\text{out}}, \vec{r}_{\text{in}}; k_0)$ is the outgoing or retarded Green's function which describes the propagation from \vec{r}_{in} to \vec{r}_{out} for a given wavenumber k_0 .

The Green's function of the Schrödinger equation $(E - H)\psi = 0$ for a given energy E is given by $G^\pm(E) = \lim_{\epsilon \rightarrow 0} (1E - H \pm i\epsilon)^{-1}$, where the sign in front of ϵ determines if the Green's function is retarded (+) or advanced (-). To get an equivalent expression for the Helmholtz equation we rewrite Eq. (2.2.1) to

$$\{n_{\text{co}}^2 k_0^2 - [-\Delta + k_0^2(n_{\text{co}}^2 - n^2(\vec{r}))]\} \psi = 0, \quad (2.2.34)$$

where we have added zero in terms of $\pm n_{\text{co}}^2 k_0^2$. The Green's function of the Helmholtz equation is now given by

$$G^\pm(k_0) = \lim_{\epsilon \rightarrow 0} (\mathbb{1} \beta_0^2 - \mathcal{H} \pm i\epsilon)^{-1} . \quad (2.2.35)$$

with $\mathcal{H} = -\Delta + k_0^2(n_{\text{co}}^2 - n^2(\vec{r}))$ being the differential operator which replaces the Hamiltonian. Next, we want to use the Green's function's spectral representation and thus we insert a complete set of eigenstates of \mathcal{H} using the longitudinal normalization to a δ -distribution (see Eq. (2.2.8)). Letting the operators act on those eigenstates yields

$$\begin{aligned} G^+(\vec{r}_2, \vec{r}_1; k_0) &= \lim_{\epsilon \rightarrow 0} \frac{\sum_n \int d\beta_{z,n} \frac{1}{\sqrt{2\pi}} \chi_n^*(\vec{r}_1) e^{-i\beta_{z,n} z_1} \frac{1}{\sqrt{2\pi}} \chi_n(\vec{r}_2) e^{i\beta_{z,n} z_2}}{\beta_0^2 - \beta_{t,n}^2 - \beta_{z,n}^2 + i\epsilon} \\ &= \sum_n \chi_n^*(\vec{r}_1) \chi_n(\vec{r}_2) \underbrace{\lim_{\epsilon \rightarrow 0} \frac{1}{2\pi} \int d\beta_{z,n} \frac{e^{i\beta_{z,n}(z_2 - z_1)}}{(\beta_0^2 - \beta_{t,n}^2) - \beta_{z,n}^2 + i\epsilon}}_{G_0^+(z_2, z_1; \sqrt{k_0^2 - k_{t,n}^2})} \end{aligned} \quad (2.2.36)$$

where the last term is just the one-dimensional Green's function describing the free propagation from z_1 to z_2 . Applying Cauchy's residue theorem, the latter evaluates to [21]

$$G_0^+(z_2, z_1; \sqrt{k_0^2 - k_{t,n}^2}) = \frac{-i}{2\beta_{z,n}} e^{i\beta_{z,n}|z_2 - z_1|} , \quad (2.2.37)$$

where the Green's function for the whole system is then

$$G^+(\vec{r}_2, \vec{r}_1; k_0) = \sum_n \frac{-i}{2\beta_{z,n}} \chi_n^*(\vec{r}_1) \chi_n(\vec{r}_2) e^{i\beta_{z,n}|z_2 - z_1|} . \quad (2.2.38)$$

Inserting this expression into Eq. (2.2.32) and using the orthogonality of the transverse fiber modes, we see that our transmission matrix becomes diagonal in case of a perfect translational invariance with respect to z , as already mentioned in the introduction of this subsection,

$$t_{nm} = e^{i\beta_{z,n} l_{\text{fib}}} \delta_{nm} . \quad (2.2.39)$$

2.2.5 Wigner-Smith Time-Delay Operator

The scattering matrix, which has been introduced in the last subsection, can be used to construct the so-called *Wigner-Smith time-delay operator* [9, 10],

$$Q = i \frac{\partial S^\dagger}{\partial \omega} S = -i S^\dagger \frac{\partial S}{\partial \omega} . \quad (2.2.40)$$

As already mentioned, the application of the concept of time-delay to waveguide systems can give rise to particlelike states as shown in [11]. For the search of particlelike states in our fiber system, we restrict ourselves to the use of the transmission matrix only, since there is almost no reflection. Thus, we use the operator

$$q = -it^{-1} \frac{\partial t}{\partial \omega} , \quad (2.2.41)$$

rather than Eq. (2.2.40). Since the transmission matrix is often subunitary, e.g. in the presence of scatterers or loss, we have also replaced t^\dagger by t^{-1} [22], but in case of a perfect straight fiber without scatterers $t^\dagger = t^{-1}$. In this case, the transmission matrix is also diagonal in the basis of eigenstates of the Helmholtz equation as derived in the preceding subsection. As a consequence $[t, q] = 0$ and hence they share the same eigenbasis (2.2.8) which are just the fiber modes which do not feature the desired beam-like behavior.

To resolve this problem, a transformation will be introduced in subsection 3.1.2, where the representation of the transmission matrix in an incomplete subset of eigenvectors of another Hermitian operator causes it to be non-square in general. Since the inverse of a non-square matrix does not exist, one can utilize a singular value decomposition and construct an effective pseudo-inverse, as we will now demonstrate. Given that our transmission matrix in mode basis is a $n_{\text{out}} \times n_{\text{in}}$ matrix we can decompose it into

$$t = U \Sigma V^\dagger , \quad (2.2.42)$$

where U is a $n_{\text{out}} \times n_{\text{out}}$ matrix which contains column-wise the left-singular vectors of t and V is a $n_{\text{in}} \times n_{\text{in}}$ matrix which contains column-wise the right singular vectors of t . The singular values which can be seen as a generalization of the eigenvalues for non-quadratic matrices can be found in the diagonal of the $n_{\text{out}} \times n_{\text{in}}$ matrix Σ . Due to the representation of the transmission matrix in an incomplete basis, some singular values can get less than one, even though the corresponding states are physically fully transmitted. This is caused by the choice of these incomplete subsets which imposes a restriction in terms of the corresponding eigenvalues on the states at the fiber facets, where singular vectors of t that do not fulfill this restriction feature a singular value less than one. Thus, we pick those singular values ς_i and corresponding left and right singular vectors contained in u and v ,

which are close to 1 up to some ϵ , i.e. $|\varsigma_i - 1| \leq \epsilon$, which we have chosen to be 10^{-3} . We can then construct the pseudo-inverse of the projected transmission matrix

$$t^{-1} = v (u^\dagger t v)^{-1} u^\dagger = v \sigma^{-1} u^\dagger, \quad (2.2.43)$$

where $(\sigma^{-1})_{ij} = 1/\varsigma_i$. Looking at the expression for the time-delay operator, we notice that it further contains the derivative of the transmission matrix which also has to be projected onto this subspace. With the projection operators onto this subspace of left and right singular vectors of the transmission matrix, $P_u = uu^\dagger$ and $P_v = vv^\dagger$, we arrive at the following expression

$$q = -iv (u^\dagger t v)^{-1} u^\dagger u u^\dagger \frac{\partial t}{\partial \omega} v v^\dagger. \quad (2.2.44)$$

Apart from this method which will be used in subsection 3.1.2, we will also generalize the concept of time-delay to the concept of *dependence shift* in subsection 3.1.3 and apply it to a two-dimensional fiber toy model.

Coming back to the time-delay operator, its eigenstates, which are also called *principal modes*, have the nice feature of being invariant to first order under a variation of the frequency. This has been shown theoretically in [23] in case of a q -operator which contains t^\dagger rather than t^{-1} . Due to the mentioned subunitarity of the transmission matrix in real fiber systems, a proof for the case of t^{-1} has been given in [22], where the invariance of principal modes under modal dispersion to first order has also recently been experimentally shown in [24]. However, a more elegant theoretical proof of this feature can be obtained by expressing the shift in frequency for a certain mode coefficient vector at the output facet by a Taylor series [25],

$$\begin{aligned} \vec{\psi}(\omega_0 + \Delta\omega) &= \vec{\psi}(\omega_0) + \left. \frac{\partial \vec{\psi}}{\partial \omega} \right|_{\omega_0} \Delta\omega + \mathcal{O}(\Delta\omega^2) \\ &\approx t(\omega_0) \vec{\phi} + \left. \frac{\partial t(\omega)}{\partial \omega} \right|_{\omega_0} \vec{\phi} \Delta\omega, \end{aligned} \quad (2.2.45)$$

where we have neglected terms of the order of $\Delta\omega^2$. Furthermore, we have used $\vec{\psi} = t\vec{\phi}$ and assumed a constant frequency-independent input pattern $\vec{\phi}$. Next, we demand that our change to first order has to be parallel to our output vector at ω_0 , i.e., they can only differ by a global amplitude and a global phase contained in $z \in \mathbb{C}$:

$$t(\omega_0) \vec{\phi} = z \left. \frac{\partial t(\omega)}{\partial \omega} \right|_{\omega_0} \vec{\phi}. \quad (2.2.46)$$

Rearranging and using $\tau = (iz\Delta\omega)^{-1}$ yields the eigenvalue equation

$$-it^{-1}(\omega_0) \left. \frac{\partial t(\omega)}{\partial \omega} \right|_{\omega_0} \vec{\phi} = \tau \vec{\phi}, \quad (2.2.47)$$

where the operator on the l.h.s is just given by the time-delay operator (2.2.41). To assign a meaning to its eigenvalues, τ_n , we multiply the equation above again by the transmission matrix from the left and use $\partial\vec{\phi}/\partial\omega = 0$,

$$\tau\vec{\psi} = -i \left. \frac{\partial\vec{\psi}}{\partial\omega} \right|_{\omega_0} . \quad (2.2.48)$$

Next, we decompose the output vector into a unit vector pointing in the corresponding direction in the mode coefficient space, a global amplitude and a global phase, i.e., $\vec{\psi} = \hat{\psi}|\vec{\psi}|e^{i\varphi}$, and get from Eq. (2.2.48)

$$\tau\hat{\psi}|\vec{\psi}|e^{i\varphi} = \hat{\psi}|\vec{\psi}| \left. \frac{\partial\varphi}{\partial\omega} \right|_{\omega_0} e^{i\varphi} - i\hat{\psi} \left. \frac{\partial|\vec{\psi}|}{\partial\omega} \right|_{\omega_0} e^{i\varphi} . \quad (2.2.49)$$

Here we have used that $\hat{\psi}(\omega) \approx \hat{\psi}(\omega_0)$ which is justified by the ω -independence of $\vec{\psi}$ to first order which, together with the assumption of a frequency-independent input pattern $\vec{\phi}$, has led us to the time-delay operator in Eqs. (2.2.45)-(2.2.47). The eigenvalue now reads

$$\tau = \left. \frac{\partial\varphi}{\partial\omega} \right|_{\omega_0} - i \left. \frac{\partial \ln |\vec{\psi}|}{\partial\omega} \right|_{\omega_0} . \quad (2.2.50)$$

From this relation, we can see that the real part of τ corresponds to the change in the scattering phase and can be interpreted as delay time [9], whereas the imaginary part gives the change of the transmitted intensity. Note that these derivations are valid for q as well as for Q , where for the latter, one also has to consider incoming states from the output facet of our fiber.

Chapter 3

Results

In this chapter we will apply the concepts we reviewed in the previous chapter. The experimental limitations to millimeter-sized cross section diameters of our three-dimensional D-shaped geometry make it numerically impossible to entirely simulate such a system, since the number of open modes is huge. For a rod with radius $r_{\text{fib}} = 2.5 \text{ mm}$ and a laser on wavelength $\lambda = 553 \text{ nm}$, the number of open modes can be estimated by $N_m = 2\pi A_{\text{fib}}/\lambda^2 \approx \mathcal{O}(10^9)$ [1], where A_{fib} is the area of the D-shaped cross section. One possible solution to that problem is the use of a subpart of higher excited fiber modes which correspond to the choice of a certain angle θ to the fiber axis. Even for a few degrees, however, the number of gridpoints needed to resolve the wavelengths of these eigenstates is huge, and thus numerically out of reach. Furthermore, picking a subpart highly-excited modes can give rise to problems in building localized wave packets due to the highly oscillating behavior of these states. To be able to treat the system numerically, we thus scale it down to the size of an actual multi-mode fiber, using $r_{\text{fib}} = 62.5 \text{ }\mu\text{m}$.

For simplicity, we will also consider a two-dimensional toy model of our fiber in a first step. In this model, two non-operator based approaches will be presented whose poor performance lead us to operator-based approaches, which will then also be used in the three-dimensional fully chaotic and mixed D-shaped fiber. First, we will introduce a transformation of the time-delay operator which yields particlelike states in the two-dimensional toy model, whereas this method lacks functionality in the three-dimensional fiber system due to the chaoticity caused by the D-shaped cross section. We present a generalization of the time-delay operator, though, whose eigenstates behave in a beam-like fashion in the toy model as well as in our D-shaped fiber. For all these methods the found states will be investigated in the spatial domain as well as in phase space, which will give us a deeper insight into their dynamics.

For the sake of comparison, we will then perform trajectory bundle simulations in the three-dimensional D-shaped fiber system used in our wave simulations, where we will find that spreading, together with the lack of interference, makes this trajectory bundle approach not a suitable tool for describing waves states in such small systems. However, in case of the experimentally available rods, the larger system

dimensions make interference less important. Thus, the trajectory bundle approach will serve as a good approximation and allows us to make predictions about the behavior of wave states in such systems.

3.1 Wave Dynamics in a 2D Fiber Toy Model

In this section, we study a two-dimensional toy model in a first step since the computations are less time consuming, and the methods stay the same, in principal. The z -invariant transverse potential of this toy model is given by Eq. (2.2.6) and sketched in Fig. 3.1. Because no direct comparison with an actual experimental setup is made, we choose the fiber length more or less arbitrarily to be $l_{\text{fib}} = 100r_{\text{fib}}$. Moreover, all calculations in this section are based on the usage of the system's 100 energetically lowest transverse modes, i.e., solutions to (2.2.5).

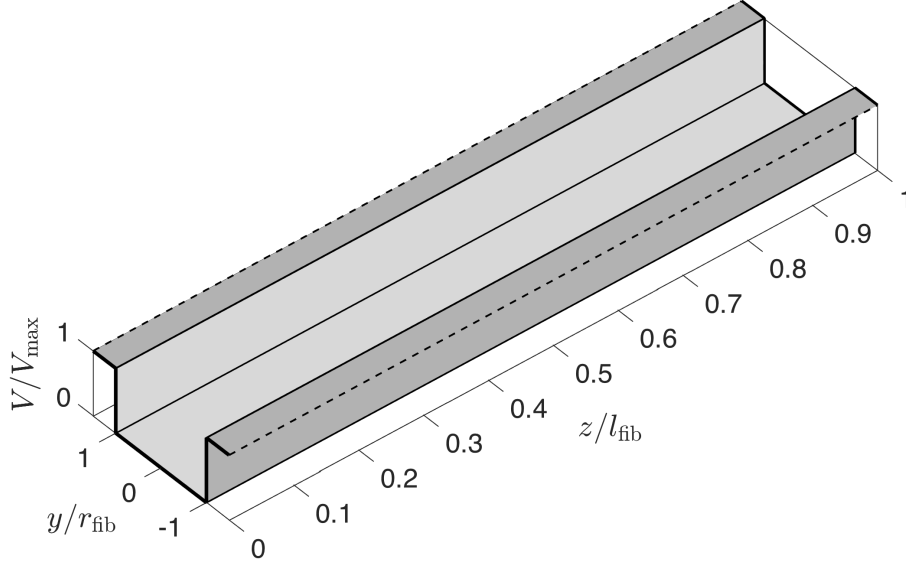


Figure 3.1: Sketch of the toy model potential which is given by a translational invariant finite potential well along the z -direction.

Because of the high difference in the indices of refraction, our finite potential well can be treated in good approximation as infinitely high. This gives us the advantage to look at our problem partly analytically, since the corresponding transverse eigenfunctions for a two-dimensional translationally invariant rectangular waveguide with hard walls are given by

$$\chi_n(y) = \sqrt{\frac{2}{d_{\text{fib}}}} \sin(k_{t,n}y) \quad , \quad (3.1.1)$$

where $k_{t,n} = \pi n/d_{\text{fib}}$, and $d_{\text{fib}} = 2r_{\text{fib}}$ is the diameter of the fiber. Experimentally, obtaining particlelike states via calculating operator eigenfunctions is not necessary since just the form of the incident wavefront is needed in order to shape it by usage of a spatial light modulator. Hence, we have also considered two non-operator based approaches in the following section.

3.1.1 Non-Operator-Based Approaches

Since one of the key-features of particlelike states is their spatial localization, we first thought of minimizing a quantity which is a measure for the area occupied by a wave, namely the spatial participation ratio (see Appendix D),

$$P(\psi) = \frac{[\int dy |\psi(y)|^2]^2}{\int dy |\psi(y)|^4} . \quad (3.1.2)$$

Notice that, like the standard deviation which is a measure for the broadness of the tails of a function, it is nonlinear and, hence, a corresponding eigenproblem does not exist. For the minimization procedure, we decompose our initial state into fiber modes and use the coefficient vectors at the input and output facet, $\vec{\phi}$ and $\vec{\psi} = t\vec{\phi}$. Numerically, we start with a random coefficient vector and minimize the functional $P(\phi) + P(\psi)$, which yields states that are localized at the input and output facet as expected, but nearly completely delocalized in between. In Fig. 3.2a one can see that the strong spatial localization causes the state to feature a broad range of momenta, which results into a Wigner distribution spread out along the k_y -axis. Apart from oscillations, the spatial localization at the output facet is also clearly visible. This effect gets even stronger if we use a higher number of modes and, therefore, this minimization procedure is not an appropriate tool for finding particlelike states.

In a second approach, we consider Glauber states whose defining equation is formally given by

$$a |\psi_\alpha\rangle = \alpha |\psi_\alpha\rangle \quad (3.1.3)$$

in which a is the annihilation or lowering operator. Since this operator is infinite dimensional in the mode basis, we cannot represent it in a finite basis, and thus we have to use the analytical solution of (3.1.3) instead of solving the eigenproblem numerically. In a quantum mechanical harmonic oscillator, Glauber states are the “most classical” ones, since the expressions for the mean position and momentum are equivalent to the classical equations of motion of a particle in a harmonic oscillator potential. These Glauber states are of the form

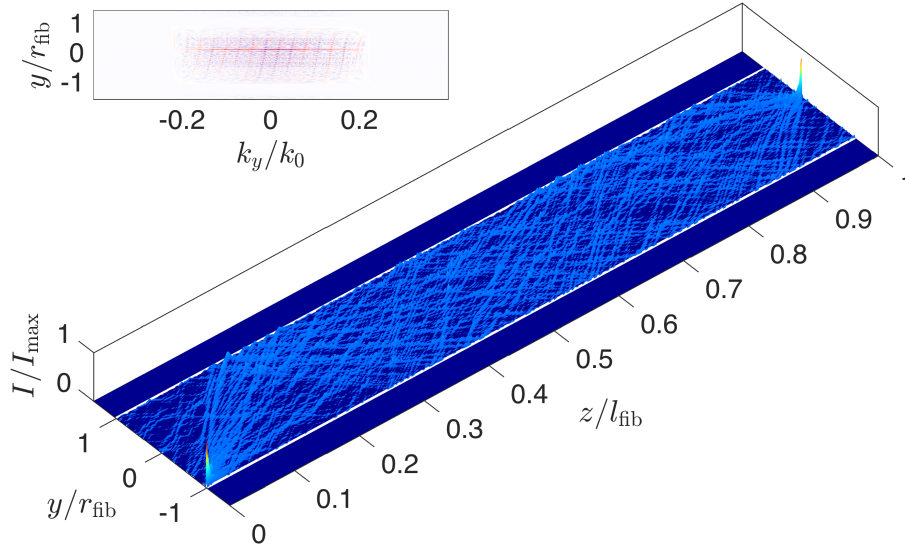
$$|\psi_\alpha\rangle = e^{-\frac{|\alpha|^2}{2}} \sum_{n=0}^{\infty} \frac{\alpha^n}{\sqrt{n!}} |\chi_n\rangle , \quad (3.1.4)$$

and applying the time-evolution operator using $\omega_n = \omega(n + 1/2)$ with ω being the eigenfrequency of the oscillator shows a nice feature of these states

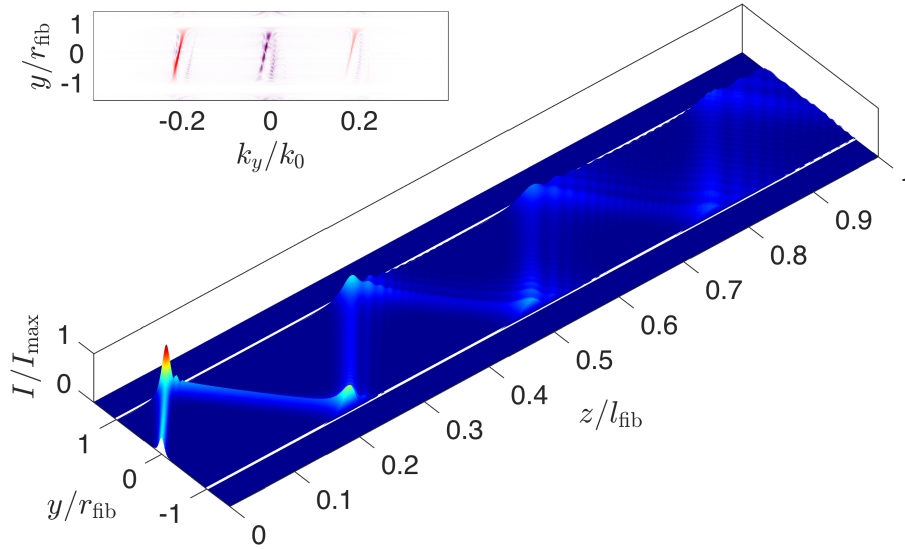
$$\begin{aligned}
 |\psi_\alpha(t)\rangle &= e^{-\frac{|\alpha|^2}{2}} \sum_{n=0}^{\infty} \frac{\alpha^n}{\sqrt{n!}} e^{-i\omega_n t} |\chi_n\rangle \\
 &= \left[e^{-\frac{|\alpha|^2}{2}} \sum_{n=0}^{\infty} \frac{(\alpha e^{-i\omega_n t})^n}{\sqrt{n!}} |\chi_n\rangle \right] e^{-\frac{i\omega t}{2}} \\
 &= |\psi_{\alpha(t)}\rangle e^{-\frac{i\omega t}{2}}
 \end{aligned} \tag{3.1.5}$$

with $\alpha(t) = \alpha \exp(-i\omega t)$. Since the time-evolution changes α by the same phase factor for every eigenstate, the Glauber state does not broaden over time which originates from the special form of this potential for which the eigenenergies are equidistant. We can now generalize the expression (3.1.4) for potential wells, but since their energy levels are not equidistant, these states will not keep the minimum uncertainty during the propagation through the system. Using the “evolution operator” $\exp(i\beta_{z,n}z)$ for classical waves with $\beta_{z,n} = \sqrt{\beta_0^2 - \beta_{t,n}^2}$, one can show that the value of $\alpha(t)$ changes every eigenstate by a different phase factor since the propagation constant $\beta_{z,n}$ cannot be separated into a n -dependent and a n -independent part like ω_n in a harmonic oscillator potential. This causes the spreading of the generalized Glauber state as shown in Fig. 3.2b. Another problem arises from the form of our potential: In an oscillator potential, the real and imaginary part of the parameter α can be associated with the mean position and mean momentum of the wave, but having a potential well makes this association invalid.

All in all, we were not able to find particlelike states in our considered two-dimensional system by numerically minimizing a nonlinear functional or by generalizing the concept of Glauber states of a harmonic oscillator. In the next subsections, we take a different approach and search for linear operators whose eigenstates show a beam-like behavior. Finding such an operator would constitute a much easier and more elegant way compared to the two approaches discussed in this subsection.



(a) State with a minimized spatial participation ratio at the input and output facet, where the high spatial localization at the facets causes complete delocalization in between due to the broad range of contributing transverse momenta. This spatial localization and delocalization in transverse momenta can be clearly seen in the Wigner function at the output facet displayed in the smaller inset at the top. Note that in contrast to the following propagation plots, here we have modified the colormap in order to make the delocalization more visible.



(b) Coherent state with $\alpha = 10 \exp(3i\pi/2)$ which is initially localized, but spreads due to the non-equidistant energy levels of the potential well. In the Wigner function, one can see that this state consists mostly of momenta around $k_y \approx -0.2k_0$, where the spreading during the propagation causes the state to also consist of momenta around $k_y \approx 0.2k_0$ at the output facet.

Figure 3.2: Propagation of given states through the system, where the insets show the corresponding Wigner distribution at the output facet in which red/blue colors stand for positive/negative values of the function.

3.1.2 Projection of the Time-Delay Operator

In this subsection, we address the problem that the eigenstates of the time-delay operator are just given by the fiber modes (2.2.8) in a perfect straight geometry due to the diagonal form of the transmission matrix. To circumvent this problem we can impose a restriction onto the transmission matrix in order to lift the degeneracy w.r.t. the angle θ , i.e. performing a rotation into a subspace spanned by the eigenvalues of another arbitrary Hermitian operator μ

$$t_\mu = M_{\text{out}}^\dagger t M_{\text{in}} , \quad (3.1.6)$$

where eigenvectors of μ are contained column-wise in M . The subscripts stand for the possible choices for different subsets at the input and output facet. Please note that a rotation into a complete set of basis states is a unitary operation and does not change the eigenstates, whereas the rotation into an incomplete subspace is not unitary since $M^\dagger M = \mathbb{1}$, but $MM^\dagger \neq \mathbb{1}$. Inserting (3.1.6) into the expression for the time-delay operator yields

$$q_\mu = -i M_{\text{in}}^\dagger t^{-1} M_{\text{out}} M_{\text{out}}^\dagger \frac{\partial t}{\partial \omega} M_{\text{in}} . \quad (3.1.7)$$

However, by making a severe restriction in terms of small subsets, we also get q_μ -eigenstates which do not fulfill this restriction and mathematically show a transmission eigenvalue less than one even though they are physically fully transmitted. To get rid of those states we just want to use those t -eigenstates, which mathematically feature a transmission close to unity. However, choosing different subsets at the input and output facet leads to the problem that our transmission matrix is no longer quadratic, and thus we cannot perform a straight-forward inversion. Given that $M_{\text{in/out}}$ consist of $n_{\text{in/out}}$ eigenvectors we instead utilize the singular value decomposition method as discussed in subsection 2.2.5, construct the effective inverse of the transmission matrix and project the derivative of t onto the “fully transmitting” subspace of singular vectors of t :

$$q_\mu = -iv (u^\dagger t v)^{-1} u^\dagger u u^\dagger \frac{\partial t}{\partial \omega} v v^\dagger . \quad (3.1.8)$$

Here we have introduced the subscript μ which denotes the operator whose eigenbasis was used for the rotation. Since this operator is quadratic, we can solve its eigenvalue problem and get eigenvectors consisting of μ -coefficients which can easily be transformed back to mode-coefficients via

$$\vec{\phi} = M_{\text{in}} \vec{\phi}_\mu . \quad (3.1.9)$$

Now we have all ingredients to try different operator eigenbases, where a first logical step in the sense of spatial localization is to restrict the time-delay operator to a

certain region in the cross section. For this purpose, we have to use the transverse position operator for which an analytical expression can be written down in the approximation of an infinitely high potential well,

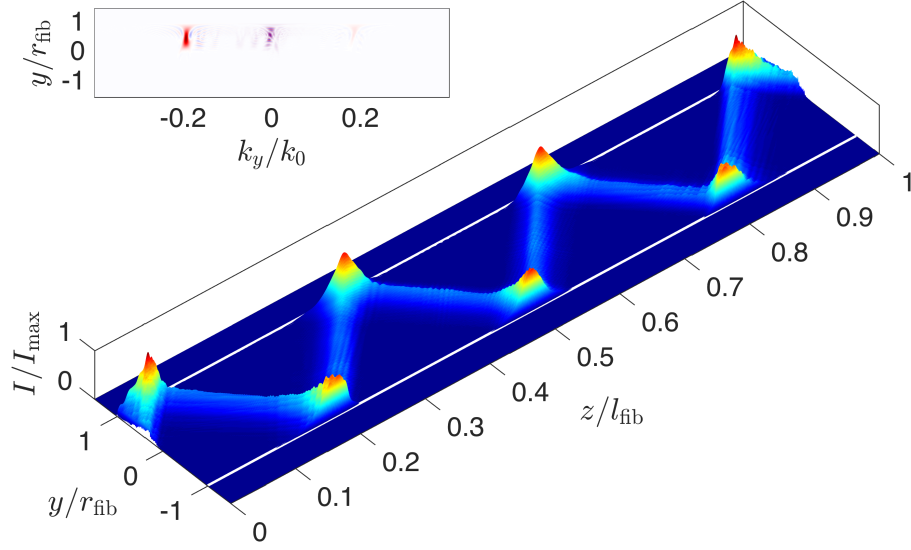
$$y_{mn} = \int dy \chi_m^*(y) y \chi_n(y) = \frac{4d_{\text{fib}} [(-1)^{m+n} - 1] mn}{\pi^2(m^2 - n^2)^2} . \quad (3.1.10)$$

The eigenstates of this operator are localized peaks which get narrower the more modes we take into account. In the limit of an infinite number of propagating modes, they become δ -peaks. One disadvantage of using this operator is that we have to pick a subspace corresponding to a certain reasonably narrow range of y -values manually. Depending on the choice of the subset we can get q_y -eigenstates that consist of single branches as desired (see Fig. 3.3a), whereas we can also get states that feature two branches due to the degeneracy of the delay-times with respect to the sign of the transverse momentum (see Fig. 3.3b).

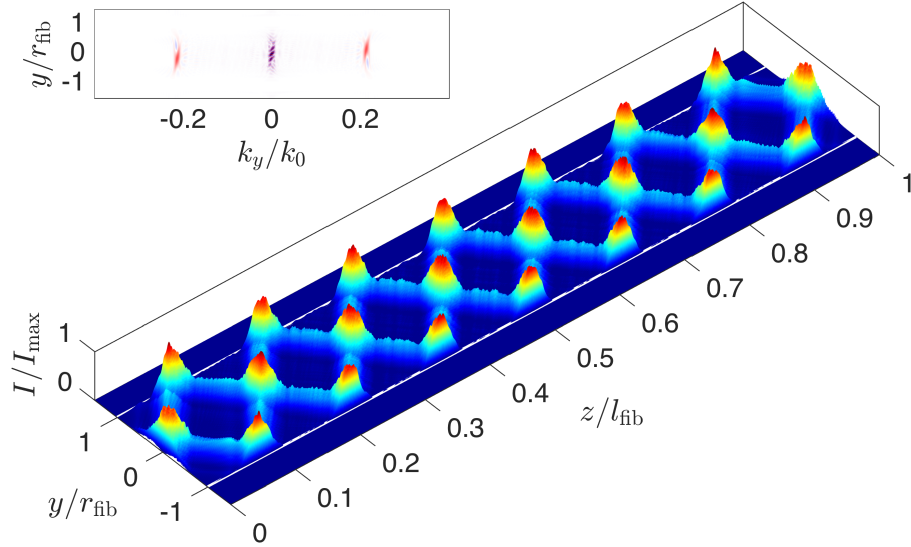
This degeneracy can be lifted by using a subset of eigenstates of the transverse momentum operator, whose analytical expression in the mode basis in case of an infinitely high potential well is given by

$$k_{y,mn} = \int dy \chi_m^*(y) (-i\partial_y) \chi_n(y) = \frac{2i [(-1)^{m+n} - 1] mn}{d_{\text{fib}}(m^2 - n^2)} . \quad (3.1.11)$$

As shown in Fig. 3.4, using the subset of eigenstates with $k_y > 0$ instead of $y > 0$ lifts the mentioned degeneracy and yields exclusively states with single branches as desired. Furthermore, q_{k_y} -eigenstates with a high time-delay automatically get narrower in the direction perpendicular to the propagation direction in order to fulfill the imposed restriction, where their width gets bigger for a smaller time-delay. Moreover, it is experimentally easily possible to inject plane waves, i.e., k_y -eigenstates, into a fiber, which makes this method more favorable compared to the use of the y -operator. However, as we will see, in three dimensions the additional degree of freedom causes problems since $[k_x, k_y] \neq 0$ due to our D-shaped cross section which permits us to do subsequent rotations into subsets of k_x - and k_y -eigenstates. Thus, we continue the search for other appropriate operators which are based on the transmission matrix.

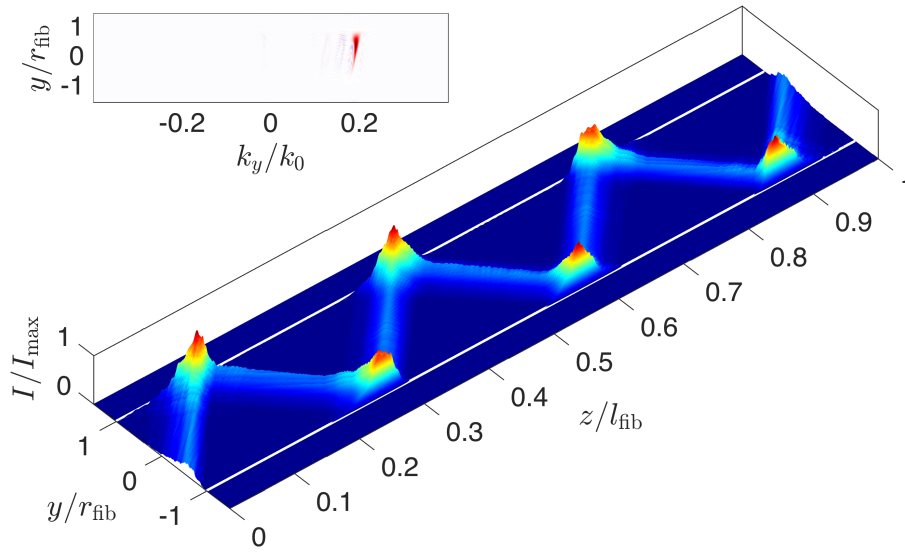


(a) Eigenstate of q_y with the highest time-delay using the subset of $y > 0$, where the beam-like behavior can be clearly seen. Note, that the choice of the subset $y > 0$ yields only a single branch as desired which results in a Wigner distribution at the output facet with a single peak at $k_y/k_0 \approx -0.2$.

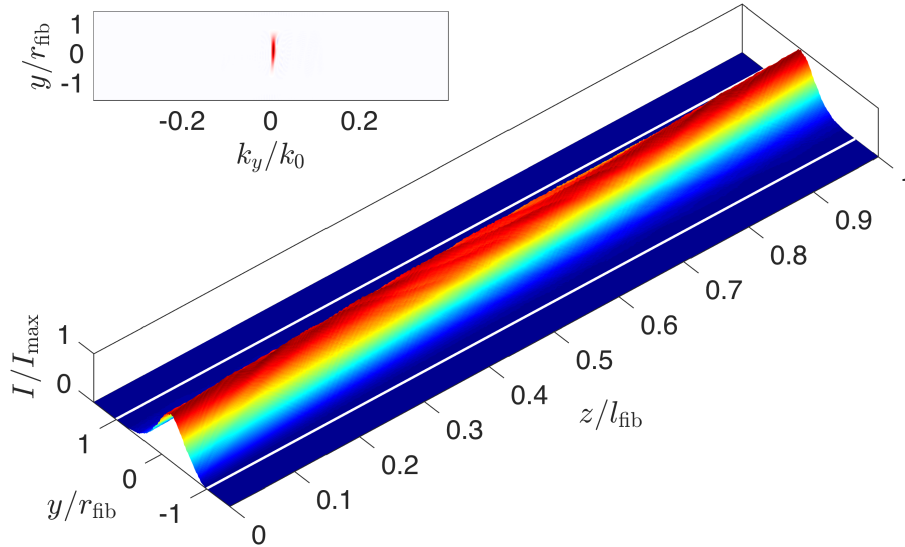


(b) Eigenstate of q_y with the highest time-delay using the subset of $-0.6 < y/r_{\text{fib}} < 0.6$. This choice results in two branches with similar delay times due to the degeneracy w.r.t. the sign of the transverse momentum which can also be clearly seen in the Wigner function at the output facet in form of two peaks around $k_y/k_0 \approx \pm 0.2$.

Figure 3.3: Propagation of given states through the system, where the insets show the corresponding Wigner distribution at the output facet in which red/blue colors stand for positive/negative values of the function.



(a) Eigenstate of q_{k_y} with the highest time-delay using the subset of $k_y > 0$. The choice of this subset lifts the degeneracy with respect to the sign of k_y and results exclusively in states with single branches. This single branch yields a Wigner distribution at the output facet which features a single peak at $k_y \approx 0.2k_0$.



(b) Eigenstate of q_{k_y} with the lowest time-delay using the subset of $k_y > 0$, where the small q_{k_y} -eigenvalue results in a small transverse momentum. Again, the choice of this subset yields a state consisting of a single branch which shows up in the Wigner distribution in form of a single peak, but the restriction $k_y > 0$ at the input and output facet allows broader transverse profiles for smaller delay times.

Figure 3.4: Propagation of given states through the system, where the insets show the corresponding Wigner distribution at the output facet in which red/blue colors stand for positive/negative values of the function.

3.1.3 Introducing the Dependence Shift (DEFT) Operator

In this subsection, we introduce the *dependence shift* (DEFT) operator as a generalization of the Wigner-Smith time-delay operator by replacing the derivative w.r.t. ω by the derivative w.r.t. an arbitrary continuous parameter ξ , i.e.

$$D = -iS^\dagger \frac{\partial S}{\partial \xi} . \quad (3.1.12)$$

As shown in subsection 2.2.5, the eigenstates of this operator are then stable under a variation of this parameter to first order instead of the frequency ω . The next important task is the choice of an appropriate continuous parameter. For this we recall, that the ω -derivative leads to states with a certain propagation time. Since time and frequency are conjugate quantities, we use the derivative w.r.t. the fiber position in order to get states with a well-defined difference in momenta at the input and output facet in the shift direction. As we will show later, shifting the fiber in the transverse direction will result in states that stay collimated during the propagation through the system in order to have a well-defined transverse momentum difference. Moreover, we again restrict ourselves to the use of the transmission matrix and introduce the operator

$$d = -it^\dagger \frac{\partial t}{\partial \xi} , \quad (3.1.13)$$

where ξ now denotes the shift of the fiber's position into a certain direction. In order to show that d -eigenstates correspond to well-defined momentum differences, we assume a small fiber displacement in the \hat{r} -direction such that we can approximate the differential by the finite-difference quotient

$$\frac{\partial t}{\partial \xi} \approx \frac{t(\xi_0 + \Delta\xi) - t(\xi_0)}{\Delta\xi} , \quad (3.1.14)$$

where $t(\xi_0)$ is the unshifted transmission matrix. To get the shifted transmission matrices, we make use of the translation operator

$$\begin{aligned} t(\xi_0 + \Delta\xi) &= e^{-i\vec{k} \cdot \hat{r} \Delta\xi} t(\xi_0) e^{+i\vec{k} \cdot \hat{r} \Delta\xi} \\ &= \left[\mathbb{1} - i \vec{k} \cdot \hat{r} \Delta\xi + \dots \right] t(\xi_0) \left[\mathbb{1} + i \vec{k} \cdot \hat{r} \Delta\xi - \dots \right] \\ &= t(\xi_0) - i \Delta\xi \vec{k} \cdot \hat{r} t(\xi_0) + i \Delta\xi t(\xi_0) \vec{k} \cdot \hat{r} + \mathcal{O}(\Delta\xi^2) . \end{aligned} \quad (3.1.15)$$

Putting everything together, neglecting terms of $\mathcal{O}(\Delta\xi^2)$ and writing $t(\xi_0) = t$ for simplicity, we arrive at

$$d = - \left(t^\dagger \vec{k} \cdot \hat{r} t - \vec{k} \cdot \hat{r} \right) . \quad (3.1.16)$$

Note that this proof is entirely based on operators which are not represented in any basis. To assign a meaning to its eigenvalues we consider an input vector $\vec{\phi}$ in

mode basis and build the expectation value

$$\begin{aligned}\vec{\phi}^\dagger d\vec{\phi} &= -\left(t\vec{\phi}\right)^\dagger \vec{k}\cdot\hat{r}\left(t\vec{\phi}\right) + \vec{\phi}^\dagger \vec{k}\cdot\hat{r}\vec{\phi} \\ &= -\langle\vec{k}\cdot\hat{r}\rangle_{\text{out}} + \langle\vec{k}\cdot\hat{r}\rangle_{\text{in}} .\end{aligned}\tag{3.1.17}$$

Bear in mind that the transmission matrix relates flux coefficients and hence the eigenvalues are not the physical momenta of our wave states. For simplicity, however, we will speak of momentum differences and denote the d -eigenvalue as $\delta\kappa$. Since our system features translational invariance along z , shifting in this direction will maintain the diagonal structure of the transmission matrix which yields the fiber modes as d -eigenstates. Thus, we shift the fiber in the transverse direction, where states with a high $|\delta\kappa|$ show a beam-like behavior since they are restricted to a small range of transverse momenta in order to have a well-defined momentum difference between the input and output facet, much analogous to the grouping of trajectories with similar delay times in case of particlelike states found by the time-delay operator [11]. States with a smaller $|\delta\kappa|$ in turn feature less well-defined transverse momenta at the fiber facets and are thus generally not particlelike.

To obtain the shifted transmission matrices in Eq. (3.1.14) numerically, we shift the entire fiber for the distance of one transverse (e.g., y -direction for the two-dimensional toy model) gridpoint while keeping the input the same, which introduces a certain amount of mode mixing whose degree is determined by the matching of the modes and their derivatives at the input and output facets very similar to transfer matrix-concepts. Like in [22], we will neglect the small amount of reflection occurring at the fiber facets, which avoids the problem of solving a set of equations via matrix inversion, where the matrix which has to be inverted is highly singular due to the small amount of mode mixing. Denoting a region left/right of the input facet with the superscript L/R we have to ensure the continuity of the transverse electric field at the interface $z = 0$

$$\left[\sum_n f_n^L e^{i\beta_{z,n}^L z} \chi_n^L(\vec{r})\right]_{z=0} = \left[\sum_n f_n^R e^{i\beta_{z,n}^R z} \chi_n^R(\vec{r})\right]_{z=0}, \tag{3.1.18}$$

where the coefficients $f_n^{L,R}$ already contain the longitudinal normalization factor. Also note that we have replaced the transverse coordinate y by the vector \vec{r} in the transverse plane since this calculation will also be used in the three-dimensional fiber system. Multiplication of Eq. (3.1.18) by $\chi_m^{R*}(\vec{r})$, integrating over the considered fiber cross section, and using the orthogonality relation (2.2.10) of the transverse fiber modes gives us the relation

$$\vec{f}^R = O\vec{f}^L, \tag{3.1.19}$$

where O is the overlap or coupling matrix between the transverse fiber modes whose elements read

$$O_{mn} = \int d^2r \chi_m^{R*}(\vec{r}) \chi_n^L(\vec{r}). \tag{3.1.20}$$

The same arguments apply to the output facet and, together with the unshifted transmission matrix t which is diagonal in mode basis, we can get the shifted transmission matrices by

$$t_{\pm} = O_{\pm}^{\dagger} t O_{\pm} , \quad (3.1.21)$$

where $+/-$ denotes the shifting in positive/negative \hat{r} -direction in the transverse plane. The dependence shift operator for transverse shifting in our two-dimensional toy model is thus given by

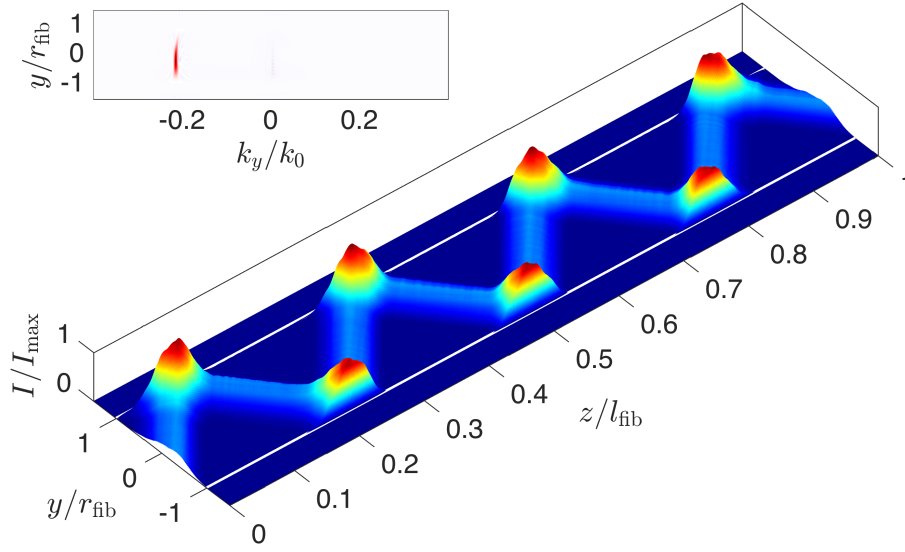
$$d_y = -it^{-1} \frac{(t_+ - t_-)}{2\Delta y} , \quad (3.1.22)$$

where we have used a central difference approximation for the continuous derivative, with Δy being the spacing between two transverse gridpoints.

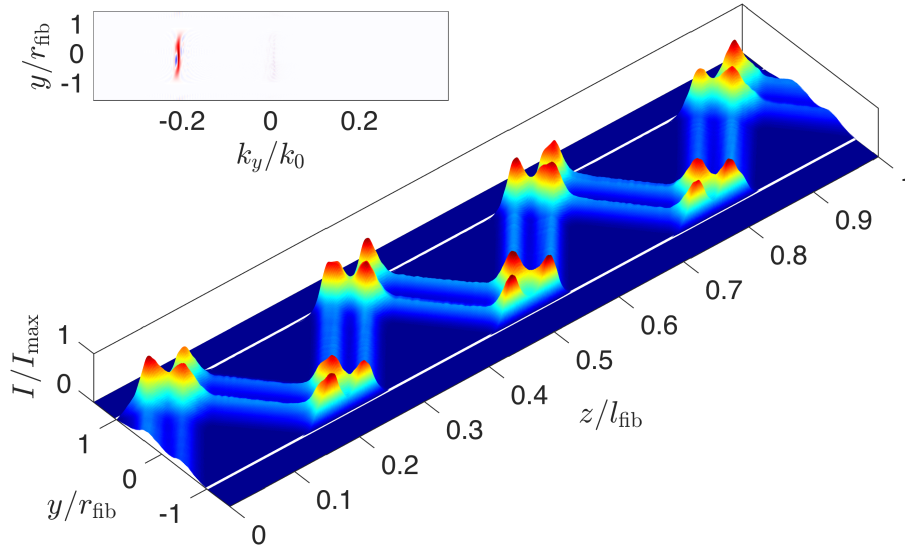
In Fig. 3.5a and 3.5b eigenstates with the highest and second highest eigenvalue $\delta\kappa$ are shown. Due to their well-defined transverse momentum difference between the input and output facet, these states stay collimated during the propagation through the system, where the sign of the eigenvalue corresponds nicely to the relation found in (3.1.16). Furthermore, similar to the q -eigenstates the d -eigenstates feature a quantization in the direction perpendicular to the beam propagation (see Fig. 3.5b). The origin of this quantization has not yet been fully understood and is subject of current research [26]. In Fig. 3.6a also an eigenstate with a small $\delta\kappa$ is shown, where one can see the complete delocalization in position as well as in momentum space. An eigenstate with $\delta\kappa \approx 0$ features several branches (see Fig. 3.6b) whose sum of transverse momenta is close to zero at the input facet as well as at the output facet.

As we have shown in subsection 2.2.5, the time-delay eigenstates are invariant under a frequency change to first order. The DEFT-eigenstates we generated, however, are by construction invariant to first order under a transversal shift of the entire fiber. Regarding pulse transmission, we will also investigate the frequency dependence of the particlelike d -eigenstates by calculating the spectral correlation function which is a measure for the change of a given state dependent on a change of the initial frequency. Given our coefficient vector in the mode basis at the input facet, $\vec{\phi}$, the corresponding coefficient vector at the output facet is $\vec{\psi}(\omega) = t(\omega)\vec{\phi}$. Note that in general, also the shape of the fiber modes and thus the coefficient vector depends on ω , but a slight change in frequency, i.e., in the height of the potential well, changes the shape of the fiber modes in a negligible way, which enables us to use $\vec{\phi} \neq \vec{\phi}(\omega)$. The spectral correlation function for a frequency detuning of $\Delta\omega$ reads

$$C(\Delta\omega) = \frac{|\vec{\psi}(\omega_0 + \Delta\omega) \cdot \vec{\psi}(\omega_0)|}{|\vec{\psi}(\omega_0 + \Delta\omega)| \cdot |\vec{\psi}(\omega_0)|} . \quad (3.1.23)$$

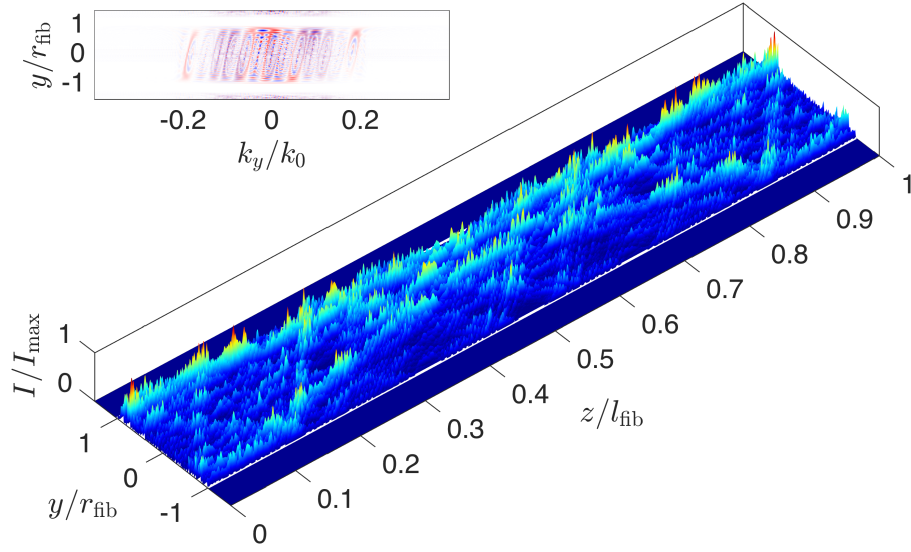


(a) Eigenstate of d with the highest momentum difference $\delta\kappa$ between the input and output facet which behaves in a beam-like fashion and features a Wigner function at the output facet with a single peak at $k_y/k_0 \approx -0.2$.

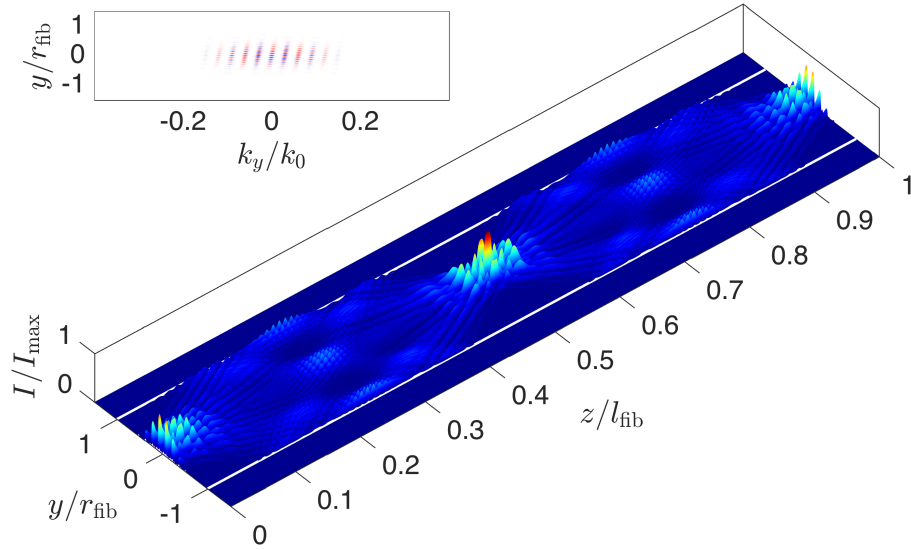


(b) Eigenstate of d with the second highest momentum difference $\delta\kappa$ between the input and output facet which is also localized in phase space at $k_y/k_0 \approx -0.2$. Moreover, a quantization transverse to the direction of the beam propagation can be seen, which has also been observed for particlelike states formed by the time-delay operator.

Figure 3.5: Propagation of given states through the system, where the insets show the corresponding Wigner distribution at the output facet in which red/blue colors stand for positive/negative values of the function.



(a) Eigenstate of d with a small momentum difference $\delta\kappa$ between the input and output facet which is completely delocalized in position space as well as in momentum space.



(b) Eigenstate of d with the smallest momentum difference $\delta\kappa$ between the input and output facet. Since $\delta\kappa$ is nearly zero, this state consists of several branches whose sum of transverse momenta approximately cancel each other out at each fiber facet. These branches also show up in the Wigner function, where they have to be symmetric around $k_y = 0$ in order to feature a transverse momentum at the output facet which is approximately zero.

Figure 3.6: Propagation of given states through the system, where the insets show the corresponding Wigner distribution at the output facet in which red/blue colors stand for positive/negative values of the function.

In Fig. 3.7 one can see the mean correlation function of fiber modes, random states and particlelike eigenstates of the DEFT-operator. Fiber modes have an infinitely broad correlation due to the lack of mode mixing, whereas the correlation of random states decays rapidly. Compared to the latter, the DEFT-eigenstates show a very broad correlation which opens up the possibility to inject particlelike time-dependent pulses consisting of a certain frequency composition into our fiber, where the usage of a broader frequency spectrum would result in pulses that are temporally more localized. Even more important is the fact that this ω -invariance makes it possible to transmit arbitrary temporal pulse shapes through the system. Furthermore, the spectral correlation of time-delay eigenstates is also shown in Fig. 3.7. Since these eigenstates are by construction invariant to first order under a frequency shift, they are overall better correlated than our particlelike DEFT-eigenstates.

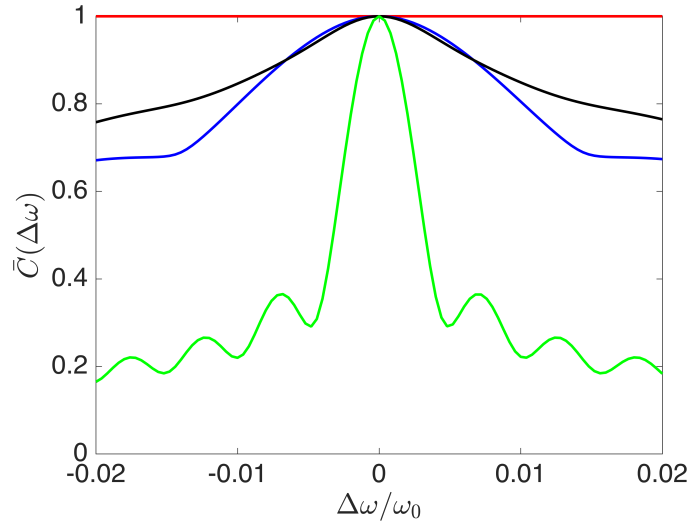


Figure 3.7: Mean correlation function all fiber modes (red curve), the ten best d -eigenstates with the highest $|\delta\kappa|$ (blue curve), the ten q_k -eigenstates with the highest time-delay fulfilling the restriction $k_y > 0$ at the input and output facet (black curve), and thousand random states (green curve). Here one can see, that the modes feature an infinitely broad correlation function, whereas the correlation function of random state decays rapidly. Moreover, the q_k -eigenstates feature an overall larger correlation width compared to the d -eigenstates, where the latter are slightly better correlated in the range $-0.0075 < \Delta\omega/\omega_0 < 0.0075$.

3.1.4 Impact of Imperfections

As we have seen in the last subsection, the fiber modes have an infinite spectral correlation, but adding imperfections to the fiber could destroy that feature and make our DEFT-eigenstates a better choice for sending pulses through a fiber. Note that in the presence of scattering elements, one could also use the concept of the Wigner-Smith time-delay operator, where the eigenstates are by construction invariant under a slight frequency shift to first order. However, the construction of the time-delay operator requires phase-coherent measurements of the transmission matrix for different frequencies, whereas the subclass of DEFT introduced in subsection 3.1.3 is based on shifting the entire fiber while keeping the frequency the same which is experimentally more easily realizable in certain cases. Furthermore, the application of DEFT for finding particlelike wavefronts in scattering systems is also a nice demonstration of this method in more realistic systems even though the concept of time-delay might also work. Moreover, the particlelike DEFT-eigenstates are by construction invariant to a shift, e.g. a vibration, of the entire system in the chosen direction to first order.

The scattering matrix in such an imperfect system is calculated via the Fisher-Lee relations (2.2.32) and (2.2.33), where we use a code which is based on the modular recursive Green's function method. We will again assume an infinitely high potential for the walls of our potential well, as well as for the two added scatterers of circular shape (see Fig. 3.8). In this system, the transmission matrix is no longer unitary and thus we replace t^\dagger by t^{-1} in the definition (3.1.13) of the DEFT-operator. Since we want particlelike states that propagate through the system without getting back-reflected, we again utilize a singular value decomposition to pick out those t -eigenstates which feature a transmission close to unity. Similar to the representation of the time-delay operator in the subspace of fully transmitting states (see subsection 2.2.5), the DEFT-operator reads

$$d = -iv (u^\dagger t v)^{-1} u^\dagger u u^\dagger \frac{\partial t}{\partial \xi} v v^\dagger, \quad (3.1.24)$$

where ξ stands for a shift of the whole scattering region including the scatterers in the transverse direction. Please note, that the leads outside the scattering region do not get shifted. As shown in Fig. 3.8, eigenstates of this operator with a high $|\delta\kappa|$ are fully transmitted and furthermore feature a beam-like behavior like the eigenstates of the time-delay operator

$$q = -iv (u^\dagger t v)^{-1} u^\dagger u u^\dagger \frac{\partial t}{\partial \omega} v v^\dagger \quad (3.1.25)$$

shown in Fig. 3.9. Note, that we have used a system whose scattering region is $3d_{\text{fib}}$ long in order to reduce the numerical effort, where the length of each lead is d_{fib} . This demonstrates, that besides the concept of time-delay, the concept of DEFT also

applies to systems with scattering regions. Furthermore, our particlelike DEFT-eigenstates show a better spectral correlation in the range $-0.0025 < \Delta\omega/\omega_0 < 0.0025$ than the best correlated fiber modes (see Fig. 3.10), where the time-delay eigenstates are by construction invariant under a slight frequency shift and thus they feature a slightly broader correlation function compared to the DEFT-eigenstates as expected.

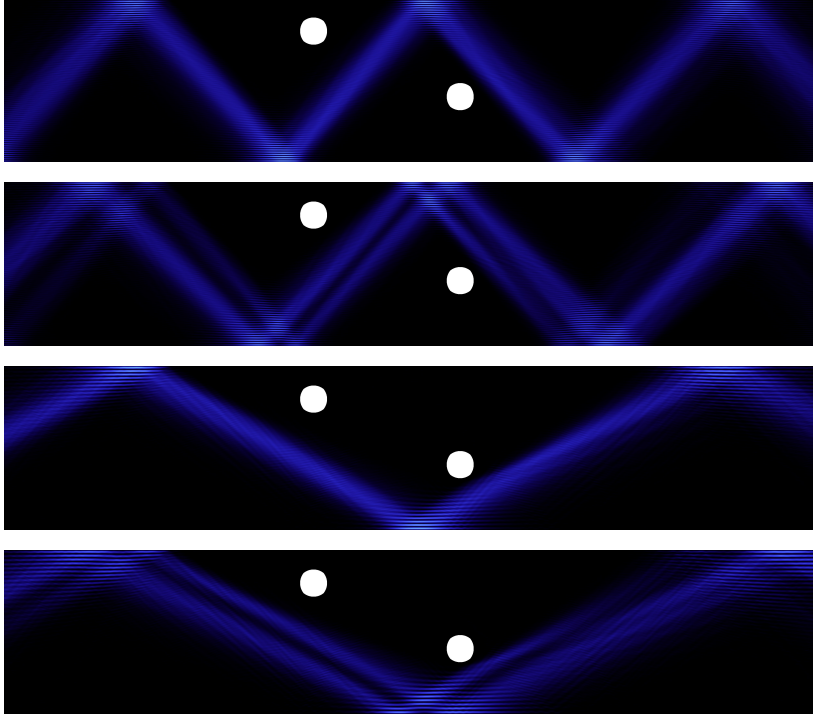


Figure 3.8: Propagation of four particlelike DEFT-eigenstates with a high $|\delta\kappa|$. These states have been obtained by shifting the whole scattering region including the scatterers (white circles) in the transverse direction. As in the perfect fiber without scatterers, we observe a quantization perpendicular to the direction of the beam propagation.

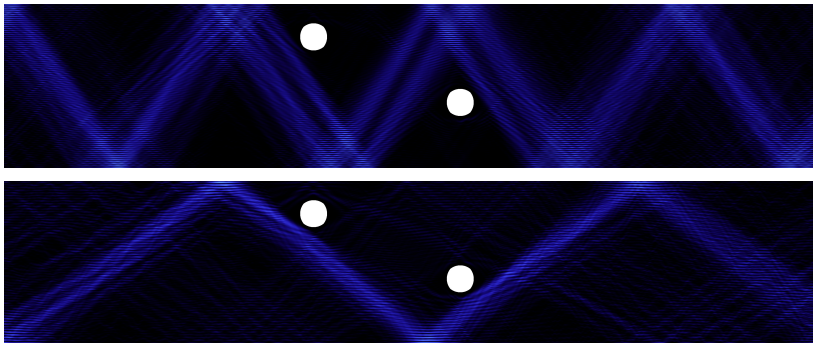


Figure 3.9: Propagation of two particlelike q -eigenstates with a high time-delay.

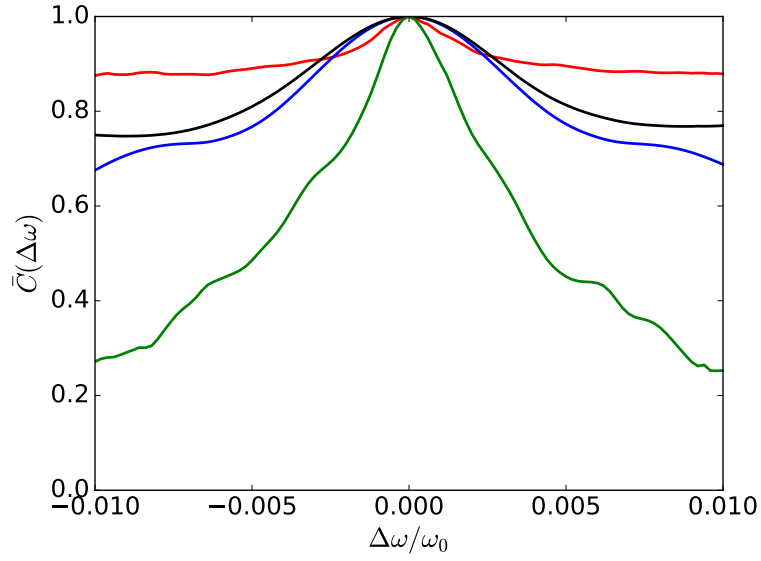


Figure 3.10: Mean correlation function of the ten best correlated fiber modes (red curve), the ten best d -eigenstates with the highest $|\delta\kappa|$ (blue curve), the ten q -eigenstates with the highest delay time (black curve) and thousand random states (green curve) in a scattering system. As expected, the time-delay eigenstates are slightly better correlated than our particlelike DEFT-eigenstates, where both of them feature a better correlation in the range $-0.0025 < \Delta\omega/\omega_0 < 0.0025$ than the best correlated fiber modes.

3.2 Wave Dynamics in a 3D D-Shaped Fiber

In this section we generalize the concepts found in the previous section to a three-dimensional, D-shaped geometry. Unlike in our two-dimensional toy model, we now also take into account the experimental limitations, i.e., we set $l_{\text{fib}} = 80r_{\text{fib}}$, $\gamma = 0.44$ or $\gamma = 1.05$ and use 400 modes calculated around a given angle which determines the transverse energy. This angle depends on the injection angle θ which we set to a value for which a wave undergoes approximately $n = 5$ reflections during the propagation. With the mean free path of trajectories $l_{\text{mfp}} = \pi r_{\text{fib}}/2$ the angle θ with respect to the optical axis can be estimated via

$$\theta = \arctan\left(\frac{nl_{\text{mfp}}}{l_{\text{fib}}}\right) \approx 5^\circ. \quad (3.2.1)$$

In a completely chaotic system, this number of bounces should be sufficient to reach a non-trivial regime, whereas in mixed systems states can undergo many more bounces due to the regular islands in the PSS. Moreover, with (2.2.18) as well as with (2.2.17), we find that $\tau_H/\tau_E \approx \mathcal{O}(10^1)$, and thus, the Ehrenfest time will keep its role as the limiting factor for propagation times (lengths). Bear in mind that the small spatial extent of our wave states due to the small system dimensions can cause a fairly large amount of spreading which is not included in the trajectory-based definition of the Ehrenfest time (2.1.12). However, considering this effect would yield even smaller Ehrenfest times resulting in a greater value of τ_H/τ_E .

3.2.1 Generalizing the Projection Procedure

Here, we will generalize the procedure in subsection 3.1.2, where we will explicitly demonstrate the difficulties that arise due to the increased dimensionality, which yields an additional degree of freedom. Together with our D-shaped cross section, this causes our transverse fiber modes not to be separable in x and y , in contrast to the eigenfunctions of Eq. (2.2.5), with an infinitely high rectangular potential, $\chi_{nm}(\vec{r}) = \chi_n(x)\chi_m(y)$. This non-separability causes our operators not to commute, i.e. $[x, y] \neq 0$ and $[k_x, k_y] \neq 0$, and hence we cannot find a common eigenbasis. Thus, doing two subsequent rotations into a k_x - and a k_y -subset destroys the effect of the first of the two transformations, and gives bad results. In a perfectly circular infinitely high potential well, however, the eigenstates of (2.2.5) are separable into r and φ components, which would enable us to do subsequent rotations into subsets of the radial momentum operator (k_r) and the angular momentum operator (L) eigenstates, but since we are interested in non-integrable phase spaces, we have to avoid doing more than one subspace rotation.

Being forced to use just one subspace rotation means that we have to find a single suitable operator to work with. One possible choice would be a momentum operator

in an arbitrary direction $k_\alpha = \cos(\alpha)k_x + \sin(\alpha)k_y$, but besides picking a certain subset at the input and output facet, we furthermore have to choose the angle α which determines the propagation direction of our states in the transverse plane. Another possible choice would be the operator $k_\varphi = L/r$, but the best results in terms of particlelike states have been achieved by rotating the transmission matrix into a (incomplete) subspace of eigenstates of the angular momentum operator

$$L = \vec{r} \times \vec{k} = xk_y - yk_x . \quad (3.2.2)$$

Like in subsection 2.2.5, this transformation is given by

$$t_L = \mathcal{L}_{\text{out}} t \mathcal{L}_{\text{in}} , \quad (3.2.3)$$

where $\mathcal{L}_{\text{in/out}}$ contains the subsets of L -eigenstates used for the rotation at the input and output facet. We construct the effective inverse of t_L again by using the mathematically “fully transmitting” singular vectors of t_L , which fulfill the choice of eigenvalues corresponding to the chosen subsets $\mathcal{L}_{\text{in/out}}$ at the fiber facets. Last, we project the frequency-derivative of the transmission matrix onto this subspace of singular vectors and get

$$q_L = -iv (u^\dagger t v)^{-1} u^\dagger u u^\dagger \frac{\partial t}{\partial \omega} v v^\dagger . \quad (3.2.4)$$

However, we have to make a more severe restriction than $L > 0$ at the input and output facet in order to get reasonable results. For our two-dimensional toy model, we have used a subset of k_y -eigenstates whose eigenvalues are conserved up to a sign. Considering our three-dimensional fiber now, we have emphasized in section 2.1.1 that the reason for the chaoticity of the D-shaped cross section lies in the fact that we have more degrees of freedom than conserved quantities. Since L and $|L|$ are only conserved in integrable geometries such as the full and the half circle, this could be responsible for the inferior performance (compare Figs. 3.11 and 3.4) of this method compared to its usage in our toy model.

In Fig. 3.11 the q_L -eigenstate with the highest time-delay is shown, where we have used a subset which corresponds to eigenvalues $L > 0.7L_{\text{max}}$ for the rotation at the input and output facet. This state behaves particlelike despite the underlying fully chaotic phase space, where it also exhibits a certain amount of refocusing caused by the partly convex shape of our cross section. This refocusing is visible in the last propagation snapshot in Fig. 3.11 in form of a “bent” intensity distribution which also causes a more elongated Husimi distribution at the boundary due to the larger number of momentum values contributing to that state.

Another disadvantage is that in mixed geometries with $1 < \gamma < 2$ most particlelike q_L -eigenstates are given by whispering gallery type states like the one shown in Fig. 3.12, which tends to conserve the angular momentum best. This, however, is a major drawback of this method since these q_L -eigenstates occupy the outer PSS regions corresponding to a larger ratio L/L_{max} , where it would be desirable to address the larger inner islands on which a wave state could fit on more easily.

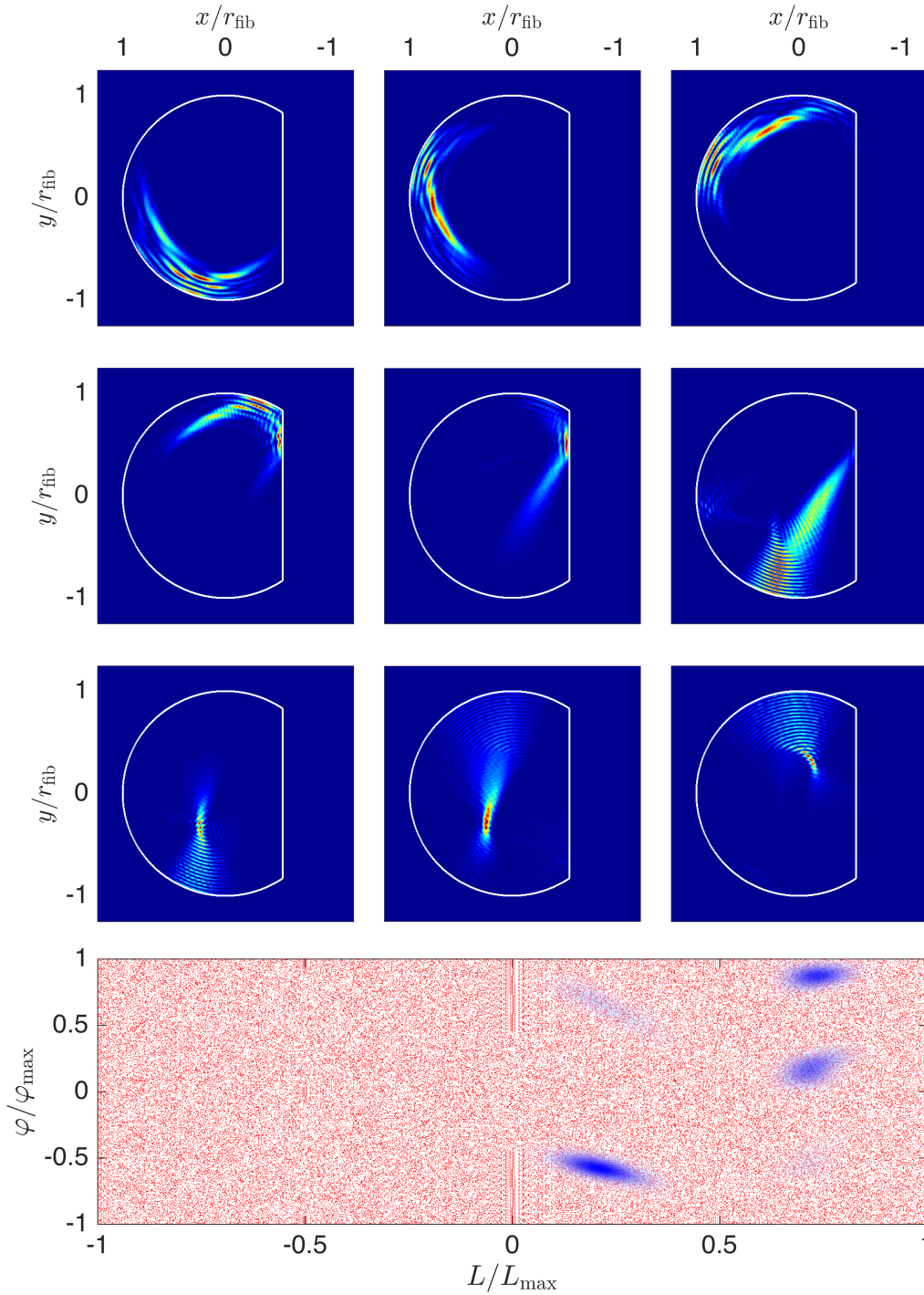


Figure 3.11: Top: Propagation snapshots for nine equidistant z -values (from the input facet at the top left to the output facet at the bottom right) of the q_L -eigenstate with the highest time-delay in a fiber with $\gamma = 0.44$ and $l_{\text{fib}} = 80r_{\text{fib}}$, where we have used the subset of states with $L > 0.7L_{\text{max}}$ at the input and output facet. In the last diagram one can see the effect of refocusing in form of a “bent” intensity distribution. Bottom: Corresponding mean Husimi distribution, where the underlying red dots represent the classical (fully chaotic) phase space. Here, the refocusing is visible in form of more elongated Husimi distributions at $\varphi/\varphi_{\text{max}} \approx \pm 0.5$.

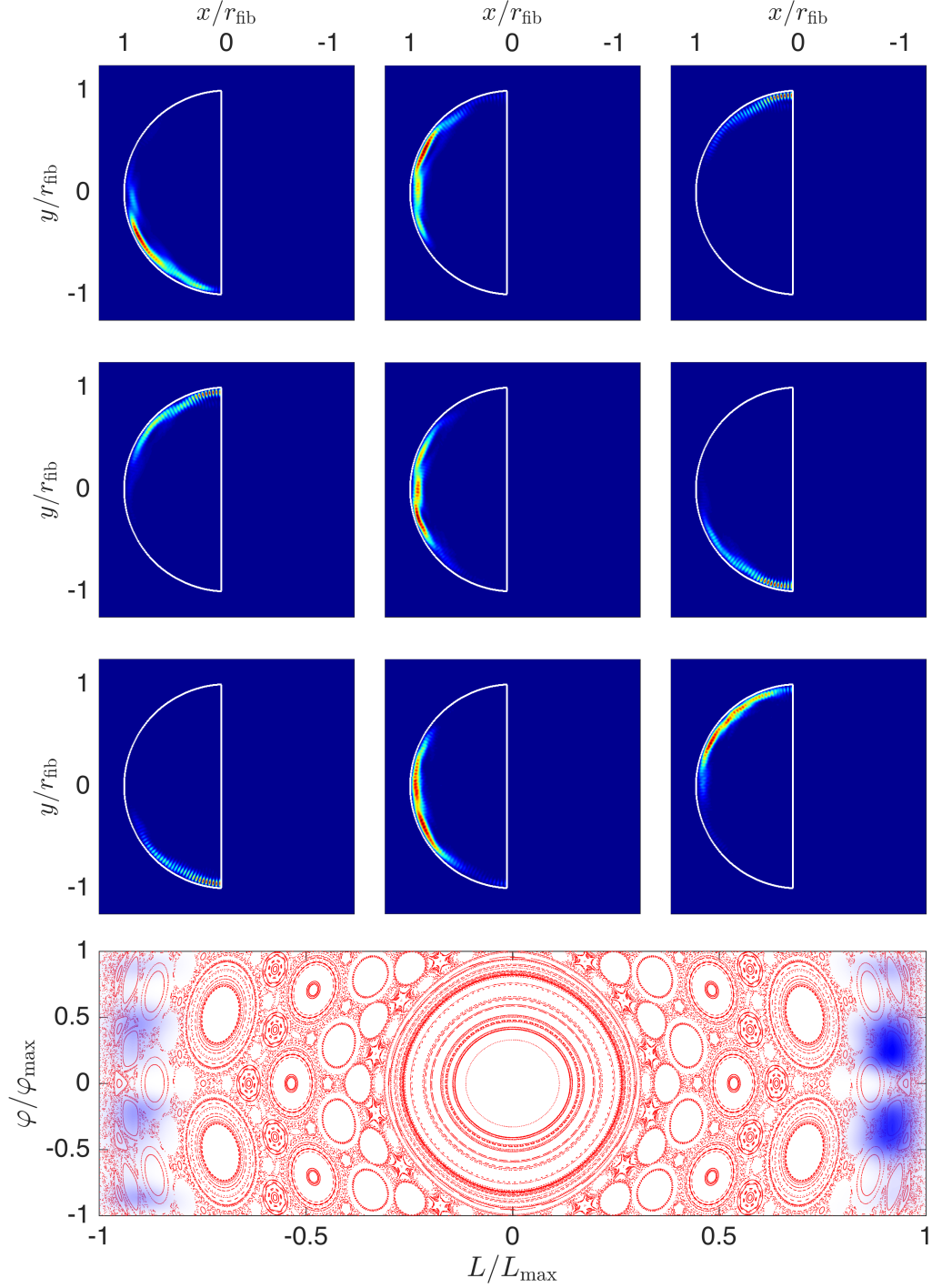


Figure 3.12: Top: Propagation snapshots for nine equidistant z -values (from the input facet at the top left to the output facet at the bottom right) of the q_L -eigenstate with the highest time-delay in a fiber with $\gamma = 1.05$ and $l_{\text{fib}} = 80r_{\text{fib}}$, where we have used the subset of states with $L > 0.7L_{\text{max}}$ at the input and output facet. Bottom: Corresponding mean Husimi distribution, where the underlying red dots represent the classical (mixed) phase space. This q_L -eigenstate is a whispering gallery type state which travels along the curved part of the boundary which causes its Husimi distributions to be located at large ratios L/L_{max} .

3.2.2 Finding Island States via the DEFT-Operator

In subsection 3.1.3, we have introduced the DEFT-operator as a generalization of the time-delay operator, where the arbitrary parameter of the derivative has been chosen to be the fiber position. In three dimensions, shifting the fiber in the transverse plane opens a lot of possibilities, but looking at the different shifting directions we found that we get the best particlelike DEFT-eigenstates, if we displace the fiber along its symmetry axis in the transverse plane, i.e., the x -axis (see Fig. 2.1), accordingly, we will denote the corresponding DEFT-operator as d_x . The reason for that lies in classical periodic orbits which are using the system's symmetry to return to their initial positions which yields a higher chance that the trajectory's transverse momentum at the output facet will be the negative of its initial value compared to other orbits which are not located on PSS islands. Regarding the DEFT-eigenstates, this results in a large $|\delta\kappa|$ and a particlelike behavior of the corresponding eigenstate whose Husimi distribution will be located on those classical PSS islands. Thus, shifting along the system's symmetry axis is generally beneficial for finding particlelike DEFT-eigenstates, whereas in our case of short fibers with $l_{\text{fib}} = 80r_{\text{fib}}$, we also get good results when shifting the fiber in an arbitrary direction. Also note that using the system's symmetry will lead to states that feature the same symmetry.

Shifting the fiber along the x -axis (see Fig. 2.1), we find states which correspond to classical periodic orbits amongst the best d_x -eigenstates, even in a completely chaotic system without any phase space structure (see Fig. 3.13 and Fig. 3.14). This is caused by the comparably short propagation lengths of $l_{\text{fib}} = 80r_{\text{fib}}$, where in the case of longer fibers these states disappear from the d_x -spectrum, since their momentum difference tends to zero due to the chaoticity of the system.

In a system with a classically mixed phase space, the situation changes since the phase space partly consists of stable islands. Once a state is placed on such islands, it can just escape via dynamic tunneling which is exponentially suppressed, i.e., the tunnel probability is proportional to $1 - \exp(-\zeta z)$ with a certain tunneling rate ζ [27]. The latter can be written as $\zeta \propto \exp(-C\mathcal{A})$, where $\mathcal{A} = \mathcal{A}(k_0)$ is the area of a phase space island and $C > 0$ is some system-dependent constant. Note that we have set $\hbar = 1$ in the expression for ζ in [27] due to the treatment of classical waves. Since $\mathcal{A}(k_0)$ is huge compared to 1 even in our treated fiber system, we do not expect to see any effects of dynamic tunneling. Thus, for such short propagation lengths a state is trapped on those islands, which ensures a well-defined momentum difference between the input and output facet. Again, looking at the d_x -eigenstates with the highest $|\delta\kappa|$, we find states that occupy phase space islands and accordingly "survive" many more reflections as compared to their counterparts in completely chaotic systems. In Figs. 3.15-3.17 three of those particlelike d_x -eigenstates which correspond to classical, periodic orbits are shown. Since the central island is large compared to the other ones, the spectrum of d_x contains a lot of states similar to

the one in Fig. 3.15, which just differ in form of a quantization in the direction perpendicular to the propagation direction. We already observed this quantization in our two-dimensional toy model (see Fig. 3.5a and 3.5b). Interestingly, we get eigenstates like the one shown in Fig. 3.16 together with a similar one which is located at the outer region, i.e. at larger ratios L/L_{\max} , of these four PSS islands, but we have not observed a state whose Husimi distributions are located directly in the centers of these islands. The reason for this could be the so called *Goos-Hänchen effect*, where linearly polarized light undergoes a small lateral shift when totally internally reflected, where the amount of lateral displacement depends on the reflection angle. Since this effect is a pure wave phenomenon, it is not accounted for in the calculation of the classical phase space which could explain the observed discrepancy.

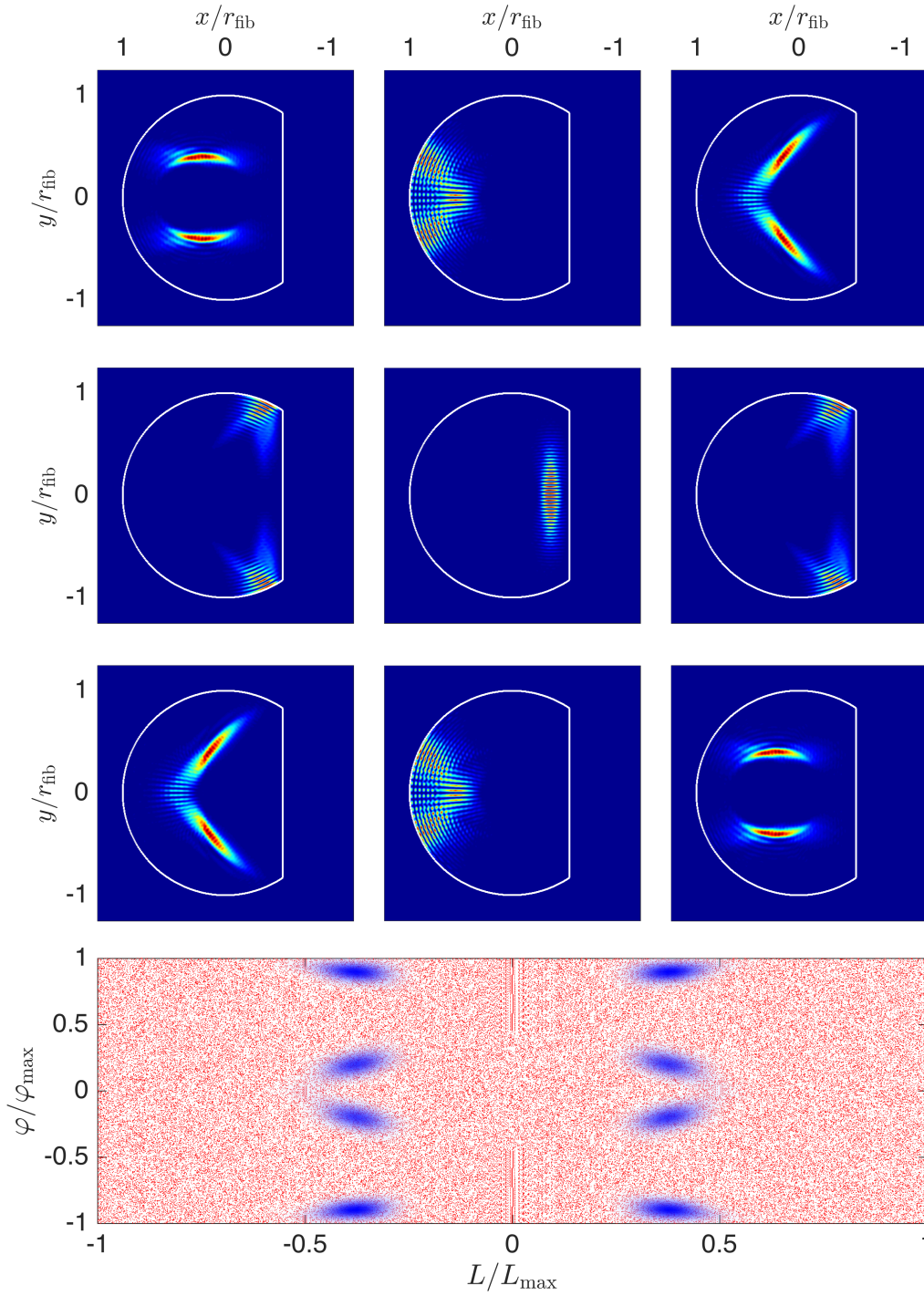


Figure 3.13: Top: Propagation snapshots for nine equidistant z -values (from the input facet at the top left to the output facet at the bottom right) of a d_x -eigenstate with a high $|\delta\kappa|$ in a fiber with $\gamma = 0.44$ and $l_{\text{fib}} = 80r_{\text{fib}}$. Bottom: Corresponding mean Husimi distribution, where the underlying red dots represent the classical (fully chaotic) phase space. Despite the absence of phase space islands, this state follows a classical, unstable, periodic orbit, i.e. it is a scar, which results in localized Husimi distributions.

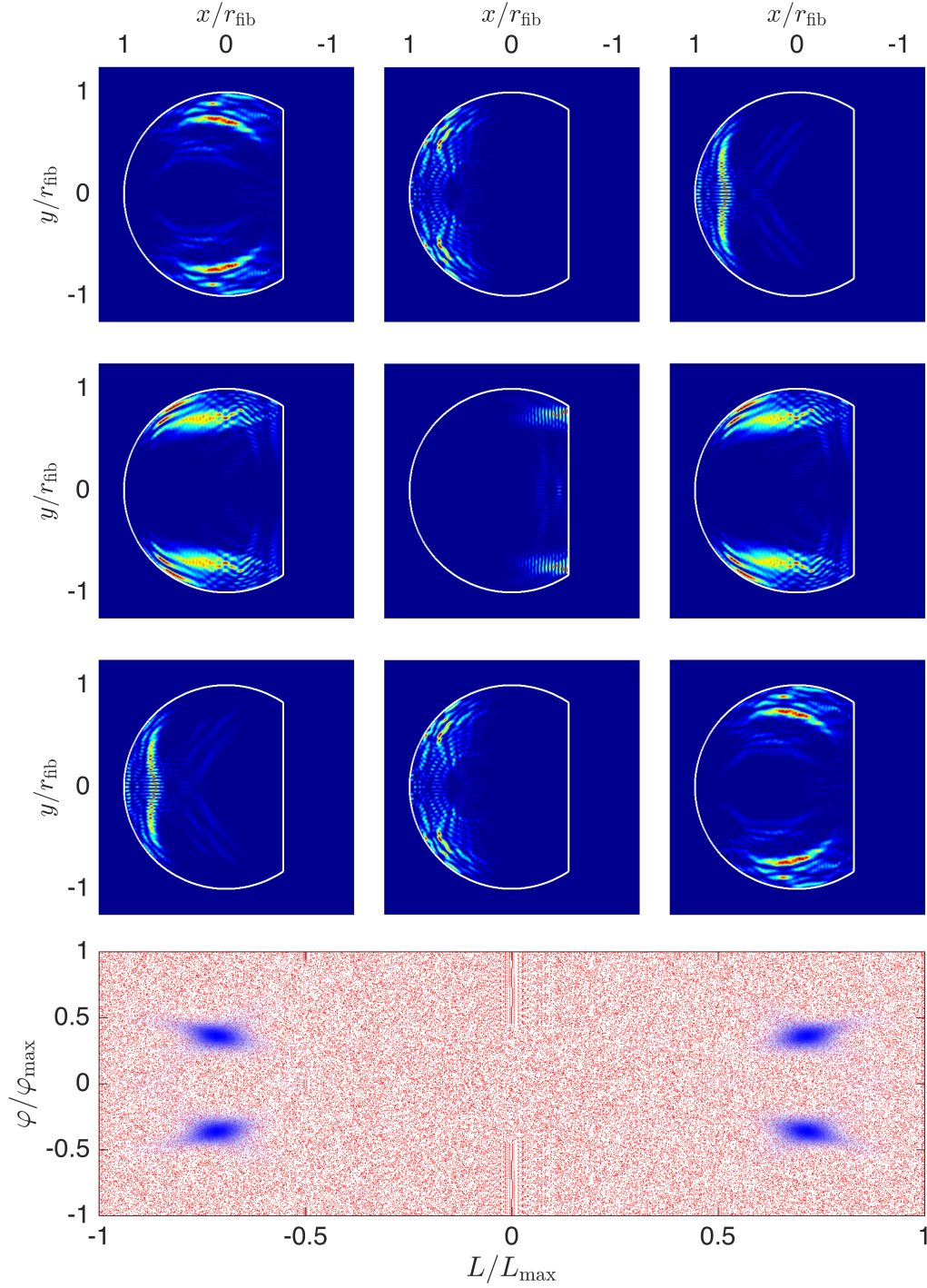


Figure 3.14: Top: Propagation snapshots for nine equidistant z -values (from the input facet at the top left to the output facet at the bottom right) of another d_x -eigenstate with a high $|\delta\kappa|$ in a fiber with $\gamma = 0.44$ and $l_{\text{fib}} = 80r_{\text{fib}}$. Bottom: Corresponding mean Husimi distribution, where the underlying red dots represent the classical (fully chaotic) phase space. This state is also a scar, i.e. it also follows a classical, unstable, periodic orbit, which again results in localized Husimi distributions.

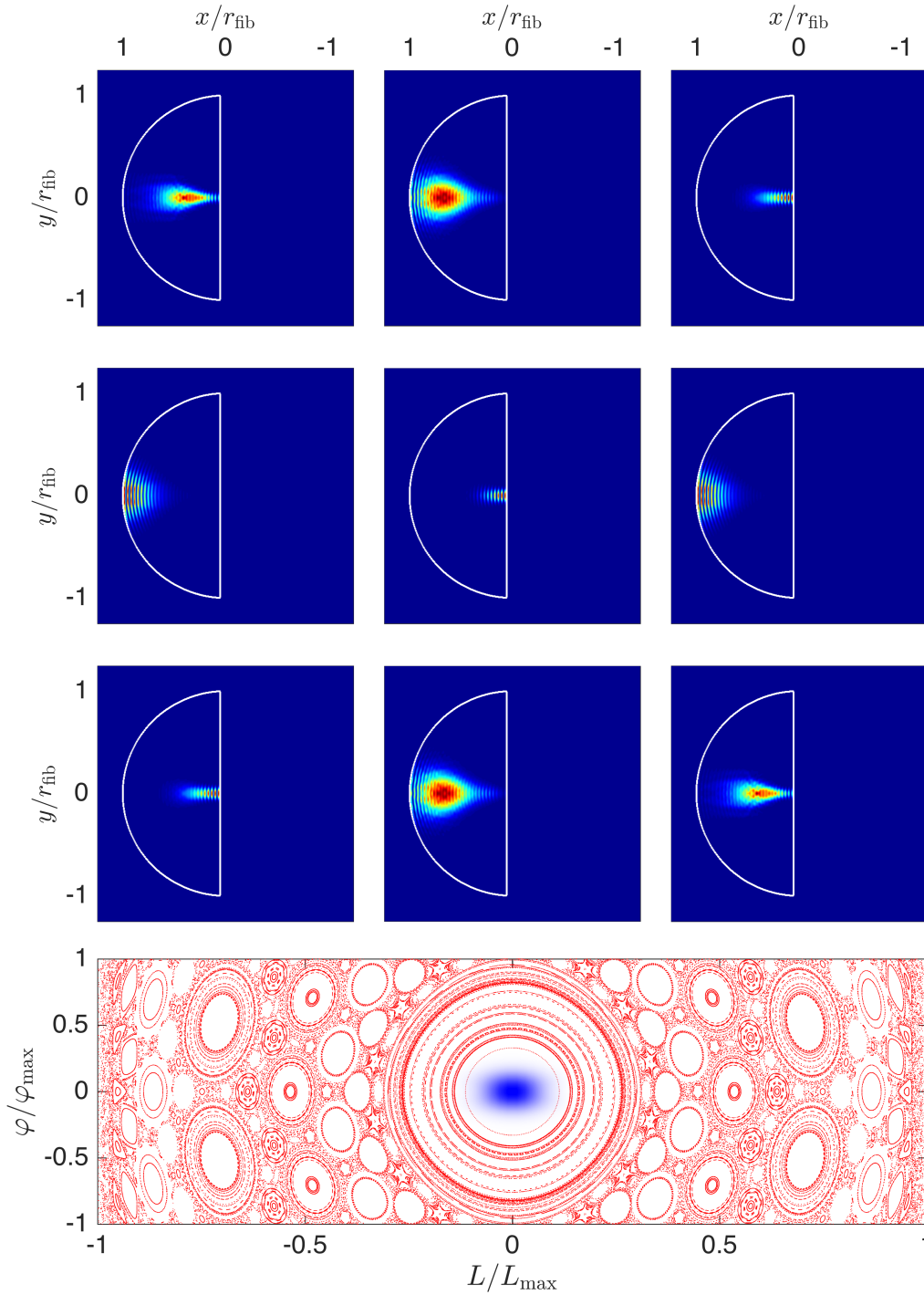


Figure 3.15: Top: Propagation snapshots for nine equidistant z -values (from the input facet at the top left to the output facet at the bottom right) of a d_x -eigenstate with a high $|\delta\kappa|$ in a fiber with $\gamma = 1.05$ and $l_{\text{fib}} = 80r_{\text{fib}}$. Bottom: Corresponding mean Husimi distribution, where the underlying red dots represent the classical (mixed) phase space. This state corresponds to the two-bounce orbit in Fig. 2.2 indicated by the red line and due to its form it has no angular momentum when it hits the curved part of the boundary at $y = 0$ and $x = r_{\text{fib}}$ which yields a mean Husimi distribution localized at the central PSS island.

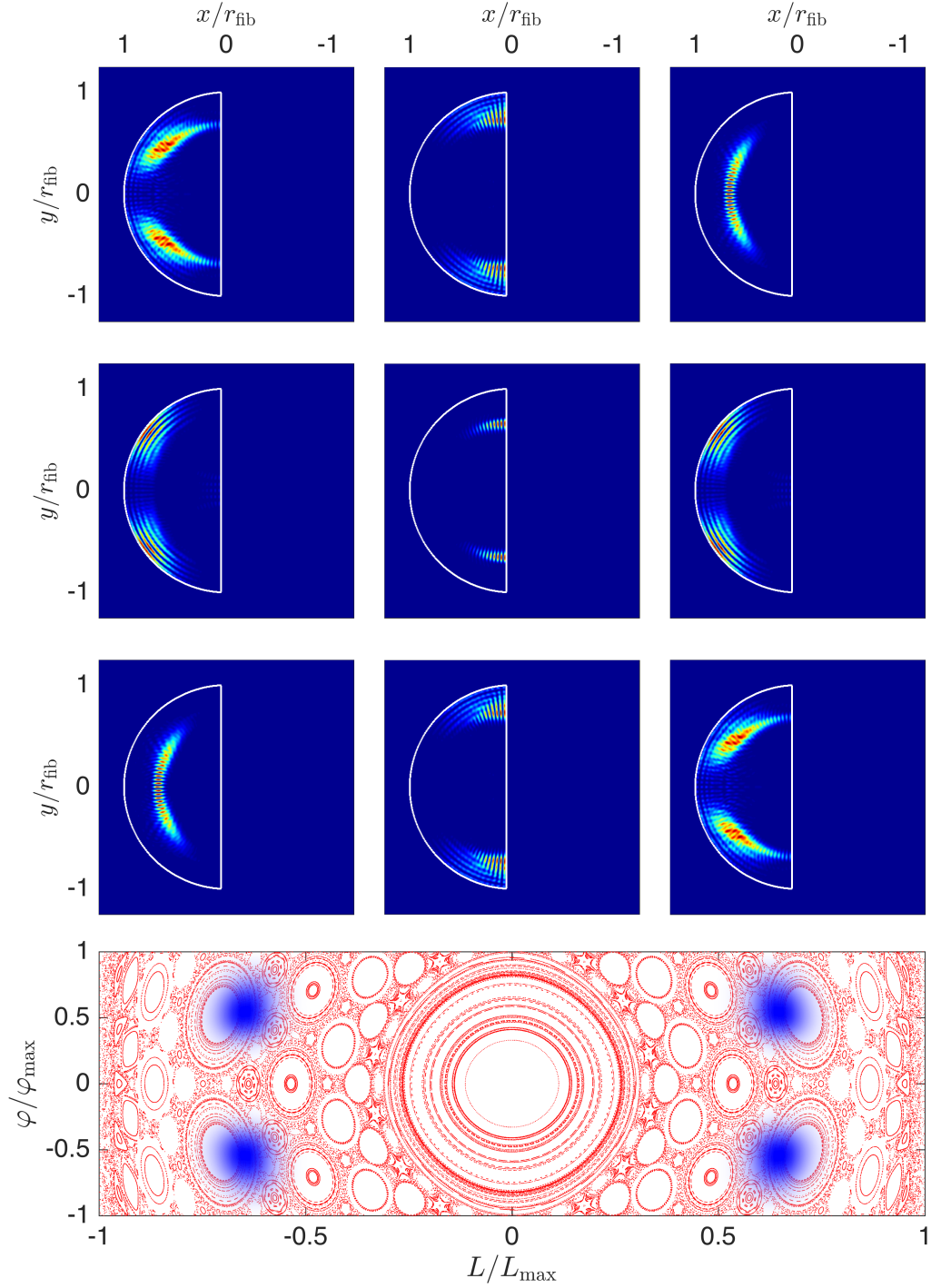


Figure 3.16: Top: Propagation snapshots for nine equidistant z -values (from the input facet at the top left to the output facet at the bottom right) of another d_x -eigenstate with a high $|\delta\kappa|$ in a fiber with $\gamma = 1.05$ and $l_{\text{fib}} = 80r_{\text{fib}}$. Bottom: Corresponding mean Husimi distribution, where the underlying red dots represent the classical (mixed) phase space. This state corresponds to the periodic orbit in Fig. 2.2 indicated by the blue line which yields a mean Husimi distribution localized at the second largest PSS islands.

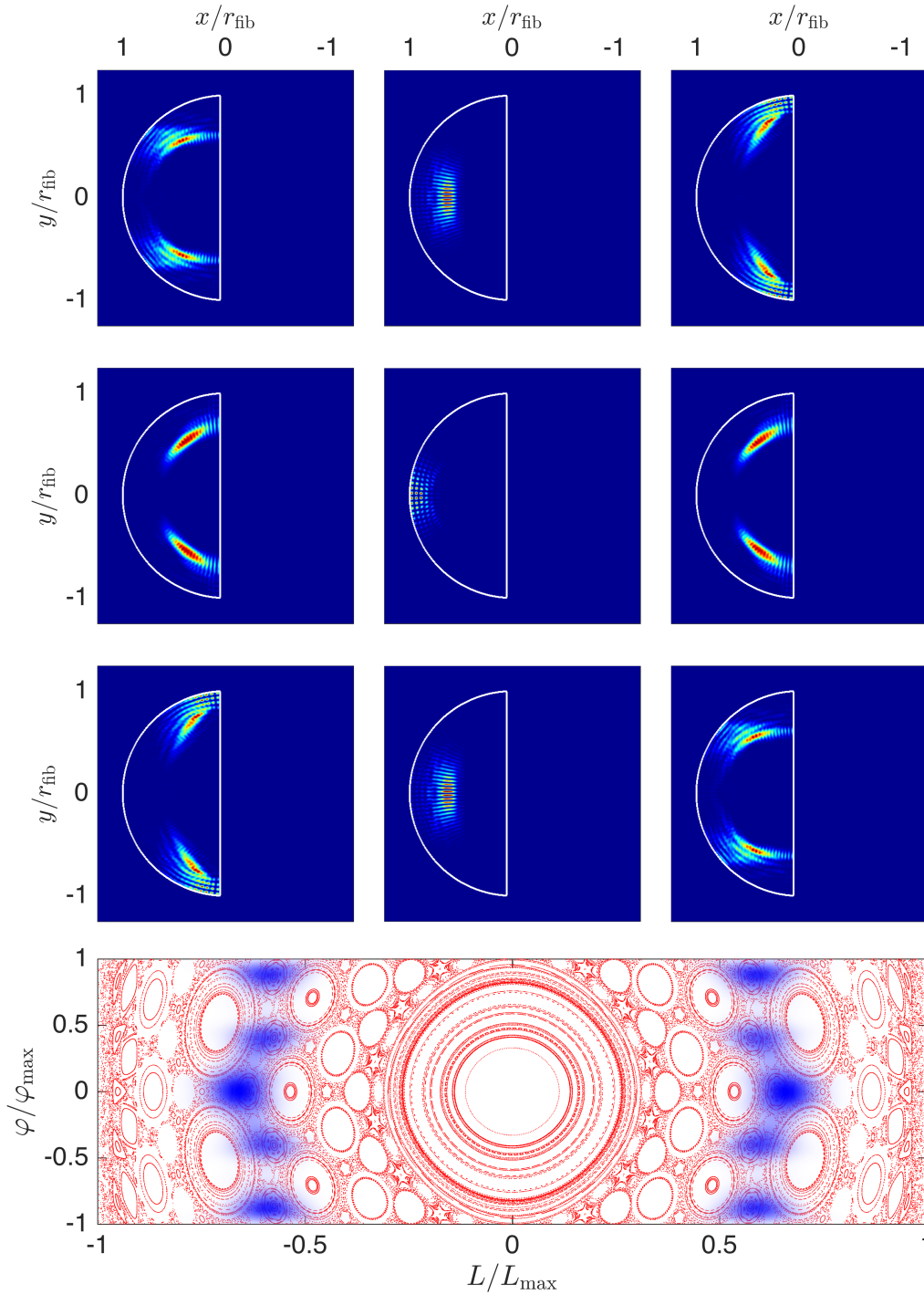


Figure 3.17: Top: Propagation snapshots for nine equidistant z -values (from the input facet at the top left to the output facet at the bottom right) of another d_x -eigenstate with a high $|\delta\kappa|$ in a fiber with $\gamma = 1.05$ and $l_{\text{fib}} = 80r_{\text{fib}}$. Bottom: Corresponding mean Husimi distribution, where the underlying red dots represent the classical (mixed) phase space. Like in the previous two Figures, also this state corresponds to a periodic orbit which again yields a mean Husimi distribution localized at some smaller PSS islands.

Again, we also look at the spectral correlation of the particlelike d_x -eigenstates which is calculated via (3.1.23). In the completely chaotic fiber with $\gamma = 0.44$, as well as in the mixed case $\gamma = 1.05$, the ten best d_x -eigenstates, i.e. with the highest $|\delta\kappa|$, show a broader spectral correlation than the average of thousand random states, where the q_L -eigenstates are again better correlated than the DEFT-eigenstates since they are by construction invariant under a ω -shift to first order. The modes show an infinitely broad correlation as already mentioned in chapter 3.1.3. Also note the faster decrease of the correlation function for a fiber with $\gamma = 1.05$. Since the area of the cross section of this system is smaller compared to the one with $\gamma = 0.44$, it has a larger energy-level spacing, which causes a given state to decorrelate faster for a slight frequency change. However, comparing Fig. 3.7 and Fig. 3.18, we observe a much more pronounced difference in the correlation between the DEFT-eigenstates and random states in the two-dimensional case, whereas the underlying reason for the less pronounced difference in three dimensions has not yet been found.

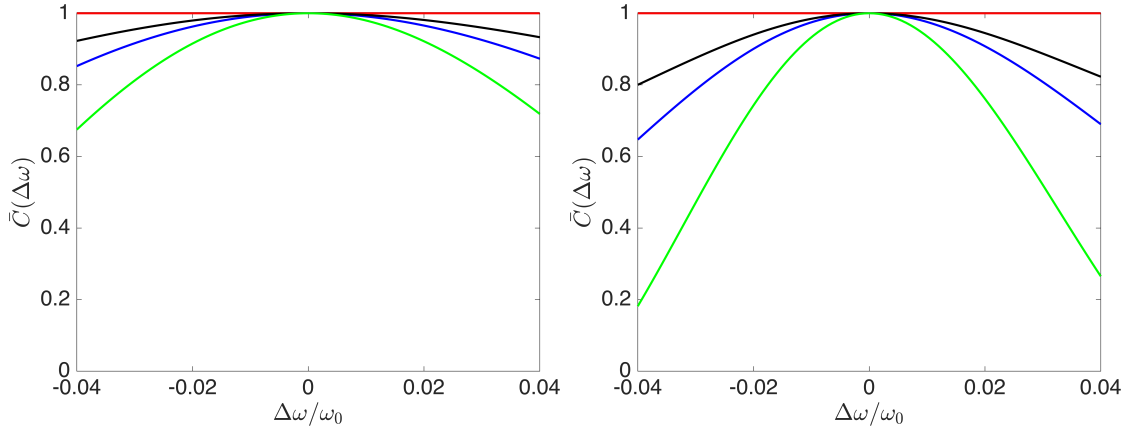


Figure 3.18: Mean correlation function of all fiber modes (red curve), the ten best d_x -eigenstates with the highest $|\delta\kappa|$ (blue curve), the ten q_L -eigenstates with the highest time-delay fulfilling the restriction $L > 0.5L_{\max}$ in the chaotic fiber or $L > 0.7L_{\max}$ in the mixed fiber at the input and output facet, and thousand random states (green curve) for a system with $\gamma = 0.44$ (left) and $\gamma = 1.05$ (right). Here one can see, that the DEFT-eigenstates feature a broader correlation function compared to the random states, whereas the time-delay eigenstates show an even stronger spectral correlation due to their ω -invariance to first order.

3.3 Classical Dynamics in a 3D D-Shaped Fiber

In this section we, investigate the behavior of trajectory bundles in the fiber system discussed in section 3.2 in order to make a comparison to the found DEFT-eigenstates and to see, if this approach allows predictions of the dynamics of wave states. Since we are using Gaussian shaped bundles we have to choose a reasonable standard deviation in order to make it comparable to the found DEFT-eigenstates. The initial standard deviation of the states in Fig. 3.13 (here we just use one of the two branches) and Fig. 3.15 is $\sqrt{\sigma_s^2 + \sigma_l^2} \approx 15 \mu\text{m}$ which is quite sizable as compared to the system's radius $r_{\text{fib}} = 62.5 \mu\text{m}$.

To make the trajectory simulations more comparable to the wave states we look at the standard deviations of these DEFT-eigenstates along their principle axes and pick the smaller one such that our Gaussian bundles do not exceed the extent of the wave states (see Fig. 3.19). This yields values of $\sigma_s \approx 5 - 8 \mu\text{m}$, where we choose the lower value, i.e. $\sigma_0 = 5 \mu\text{m}$, in order to ensure that our bundles are smaller than each of our wave states.

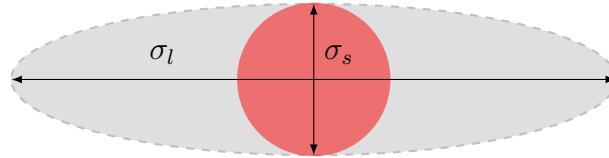


Figure 3.19: Sketch of the approximate shape of a particlelike DEFT-eigenstate or one of its branches (gray ellipse) with its standard deviations σ_l/σ_s along its longer/shorter principal axis indicated. Since the standard deviation $\sqrt{\sigma_l^2 + \sigma_s^2} \approx 15 \mu\text{m}$ is quite sizable as compared to the system radius, we just use $\sigma_0 = \sigma_s \approx 5 \mu\text{m}$ for our Gaussian (red circle).

For the search of particlelike trajectory bundles, we use a discrete grid in the xy -plane for the positions from which the trajectories are launched combined with varying the angle φ in finite steps for every gridpoint and let the bundles propagate while monitoring their spread in terms of calculating their standard deviation for every propagation step. Depending on the value of $\gamma = r_{\text{cut}}/r_{\text{fib}}$, the number of injected trajectory bundles ranges from $2 \cdot 10^3$ to $4 \cdot 10^3$. Next, we have to specify a criterion for states to be counted as particlelike, where we have chosen this criterion to be

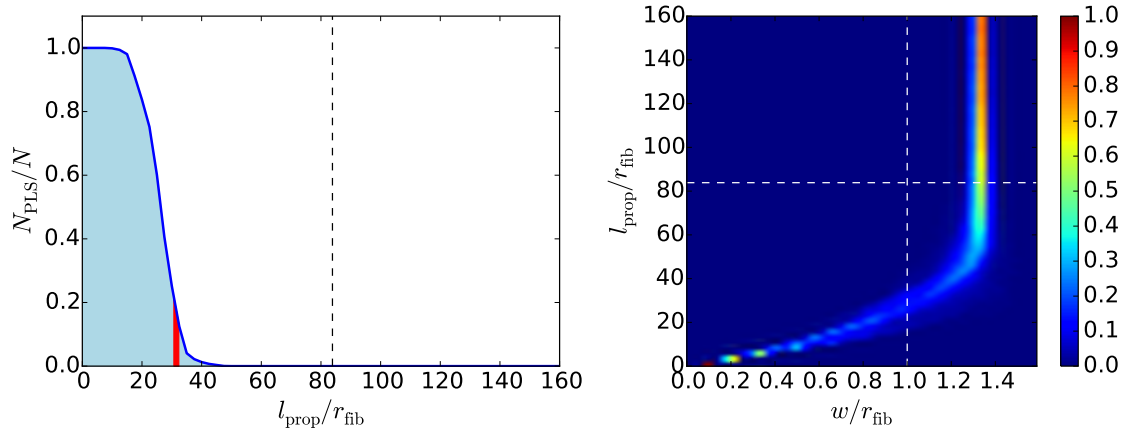
$$w = 2\sigma < r_{\text{fib}} . \quad (3.3.1)$$

Applying this to a system with $\gamma = 0.44$ yields the result shown in Fig. 3.20a, where one can see that the value of the mean Ehrenfest length does not serve as a good approximation for the limitation of propagation lengths. This is mainly caused by spreading which does not enter the definition (2.1.12) of the Ehrenfest

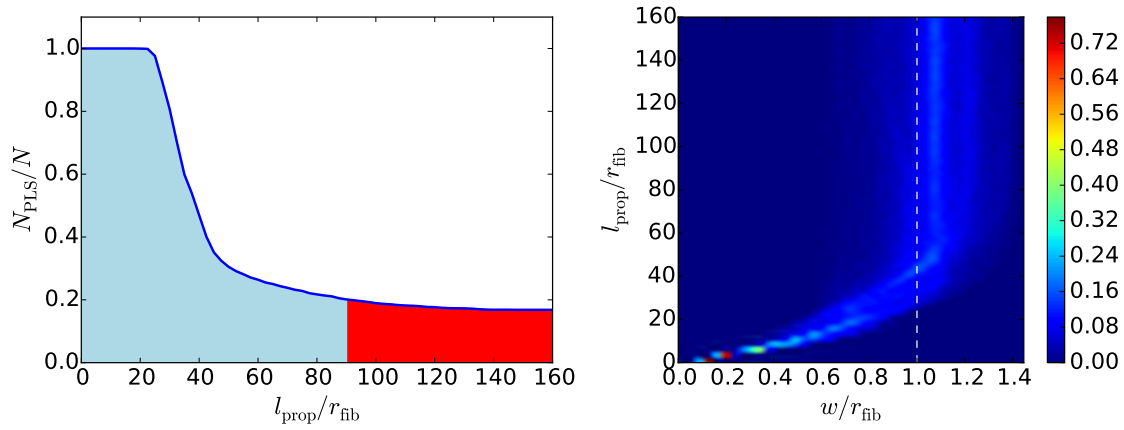
time. Together with the chaoticity of the system, we observe a rapid decrease in the number of particlelike bundles, as expected. In the right diagram of Fig. 3.20a, we can see the evolution of the bundle spreads dependent on the propagation length: At the input facet ($l_{\text{prop}} = 0$) all bundles have the same initial width, where they rapidly spread out for short propagation length mainly due to spreading and reach the saturated regime caused by the boundedness of the system. Looking at some of the bundles which lie in the red region in the left diagram of Fig. 3.20a, we notice that due to the shallow injection angle of $\theta = 5^\circ$ they undergo just two bounces on average, where for $l_{\text{fib}} = 80r_{\text{fib}}$ none of these states have survived.

Next, we examine the case of a fiber with $\gamma = 1.05$ in which the phase space islands could help the trajectory bundles to stay collimated. Comparing Fig. 3.20a to Fig. 3.20b in which the number of particlelike bundles and the evolution of bundle-spreads are shown, we notice that the former decays much more slowly due to the mixed phase space structure. Looking at the most collimated states for $l_{\text{fib}} = 80r_{\text{fib}}$, we find that they are exclusively states that occupy the central island, where two of these states are shown in Fig. 3.21. Due to the rapid spreading the bundles only fit on this island, which is the largest.

Comparing these results to the found particlelike DEFT-eigenstates in subsection 3.2.2, we find that for such small geometries the trajectory bundle approach is not a valid tool for predicting the behavior of waves. This is mainly caused by the lack of interference which gets more and more important the smaller a bundle is compared to the wavelength of light. In other words, interference will not play such an important role in larger geometries like the experimentally available rod-systems treated in the following section in which case the trajectory bundle approach will serve as a good approximation for describing the dynamics of wave states.

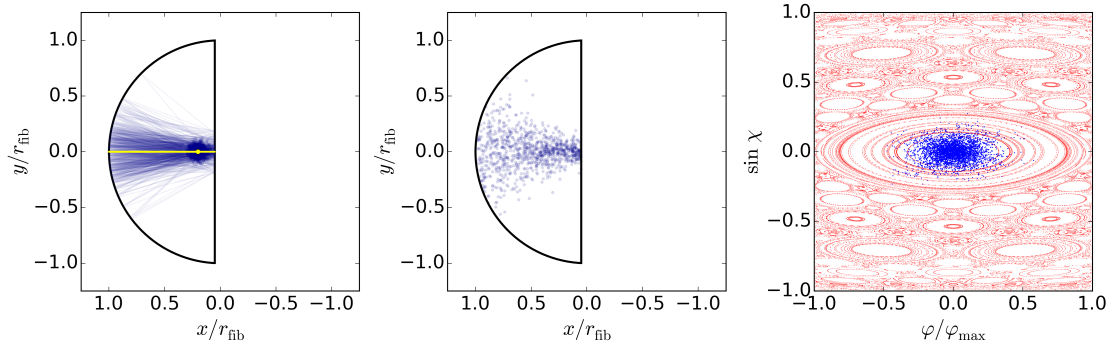


(a) Fiber system with the ratio of fiber cut over fiber radius $\gamma = r_{\text{cut}}/r_{\text{fib}} = 0.44$: In the left diagram one can see the fast decrease of number of particlelike bundles, where the distribution of spreads in the right diagram also shows a fast transition to the saturated regime caused by the boundedness of the system.

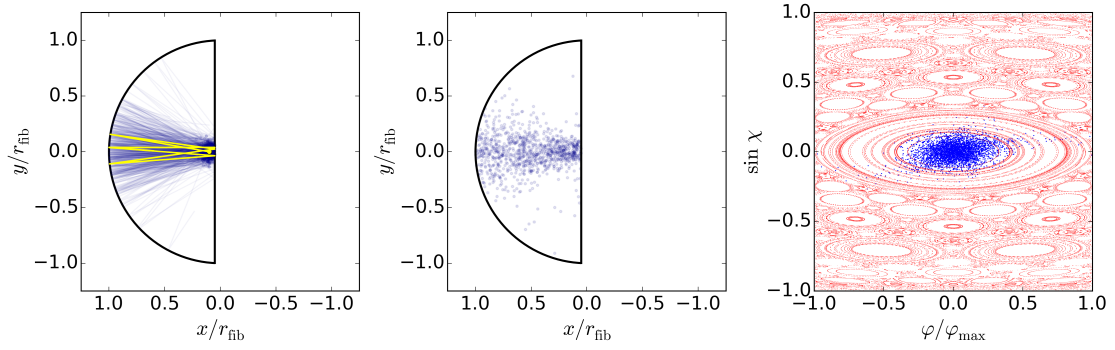


(b) Fiber system with the ratio of fiber cut over fiber radius $\gamma = r_{\text{cut}}/r_{\text{fib}} = 1.05$: In the left diagram one can see a slower decrease of the number of particlelike bundles compared to the chaotic system, where the distribution of spreads in the right diagram also shows a fast transition to the saturated regime. However, bundles occupying the central PSS island (see Fig. 3.21) will stay more or less bundled together for longer propagation lengths due to the trapping on that island which causes a broader spread distribution compared to the fully chaotic case.

Figure 3.20: Left: Number of particlelike bundles N_{PLS} over the number of injected bundles N in a fiber system with $r_{\text{fib}} = 62.5 \mu\text{m}$ dependent on the propagation length l_{prop} , where the red area marks the region in which 10-20% of bundles are particlelike and the dashed vertical line denotes the Ehrenfest length. Right: Histogram plot of spreads dependent on the propagation length. Here the vertical dashed line marks the particlelike-criterion, the horizontal dashed line denotes the Ehrenfest length and the colormap stands for the percentage of spreads in a certain bin.



(a) Best particlelike bundle in the given fiber system which occupies the central PSS island. Note, that even if this bundle is counted as particlelike due to our loosened criterion, its distribution of trajectories at the output facet is fairly delocalized.



(b) Another particlelike bundle in the given fiber system which also occupies the central PSS island and thus follows a quasi-periodic orbit in position space.

Figure 3.21: Fiber with $\gamma = 1.05$ and $l_{\text{fib}} = 80r_{\text{fib}}$: The left diagram of each row shows the initial Gaussian and the propagation of a subpart of the bundle's trajectories, where the yellow line marks the Gaussian center trajectory. The center diagrams show the final distribution of trajectories at the output facet and the right diagrams show their PSS distribution over the whole propagation (blue) together with the entire PSS (red).

3.4 Classical Dynamics in a 3D D-Shaped Rod

Here we study classical trajectory bundle dynamics given a system which consists of a glass rod with of radius $r_{\text{fib}} = 2.5$ mm, and a length of $l_{\text{fib}} = 200$ mm $= 80r_{\text{fib}}$ in order to predict the behavior of waves in such a system. Scaling up the width of our Gaussian bundles used in the preceding section by the same factor as the system dimension yields $w_0 = 200$ μm , where we keep the angle to the fiber axis the same, i.e., $\theta = 5^\circ$.

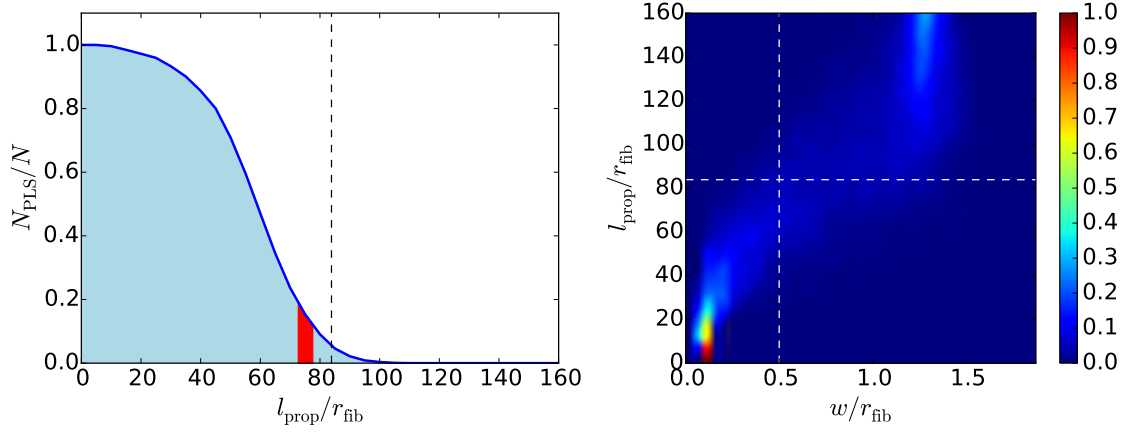
Like in the previous section, we track the standard deviations of trajectory bundles launched at different positions in the xy -plane, where we also vary the angle φ in discrete steps at each initial position. Due to the smaller amount of spreading we use the particlelike criterion

$$w = 2\sigma < \frac{r_{\text{fib}}}{2} , \quad (3.4.1)$$

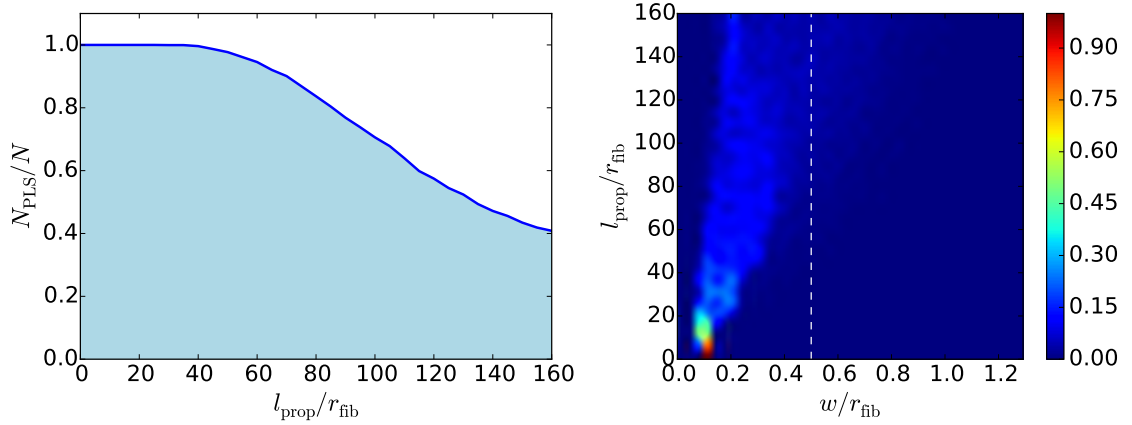
which again has to be fulfilled for all previous propagation steps in order for a state to be counted as particlelike at a given propagation length.

Applying this to a rod with $\gamma = 0.44$ yields the diagrams in Fig. 3.22a. In the left diagram one can see that for the given parameters the non-trivial regime (red) in which 10-20% of bundles are counted as particlelike lies around $l_{\text{prop}} \approx l_{\text{fib}}$, where the mean Ehrenfest length coincides nicely with our results in the sense that almost no particlelike bundles are left at this propagation length. Furthermore, calculating the Heisenberg time via (2.2.18) and (2.2.17) we find a greater value of $\tau_H/\tau_E \approx \mathcal{O}(10^3)$ due to the larger system dimensions, and thus the Ehrenfest time will remain our limiting factor. Looking at the evolution of bundle-spreads in the right diagram of Fig. 3.22a, we observe a much slower reach of the saturated regime compared to the fiber system discussed in the preceding section which is mainly caused by the smaller amount of spreading.

Moving on to the rod with $\gamma = 1.05$, we can see in Fig. 3.22b, that the spreading happens much more slowly in comparison to a rod with $\gamma = 0.44$ due to the presence of phase space islands. Moreover, it is worth noting that in this system, the mean Lyapunov exponent of the whole system has lost its meaning since the spreading of bundles launched on those islands happens in a linear way in contrast to the exponential growth in the chaotic regions. In contrast to waves which can exhibit dynamic tunneling, trajectories, once placed on an island, cannot escape which causes a limitation of the maximal spread, which is determined by the size of the island. Thus, a lot of particlelike bundles survive up to $l_{\text{prop}} = l_{\text{fib}}$.



(a) Rod system with the ratio of fiber cut over fiber radius $\gamma = r_{\text{cut}}/r_{\text{fib}} = 0.44$: In the left diagram one can see that the decrease of the number of particlelike bundles happens much slower compared to the fiber system (see Fig. 3.20a) due to the small amount of spreading. Thus, the bundle spreading is mainly caused by the chaoticity of the system which yields a mean Ehrenfest length at which almost no particlelike bundles are left. The evolution of spreads in the right diagram shows a much more slowly and differently shaped transition to the saturated regime like the one in Fig. 3.20a.



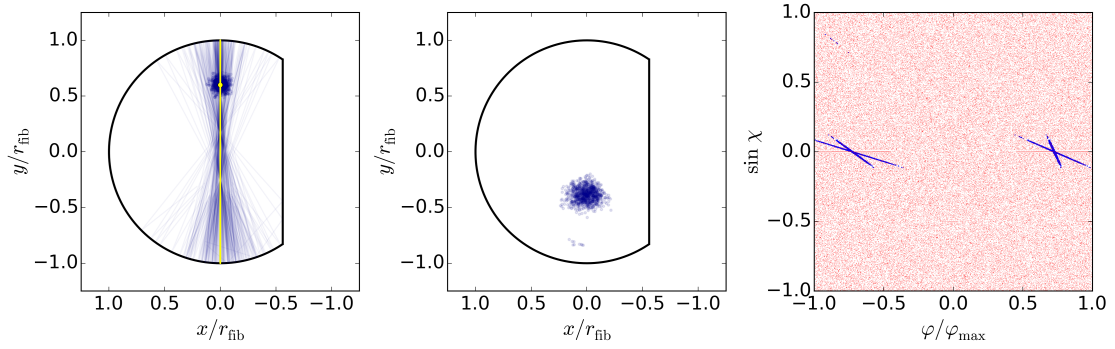
(b) Rod system with the ratio of fiber cut over fiber radius $\gamma = r_{\text{cut}}/r_{\text{fib}} = 1.05$: Due to the presence of PSS islands and the small amount of spreading the increase of the bundle-widths happens at a much slower rate compared to the chaotic case shown above. This can be seen in the left diagram in form of a large number of “surviving” particlelike bundles as well as in the slower growth of spreads visible in the right diagram.

Figure 3.22: Left: Number of particlelike bundles N_{PLS} over the number of injected bundles N in a rod system with $r_{\text{fib}} = 2.5$ mm dependent on the propagation length l_{prop} , where the red area marks the region in which 10-20% of bundles are particlelike and the dashed vertical line denotes the Ehrenfest length. Right: Histogram plot of spreads dependent on the propagation length. Here the vertical dashed line marks the particlelike-criterion, the horizontal dashed line denotes the Ehrenfest length and the colormap stands for the percentage of spreads in a certain bin.

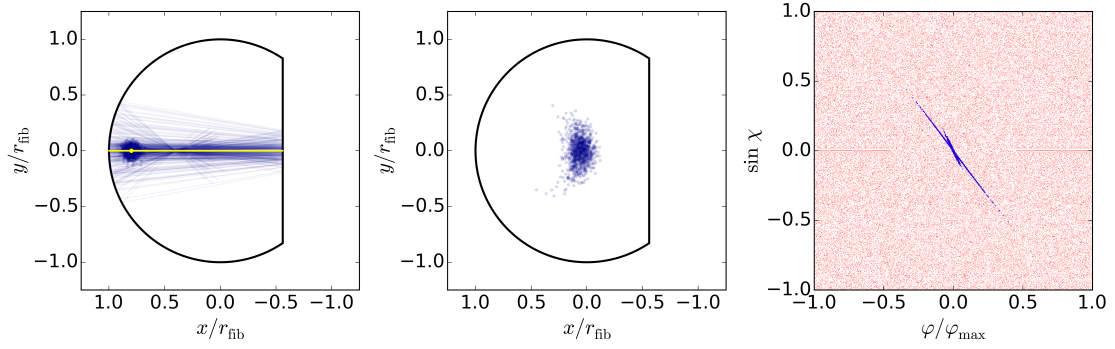
Of course, we are also interested in the shapes in coordinate space and the PSS distributions of our particlelike trajectory bundles for $l_{\text{fib}}/r_{\text{fib}} = 80$. In Fig. 3.23, some of the best states in a rod with $\gamma = 0.44$ are shown, which we can categorize into three types of orbits: diameter orbits which do not bounce off the cut, remnants of classically unstable periodic orbits which survive such short propagation lengths despite bouncing off the cut, and refocused orbits that use the convex and focusing geometry of the system.

By examination of the best particlelike bundles in a rod with $\gamma = 1.05$, we find that most of them occupy the central phase space island which contains lots of similar quasi-periodic orbits due to its large size. As shown in Fig. 3.24 we also find orbits which correspond to the second and third biggest island, where the smaller islands cannot be reached since the initial width of our Gaussian is too big. We also find particlelike bundles that partly occupy the chaotic sea, where their “survival” is caused by the short propagation length $l_{\text{fib}}/r_{\text{fib}} = 80$.

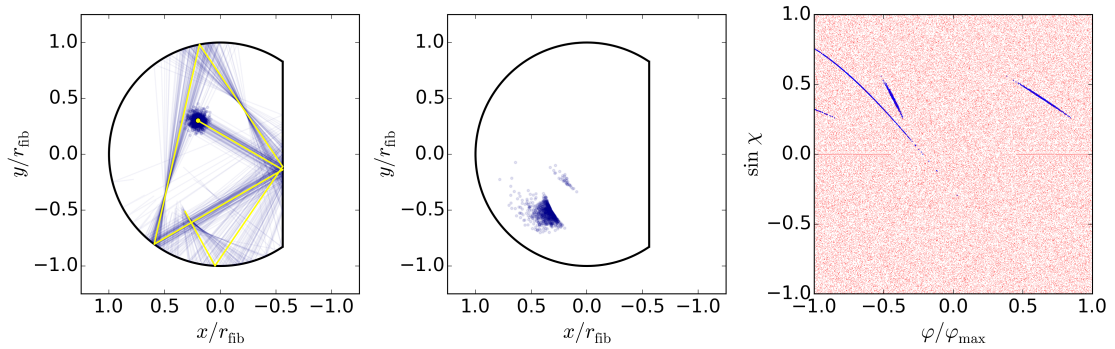
In contrast to the trajectory bundle simulations in fiber systems, the treatment of larger bundles in rod systems yields nice results due to the small amount of spreading which makes interference not so important for the survival of collimated states. In case of a chaotic rod, the fiber length $l_{\text{fib}} = 80r_{\text{fib}}$ lies in the non-trivial regime, where just a few particlelike trajectory bundles are left. In a mixed rod, however, approximately 80% of the bundles are counted as particlelike for $l_{\text{prop}} = l_{\text{fib}}$, where the regime, in which particlelike bundles are the minority, is reached for much longer lengths due to the presence of phase space islands. Even though the length $l_{\text{prop}} = l_{\text{fib}}$ seems to lie in a trivial regime in case of a mixed rod, the main goal is to place initial states on phase space islands, which has been achieved by launching approximately $2 \cdot 10^3$ bundles with different initial conditions into the fiber. This scanning of initial conditions can be avoided by the application of the concept of DEFT (see section 3.2.2), which is based on the measurement of the transmission matrices, where it is very likely that DEFT-eigenstates with the most well-defined momentum difference occupy phase space islands. Together with the good results obtained in this section, we are confident that we will find good agreement with the experimental measurements and that the realization of the DEFT-concept will also yield particlelike wave states in these rod systems.



(a) Example of a particlelike bundle whose trajectories do not bounce off the cut (diameter orbit) and hence they do not experience the chaoticity introduced by the cut.

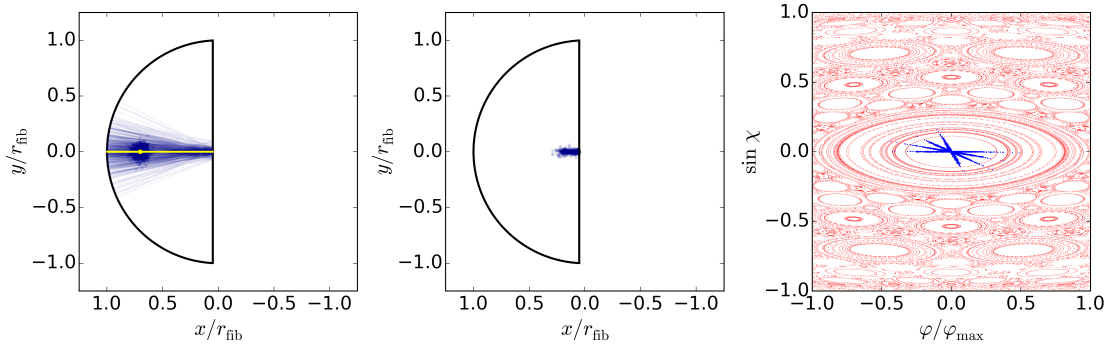


(b) Example of a particlelike bundle whose trajectories follow a classical, quasi-periodic orbit which is unstable due to the placement of the cut at $\gamma = 0.44$, whereas its counterpart in a system with $\gamma = 1.05$ is stable (see Fig. 3.24).

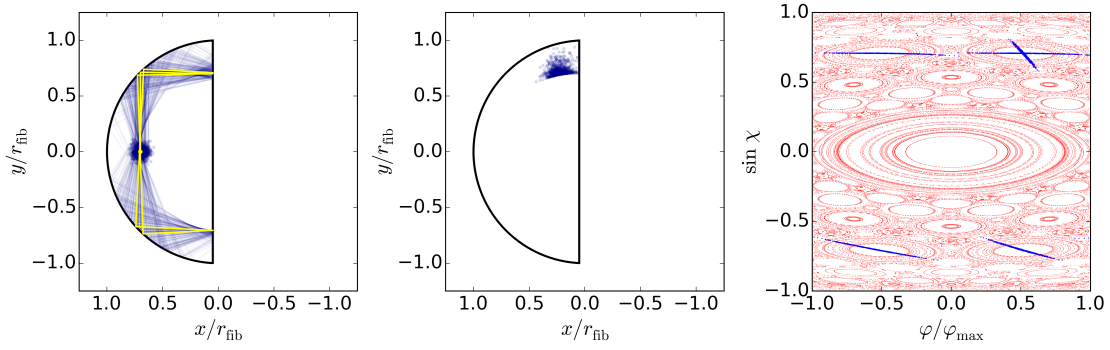


(c) Example of a particlelike bundle whose trajectories exhibit refocusing. This can be seen in the left diagram at the end of the yellow Gaussian center trajectory as well as in phase space in form of the longer blue streak.

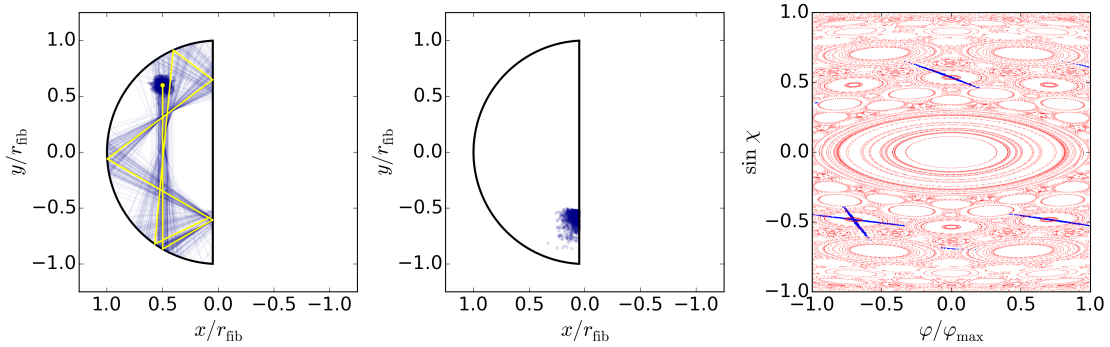
Figure 3.23: Rod with $\gamma = 0.44$ and $l_{\text{fib}} = 80r_{\text{fib}}$: The left diagram of each row shows the initial Gaussian and the propagation of a subpart of the bundle's trajectories, where the yellow line marks the Gaussian center trajectory. The center diagrams show the final distribution of trajectories at the output facet and the right diagrams show their PSS distribution over the whole propagation (blue) together with the entire PSS (red).



(a) Example of a particlelike bundle whose trajectories follow a classical, quasi-periodic two-bounce orbit which is similar to the found DEFT-eigenstate in the fiber system shown in Fig. 3.15.



(b) Example of a particlelike bundle whose trajectories follow a classical, quasi-periodic four-bounce orbit (see blue line in Fig. 2.2) which is similar to the found DEFT-eigenstate in the fiber system shown in Fig. 3.16.



(c) Example of a particlelike bundle whose trajectories follow a classical, quasi-periodic five-bounce orbit.

Figure 3.24: Rod with $\gamma = 0.44$ and $l_{\text{fib}} = 80r_{\text{fib}}$: The left diagram of each row shows the initial Gaussian and the propagation of a subpart of the bundle's trajectories, where the yellow line marks the Gaussian center trajectory. The center diagrams show the final distribution of trajectories at the output facet and the right diagrams show their PSS distribution over the whole propagation (blue) together with the entire PSS (red).

Chapter 4

Summary and Outlook

In this thesis, we have investigated the classical trajectory and wave dynamics in three-dimensional straight geometries with a D-shaped cross section without cladding, with the aim of finding particlelike states which are highly collimated beams. We have studied actual multi-mode fiber systems as well as rod systems, where the treatment of the latter was constrained to classical trajectory bundle simulations, since the full wave simulation of such systems is numerically not feasible. Dependent on the placement of the cut, which yields the D-shaped cross section, the system shows regular, completely chaotic or mixed classical dynamics, where we were mainly interested in the latter two cases, in which chaos can counteract the formation of particlelike states.

For simplicity we first considered the wave dynamics in a two-dimensional toy model of a multi-mode fiber, where our first approaches for finding particlelike states were based on the minimization of a non-linear functional, and the generalization of coherent states in harmonic oscillator potentials to potential wells. Due to their poor performance, we moved on to operator-based approaches, where projecting the time-delay operator onto a subspace of the transverse position operator yields good results. However, for certain subsets we observe the emergence of eigenstates with two branches rather than a single collimated beam, which are caused by a degeneracy in delay-times for different signs of the transverse momentum. Even better results have been achieved by using the subset of transverse momentum eigenstates with an eigenvalue less or greater than zero which lifts the mentioned degeneracy and gives exclusively eigenstates consisting of single branches. Apart from this method we have also generalized the Wigner-Smith time-delay operator to the DEFT-operator by replacing its derivative w.r.t. the frequency by the derivative w.r.t. an arbitrary continuous parameter. The latter has been chosen to be the spatial position of the entire fiber, where we have shown analytically the equivalence of the DEFT-operator with an operator whose eigenvalues are given by momentum differences in the shift direction. In case of a transverse fiber shift, the DEFT-eigenstates with the highest or lowest eigenvalue feature a well-defined transverse momentum difference which causes them to behave in a beam-like fashion, as we could show. Moreover, they are by construction invariant to first order under a shift

of the entire fiber and also feature broad spectral correlation compared to random states which makes it possible to construct particlelike DEFT-pulses. We have also shown that the concept of DEFT can be applied to systems with scattering regions in which the concept of time-delay might also work. However, the latter does not yield particlelike states in systems without mode mixing and furthermore does not feature the invariance under a shift of the entire system which makes DEFT the best approach for finding particlelike states.

Next, we have examined the wave dynamics in the actual three-dimensional, D-shaped fiber in which we encountered certain difficulties due to the additional spatial dimension. In the generalization of the projection method for the time-delay operator, it is not possible to do subsequent rotations of the transmission matrix in subspaces of both of the two transverse positions or transverse momenta eigenstates. This is due to the non-commutativity of the corresponding operators, which is caused by the non-separability of the system. Being limited to only one rotation, we achieved the best results in terms of particlelike states by using the eigenstates of the angular momentum operator. Since the angular momentum is not a conserved quantity in these non-integrable D-shaped cross sections, we had to choose a smaller subset of angular momentum eigenstates compared the usage of the transverse momentum operator in our toy model in order to achieve reasonably good results. However, in fibers with a mixed phase space, those time-delay eigenstates are whispering gallery type states, which do conserve the angular momentum best, but do not occupy larger phase space islands.

Since it would be desirable to address all phase space islands in order to find more particlelike states, we moved on to applying the concept of the DEFT-operator to the three-dimensional fibers, where we have found to get the best results by shifting the fiber along its symmetry axis in the transverse plane. This fact originates from the shape of classical periodic orbits which rely on the system's symmetry. For this shifting direction, the eigenvectors of the DEFT-operator contains states that occupy classical phase space islands of regular dynamics. Even in completely chaotic geometries or arbitrary shifting directions we were able to find states which stay collimated in case of not too long propagation lengths. Together with the result for the two-dimensional toy model, we think that the concept of DEFT is generally a good approach for finding particlelike states in perfect systems as well as in imperfect systems with scattering regions.

Last, we have used Monte-Carlo methods to generate Gaussian-shaped trajectory bundles that feature spreading in order to mimic initial wavefronts. To achieve the best coincidence with our wave simulations in the fiber systems, we have used the standard deviation of the found DEFT-eigenstates along the shorter principal axis of the respective elliptically-shaped beam cross sections for the creation of our Gaussian-shaped bundles. In a fiber system, our simulations revealed that the fairly large amount of spreading makes it impossible for bundles to survive up to the propagation length used in our wave simulations. This shows that in

such small systems, interference is one of the key-ingredients for the survival of particlelike states. With respect to the experimental realization of this work at Yale University, we have also studied the dynamics of trajectory bundles in the D-shaped rod systems at hand, in order to make predictions about the underlying wave behavior. For a completely chaotic rod, we have found that we can categorize the found particlelike bundles into three types of orbits, namely diameter orbits, classically unstable periodic orbits and refocused orbits, whereas in a rod with a mixed phase space the particlelike bundles are mainly given by states that occupy phase space islands. Even if it is numerically not feasible to do wave simulations in rod-like systems, we have shown the good performance of the concept of DEFT in fiber-systems, which, together with the results of the trajectory bundle simulations in rods, makes us confident, that the experimental realization of DEFT will also yield nice results in such large geometries.

In a future work, one could address the question of the survival time of DEFT-eigenstates which occupy regular islands in a classically mixed phase space with respect to dynamic tunneling. Since we expect the tunneling rate to be small, the trapping on regular phase space islands limits the wavepacket size which would allow longer propagation times of our particlelike DEFT-states compared to systems with regular phase spaces in which the absence of islands causes a continuous linear spreading. Together with this island trapping, the concept of DEFT could be beneficial for multiplexing, where the additional use of the spatial degrees of freedom could lead to higher data rates compared to current techniques. Moreover, the particlelike DEFT-eigenstates feature a quantization transverse to the propagation direction like the particlelike eigenstates of the Wigner-Smith time-delay operator. Since the occurrence of this quantization is not yet fully understood, this could also be a possible topic of future research. Further interesting and not yet understood effects are the difference of correlation functions between DEFT-eigenstates and random states which is much more pronounced in a two-dimensional system and the shift of certain Husimi distributions w.r.t. the classical phase space which could be related to the Goos-Hänchen effect. Lastly, the treatment of realistic three-dimensional fiber systems including imperfections and bends would be an important task regarding future applications of these techniques.

Chapter 5

Acknowledgments

I would like to express my gratitude to my supervisor Philipp Ambichl for many useful discussions, comments, remarks and engagement through this master thesis. Furthermore, I would like to thank my supervising professor Stefan Rotter, who provided me guidance throughout this thesis, took his precious time for every question I had and gave me the possibility to visit the collaborating experimental physics group of Hui Cao at Yale University. Also, I would like to thank the group of Hui Cao for their collaboration and for making my stay in New Haven possible, where special thanks go to Stefan Bittner for giving me a warm welcome and providing me lots of useful tips regarding the everyday life in New Haven. Moreover, I would like to thank my fellow students without which the past years wouldn't have been the same. Last, I would like to deeply thank my parents for supporting me in every possible way in order to make my life as a student as easy as they can.

Appendix A

Hamiltonian Optics

Here we want to give a brief overview of Hamiltonian optics in order to see the striking similarity between the treatment of photon- and particle-trajectories which justifies our ray-treatment of light in the main text. Following [28], we start with Fermat's principle who states that light takes the path whose optical path length is an extremum, i.e.,

$$\delta \int_{P_1}^{P_2} n(x, y, z) d\zeta = 0 , \quad (\text{A.1})$$

where δ stands for a small variation of the path \mathcal{C} between two fixed endpoints $P_{1,2}$, $n(x, y, z)$ is the index of refraction of the medium the light is propagating in and $d\zeta = \sqrt{dx^2 + dy^2 + dz^2}$ is an infinitesimal element of the arc length. Next we choose an optical axis, e.g. z , and change variables such that $d\zeta \rightarrow dz$

$$\delta \int_{z_1}^{z_2} n \frac{d\zeta}{dz} dz = \delta \int_{z_1}^{z_2} n(x, y, z) \sqrt{1 + x'^2 + y'^2} dz = 0 \quad (\text{A.2})$$

in which $x' = dx/dz$ and $y' = dy/dz$. The integrand is then usually defined as the optical Lagrangian

$$L(x, y, x', y', z) = n(x, y, z) \sqrt{1 + x'^2 + y'^2} \quad (\text{A.3})$$

and the corresponding Euler-Lagrange equations are just given by

$$\frac{d}{dz} \left(\frac{dL}{dx'} \right) - \frac{dL}{dx} = 0 , \quad (\text{A.4})$$

$$\frac{d}{dz} \left(\frac{dL}{dy'} \right) - \frac{dL}{dy} = 0 . \quad (\text{A.5})$$

The Euler Lagrange-equations can now be rearranged into a single differential equation of second order

$$\frac{d}{ds} \left(n \frac{d\vec{x}}{d\zeta} \right) = \vec{\nabla} n , \quad (\text{A.6})$$

where $\vec{x} = (x, y, z)^T$ is a vector in coordinate space. Eq. (A.6) shows a striking similarity to the equations of motion for a classical point particle, i.e.,

$$\frac{d}{dt} \left(m \frac{d\vec{x}}{dt} \right) = F = -\vec{\nabla} V , \quad (\text{A.7})$$

where the time is replaced by the arclength and n can be interpreted as a potential whose gradient is the force acting on the photon changing its “momentum” $n d\vec{x}/d\zeta$.

To arrive at the Hamilton function we utilize the Legendre transform of the optical Lagrangian

$$H(x, y, p_x, p_y, z) = p_x x' + p_y y' - L(x, y, x', y', z) , \quad (\text{A.8})$$

where the so-called *ray momenta* are given by

$$p_x = \frac{\partial L}{\partial x'} = n(x, y, z) \frac{x'}{\sqrt{1 + x'^2 + y'^2}} = n \frac{dx}{ds} , \quad (\text{A.9})$$

$$p_y = \frac{\partial L}{\partial y'} = n(x, y, z) \frac{y'}{\sqrt{1 + x'^2 + y'^2}} = n \frac{dy}{ds} \quad (\text{A.10})$$

in accordance to the mechanical analogy mentioned above. The whole photon momentum can be written as

$$\vec{p} = n \frac{d\vec{x}}{d\zeta} = n \begin{pmatrix} \cos \alpha_1 \\ \cos \alpha_2 \\ \cos \alpha_3 \end{pmatrix} , \quad (\text{A.11})$$

where the vector consists of the so called *direction cosines* with respect to the x , y and z axis and $|\vec{p}| = n$. Inserting the optical Lagrangian and using the proper coordinates we arrive at the optical Hamiltonian

$$H(x, y, p_x, p_y, z) = -\sqrt{n^2(x, y, z) - p_x^2 - p_y^2} = -p_z , \quad (\text{A.12})$$

where the Hamilton equations of motion are then given by

$$\frac{dx}{dz} = \frac{\partial H}{\partial p_x} , \quad \frac{dp_x}{dz} = -\frac{\partial H}{\partial x} , \quad (\text{A.13})$$

$$\frac{dy}{dz} = \frac{\partial H}{\partial p_y} , \quad \frac{dp_y}{dz} = -\frac{\partial H}{\partial y} . \quad (\text{A.14})$$

It is worth noting that the choice of an optical axis is convenient but not necessary, since one can also parametrize a curve along an arbitrary parameter. Moreover, in Eq. (A.12) one can see another analogy to a relativistic point particle with mass m whose energy is given by

$$E = c\sqrt{m^2 c^2 + |\vec{p}|^2} , \quad (\text{A.15})$$

where the different sign in the square roots has its origin in the use of a Minkowski metric instead of an Euclidean metric in optics.

Appendix B

Exponential Growth of Distances in Chaotic Systems

Following [29], we show that in classically chaotic systems the distances between phase space trajectories grows exponentially, where the rate of growth is determined by the Lyapunov exponent Λ . Lets consider a state vector of a continuous system, \vec{x} , which is defined by a differential equation of the form

$$\dot{\vec{x}} = \vec{F}(\vec{x}(t)) , \quad (\text{B.1})$$

where \vec{F} is also called the tangent map. If the tangent map is a function which is continuously differentiable to first order, i.e. $\vec{F} \in C^1$, it is characterized by

$$\left| \vec{F}(\vec{x}(t)) - \vec{F}(\vec{x}'(t)) \right| \leq \Lambda |\vec{x}(t) - \vec{x}'(t)| . \quad (\text{B.2})$$

If the state vectors are part of a Euclidean space, Eq. (B.2) is just the definition of the Lipschitz continuity, where Λ is the Lipschitz constant. This criterion states that there has to be an upper bound for the growth of the distances between two solutions of the differential equation (B.1) which can be expressed as

$$\vec{x}(t) = \vec{x}(0) + \int_0^t dt \vec{F}(\vec{x}(t)) , \quad (\text{B.3})$$

$$\vec{x}'(t) = \vec{x}'(0) + \int_0^t dt' \vec{F}(\vec{x}'(t')) . \quad (\text{B.4})$$

The difference $d(t) \equiv |\vec{x}(t) - \vec{x}'(t)|$ between two state vectors can then be rewritten using the triangle inequality

$$d(t) = \left| \vec{x}(0) - \vec{x}'(0) + \int_0^t dt' \vec{F}(\vec{x}(t')) - \int_0^t dt' \vec{F}(\vec{x}'(t')) \right| \quad (\text{B.5})$$

$$\leq d(0) + \left| \int_0^t dt' \vec{F}(\vec{x}(t')) - \int_0^t dt' \vec{F}(\vec{x}'(t')) \right| . \quad (\text{B.6})$$

Inserting the Lipschitz continuity yields

$$d(t) \leq d(0) + \Lambda \int_0^t dt' d(t') \equiv D(t) . \quad (\text{B.7})$$

To solve this we can use the derivative of $D(t)$ w.r.t. t and get

$$\dot{D}(t) = \Lambda d(t) \leq \Lambda D(t) . \quad (\text{B.8})$$

This equation can now be easily integrated as

$$D(t) \leq D(0)e^{\Lambda t} = d(0)e^{\Lambda t} . \quad (\text{B.9})$$

Making use of the inequality (B.7) we arrive at

$$d(t) \leq d(0)e^{\Lambda t} , \quad (\text{B.10})$$

which proves that the distance between two trajectories can grow at most exponentially. This observation is the hallmark of classical chaos and makes the dynamical evolution of the system unpredictable, since infinitesimal deviations in the initial conditions grow exponentially fast. With this prove we can now define the Lyapunov exponent as

$$\Lambda_{\text{phys}}(\vec{x}_0) = \lim_{t \rightarrow \infty} \lim_{d(0) \rightarrow 0} \frac{1}{t} \ln \left(\frac{d(\vec{x}_0, t)}{d(\vec{x}_0, 0)} \right) . \quad (\text{B.11})$$

If a $\Lambda(\vec{x}_0) > 0$ exists we call it Lyapunov exponent, where it is worth noting that this exponent depends on the initial conditions \vec{x}_0 . Up to now we have just looked at continuous systems, but since we are using Birkhoff coordinates we use an analogous version for discrete maps, where the tangent map is replaced by the billiard map. Similarly we can define

$$\Lambda_{\text{Birk}}(\vec{x}_0) = \lim_{n \rightarrow \infty} \lim_{d(0) \rightarrow 0} \frac{1}{n} \ln \left(\frac{d(\vec{x}_0, n)}{d(\vec{x}_0, 0)} \right) , \quad (\text{B.12})$$

where we have replaced the time t by the number of bounces n . Since we are dealing with a billiard system our motion is bounded which makes the limit $d(0) \rightarrow 0$ in (B.11) and (B.12) necessary in order not to run into the regime, where distances between two trajectories are saturated due to the boundedness of the system.

Appendix C

Derivation of the Scalar Helmholtz Equation

In a medium without source terms, i.e. no charge density $\rho = 0$ and no current density $\vec{j} = 0$, a wave equation can be derived from the Maxwell equations,

$$\vec{\nabla} \cdot \vec{D}(\vec{r}, t) = 0 , \quad (\text{C.1})$$

$$\vec{\nabla} \cdot \vec{B}(\vec{r}, t) = 0 , \quad (\text{C.2})$$

$$\vec{\nabla} \times \vec{E}(\vec{r}, t) = -\frac{\partial \vec{B}(\vec{r}, t)}{\partial t} , \quad (\text{C.3})$$

$$\vec{\nabla} \times \vec{H}(\vec{r}, t) = \frac{\partial \vec{D}(\vec{r}, t)}{\partial t} , \quad (\text{C.4})$$

in which $\vec{D}(\vec{r}, t) = \epsilon(\vec{r})\vec{E}(\vec{r}, t)$ and $\vec{B}(\vec{r}, t) = \mu(\vec{r})\vec{H}(\vec{r}, t)$ with $\epsilon(\vec{r}) = \epsilon_0\epsilon_r(\vec{r})$ and $\mu(\vec{r}) = \mu_0\mu_r(\vec{r})$, where we assume $\mu_r(\vec{r}) \approx 1$. Taking the curl of Eq. (C.3) and inserting Eq. (C.4) yields

$$\vec{\nabla} \times (\vec{\nabla} \times \vec{E}) = \vec{\nabla} (\vec{\nabla} \cdot \vec{E}) - \vec{\nabla}^2 \vec{E} = -\mu_0\epsilon \frac{\partial^2 \vec{E}}{\partial t^2} . \quad (\text{C.5})$$

Because of Eq. (C.1) we can write

$$\vec{\nabla} \cdot (\epsilon \vec{E}) = \epsilon \vec{\nabla} \cdot \vec{E} + \vec{E} \cdot \vec{\nabla} \epsilon = 0 , \quad (\text{C.6})$$

and use the expression for the divergence of the electric field to arrive at the wave equation

$$\Delta \vec{E} - \mu_0\epsilon \frac{\partial^2 \vec{E}}{\partial t^2} + \vec{\nabla} \left(\frac{\vec{E} \cdot \vec{\nabla} \epsilon}{\epsilon} \right) = 0 . \quad (\text{C.7})$$

Since the dielectric function of our fiber system only changes in the transverse plane we can neglect longitudinal field components and set

$$\vec{\nabla} \left(\frac{\vec{E} \cdot \vec{\nabla} \epsilon}{\epsilon} \right) = 0 . \quad (\text{C.8})$$

Now we assume a monochromatic and linearly polarized electric field

$$\vec{E}(\vec{r}, t) = \hat{p}\psi(\vec{r})e^{-i\omega t} \quad (\text{C.9})$$

whose polarization direction is determined by the unit vector \hat{p} . Using $k_0^2 = \omega^2\epsilon_0\mu_0$ and $n^2(\vec{r}) = \epsilon_r(\vec{r})$, we arrive at the scalar Helmholtz equation:

$$[\Delta + n^2(\vec{r})k_0^2]\psi(\vec{r}) = 0 , \quad (\text{C.10})$$

where $k_0 = 2\pi/\lambda$ is the vacuum wave number.

Appendix D

Spatial Participation Ratio

Besides the standard deviation which is a measure of how broad the tails of a given distribution are there exists the concept of the so-called *inverse participation ratio* P . It is given by the expression

$$P = \frac{1}{\sum_n p_n^2} \quad \text{with} \quad p_n = |\langle \chi_n | \psi \rangle|^2, \quad (\text{D.1})$$

where p_n is the probability of finding the state $|\psi\rangle$ in one of the modes $|\chi_n\rangle$. If we consider for example only two modes and assume that $|\psi\rangle$ is an equally weighted superposition of both, then $P = 2$. From this, we can see that P is a measure for how many modes participate in a given state. We can easily generalize (D.1) to a spatial participation ratio by taking its inverse, projecting onto the transverse position eigenstates instead of the modes and replacing the sum by an integral over the cross section

$$P = \frac{\left[\int d^2r I(\vec{r}) \right]^2}{\int d^2r I^2(\vec{r})} \quad \text{with} \quad I(\vec{r}) = |\langle \vec{r} | \psi \rangle|^2 = |\psi(\vec{r})|^2, \quad (\text{D.2})$$

where $I(\vec{r})$ is the measured intensity. Note that we have added a term in the numerator which we only need if the state is not intensity normalized. To show that this quantity is a measure for the spatial extent of a state we consider two special cases:

- For a point-like intensity $I(\vec{r}) = \delta^{(2)}(\vec{r} - \vec{r}_0)$ the occupied area is zero:

$$P = \frac{\left[\int d^2r \delta^{(2)}(\vec{r} - \vec{r}_0) \right]^2}{\int d^2r [\delta^{(2)}(\vec{r} - \vec{r}_0)]^2} = \frac{1}{\delta^{(2)}(\vec{r}_0 - \vec{r}_0)} = 0. \quad (\text{D.3})$$

- For a constant intensity $I(\vec{r}) = c$ the occupied area is just the cross section:

$$P = \frac{\left[\int d^2r c \right]^2}{\int d^2r c^2} = \frac{c^2 A_{\text{fb}}^2}{c^2 A_{\text{fb}}} = A_{\text{fb}}. \quad (\text{D.4})$$

Bibliography

- [1] A. P. Mosk, A. Lagendijk, G. Lerosey, and M. Fink, “Controlling waves in space and time for imaging and focusing in complex media,” *Nature Photonics*, vol. 6, no. May, pp. 283–292, 2012.
- [2] S. M. Popoff, G. Lerosey, R. Carminati, M. Fink, a. C. Boccara, and S. Gigan, “Measuring the Transmission Matrix in Optics: An Approach to the Study and Control of Light Propagation in Disordered Media,” *Physical Review Letters*, vol. 104, no. March, pp. 1–4, 2010.
- [3] S. Bianchi and R. Di Leonardo, “A multi-mode fiber probe for holographic micromanipulation and microscopy,” *Lab on a Chip*, vol. 12, no. 3, p. 635, 2012.
- [4] T. Čižmár and K. Dholakia, “Shaping the light transmission through a multi-mode optical fibre: complex transformation analysis and applications in biophotonics,” *Optics express*, vol. 19, no. 20, pp. 18871–84, 2011.
- [5] M. Plöschner, T. Tyc, and T. Čižmár, “Seeing through chaos in multimode fibres,” *Nature Photonics*, vol. 9, no. 8, pp. 529–535, 2015.
- [6] S. Ree and L. E. Reichl, “Classical and quantum chaos in a circular billiard with a straight cut,” *Physical review. E, Statistical physics, plasmas, fluids, and related interdisciplinary topics*, vol. 60, no. 2, pp. 1607–1615, 1999.
- [7] V. Doya, O. Legrand, F. Mortessagne, and C. Miniatura, “Light Scarring in an Optical Fiber,” *Physical review letters*, vol. 88, p. 014102, 2002.
- [8] C. Michel, M. Allgaier, and V. Doya, “Regular modes of a mixed dynamical based optical fiber,” pp. 1–12, 2015, arXiv:1507.01355v1.
- [9] E. P. Wigner, “Lower Limit for the Energy Derivative of the Scattering Phase Shift,” *Physical Review*, vol. 98, pp. 5–7, 1955.
- [10] F. T. Smith, “Lifetime Matrix in Collision Theory,” *Physical Review*, vol. 118, no. 1, pp. 349–356, 1960.
- [11] S. Rotter, P. Ambichl, and F. Libisch, “Generating particlelike scattering states in wave transport,” *Physical Review Letters*, vol. 106, no. March, pp. 1–4, 2011.

- [12] B. Gérardin, J. Laurent, P. Ambichl, C. Prada, S. Rotter, and A. Aubry, “Particle-like wave packets in complex scattering systems,” pp. 1–30, 2016, arXiv:1602.05812v1.
- [13] B. Crespi, G. Perez, and S.-J. Chang, “Quantum Poincaré sections for two-dimensional billiards,” *Physical Review E*, vol. 47, no. 2, pp. 986–991, 1993.
- [14] M. C. Gutzwiller, *Chaos in Classical and Quantum Mechanics*. Springer, 2nd ed., 1991.
- [15] Z. Zheng and G. Hu, “Polygonal Approaches to the Circular Billiard: the Lyapunov Exponent,” *Commun. Theor. Phys.*, vol. 32, no. 2, pp. 221–228, 1999.
- [16] B. Friedman, Y. Oono, and I. Kubo, “Universal Behavior of Sinai Billiard Systems in the Small-Scatterer Limit,” *Physical Review Letters*, vol. 52, no. 9, pp. 709–712, 1984.
- [17] G. Benettin, L. Galgani, A. Giorgilli, and J.-M. Strelcyn, “Lyapunov Characteristic Exponents for smooth dynamical systems and for Hamiltonian systems; a method for computing all of them. Part 1: Theory,” *Meccanica*, vol. 15, no. 1, pp. 9–20, 1980.
- [18] R. Kaiser and D. F. Westbrook, *Coherent Atomic Matter Waves*. Springer, 1st ed., 2010.
- [19] A. Bäcker, S. Fürstberger, and R. Schubert, “Poincaré Husimi representation of eigenstates in quantum billiards,” *Physical Review E - Statistical, Nonlinear, and Soft Matter Physics*, vol. 70, pp. 1–10, 2004.
- [20] S. Datta, *Electronic Transport in Mesoscopic Systems*. Cambridge University Press, 1997.
- [21] E. N. Economou, *Green’s Functions in Quantum Physics*. Springer, 3rd ed., 2010.
- [22] A. A. Juarez, C. A. Bunge, S. Warm, and K. Petermann, “Perspectives of principal mode transmission in mode-division-multiplex operation,” *Optics Express*, vol. 20, no. 13, p. 13810, 2012.
- [23] S. Fan and J. M. Kahn, “Principal modes in multimode waveguides,” *Optics letters*, vol. 30, no. 2, pp. 135–137, 2005.
- [24] W. Xiong, P. Ambichl, Y. Bromberg, B. Redding, S. Rotter, and H. Cao, “Spatiotemporal Control of Light through a Multimode Fiber Using Principal Modes,” *submitted to PRL*, pp. 1–5, 2015, arXiv:1601.04646v1.

-
- [25] P. Ambichl, *Delay Times and Beyond in Coherent Wave Transport*. PhD thesis, Vienna University of Technology, 2016.
 - [26] K. Newrkla, “Semiclassical quantization of particlelike scattering states in a cavity,” 2016. Project Thesis (in preparation).
 - [27] Steffen Löck, *Dynamical tunneling in systems with a mixed phase space*. PhD thesis, Dresden University of Technology, 2010.
 - [28] A. Torre, *Linear Ray and Wave Optics in Phase Space*. Elsevier Science, 1st ed., 2005.
 - [29] J. Burgdörfer, “Classical and quantum chaos,” 2009. Lecture Notes.